



ISTITUTO NAZIONALE DI FISICA NUCLEARE
Laboratori Nazionali di Frascati

FRASCATI PHYSICS SERIES



Third Young Researchers Workshop
"Physics Challenges in the LHC Era"

2012

Editor:
Enrico Nardi

FRASCATI PHYSICS SERIES

Series Editor

Daniilo Babusci

Technical Editor

Debora Bifaretti

Cover by Claudio Federici

Volume LV

*Istituto Nazionale di Fisica Nucleare – Laboratori Nazionali di Frascati
Divisione Ricerca
SIDS – Servizio Informazione e Documentazione Scientifica
Ufficio Biblioteca e Pubblicazioni
P.O. Box 13, I-00044 Frascati Roma Italy
email: sis.publications@lnf.infn.it*

Copyright © 2012 by INFN

All rights reserved. No part of this publication may be reproduced, stored in a retrieval system or transmitted in any form or by any means, electronic, mechanical, photocopying, recording or otherwise, without the prior permission of the copyright owner.

ISBN 978–88–86409–59–9

**Third Young Researchers Workshop
“Physics Challenges in the LHC Era”
2012**

International Scientific Committee:

Guido Altarelli (*U. & INFN Roma3*)
Wilfried Buchmuller (*DESY*)
Filippo Ceradini (*U. & INFN Roma3*)
Anna Di Ciaccio (*U. & INFN Tor Vergata*)
John Ellis (*CERN*)
Benjamin Grinstein (*UC San Diego*)
Ida Peruzzi (*INFN-LNF & U. Perugia*)
Antonio Pich (*U. Valencia & IFIC, U. Valencia*)
Roberto Fiore (*U. Calabria & INFN Cosenza*)

Local Organizing Committee:

Mario Antonelli
Gennaro Corcella
Vittorio Del Duca
Chee Sheng Fong
Riccardo Faccini
Gino Isidori
Maria Paola Lombardo
Kotaroh Miura
Enrico Nardi (School Director)
Joel Jones-Perez
Tommaso Spadaro

CONTENTS

Preface		VI
Naser Ahmadiniaz	A Compact Representation of the Three-Gluon Vertex	1
Simone Biondini	Phenomenology of excited doubly charged leptons at LHC	7
Valerio Bortolotto	Search for the Higgs boson in the $H \rightarrow WW^{(*)} \rightarrow l\nu l\nu$ channel	13
Giordano Cattani	Forward-backward asymmetry measurement in $pp \rightarrow Z/\gamma^* \rightarrow \mu^+\mu^-$ events at $\sqrt{s} = 7$ TeV with the ATLAS experiment at the LHC	19
Pietro Dall’Olio	IR Behavior of the Propagators in Yang-Mills Theory	25
Audrey Degee	Minimal seesaw models and minimal lepton flavor violation	31
Andrea Gabrielli	Search for Hidden Higgs decays in the ATLAS detector	37
José García-Aguilar	The Superfield Formalism in a 5D Susy Model	43
Sergi González-Solís	$\eta - \eta'$ mixing angle from the semileptonic decays $D^+ \rightarrow \eta(\eta')e^+\nu_e$ and $B^+ \rightarrow \eta(\eta')l^+\nu$	49
Valerio Ippolito	Search for Higgs boson in the four lepton final state with the ATLAS experiment	55
Roberto Iuppa	Anisotropy in the Cosmic Radiation at TeV energy	61
Dmitriy Matvienko	Model of the decay $B^0 \rightarrow D^*\omega\pi$ and status of Belle analysis	67
Federico Meloni	ATLAS searches for supersymmetry at LHC	73
Beatrice Murdaca	The jet vertex for Mueller-Navelet and forward jet production	79
Beatrice Panico	Measurement of the Cosmic Rays primary spectrum with ARGO-YBJ experiment	85
Simona Salvini	Double Parton Interactions in Proton Deuteron Collision	91

PREFACE

The third Young Researcher Workshop "Physics Challenges in the LHC Era" was held in the Frascati Laboratories during May 7th and 10th 2012, in conjunction with the XVI edition of the Frascati Spring School "Bruno Touschek".

After three successful editions, the Frascati Young Researcher Workshop is now an established and important appointment for young physicists in the last stages of their graduate studies. Young researchers in theoretical and experimental particle physics are invited to present the results of their research work in a fifteen minutes talk, and discuss them with their colleagues. Students thus learn to condense the results of several months of work in a short presentation, and to organize a speech on a specialized subject in a way understandable to their other colleagues. They get a training in preparing the write up of their contribution for the Workshop Proceedings, they experience how to interact with the Scientific Editor and with the Editorial Office of the Frascati Physics Series and eventually, in many cases, their preprint ends up being their first individual submission to the arXive.org database. Helping to develop these skills is an integral part of the scientific formation the Frascati Spring School is providing.

These proceedings, that collect the joint efforts of the sixteen speakers of the Young Researchers Workshop 2012, give the best demonstration of the remarkable scientific level of the Workshop contributors. The sixteen short write-ups also set the benchmark for the scientific level required to apply for participating in the Workshop, and provide useful guidelines for structuring the presentations of our future young lecturers.

Many people contributed to the success of the XVI Frascati Spring School "Bruno Touschek" and of the joint 3rd Young Researcher Workshop "Physics Challenges in the LHC Era". A special acknowledgment goes to Maddalena Legramante, that carried out with her usual efficiency the secretariat work both for the Workshop and for the Spring School, to Claudio Federici, that put special efforts in realizing the graphics of the Workshop, of the School posters, and of the front page of the proceedings, and to Debora Bifaretti, for the technical editing. I also want to thank the director of the LNF Research Division Vitaliano Chiarella, the responsabile of the SIDS Danilo Babusci, and the responsabile of the LNF seminars Manuela Boscolo, for sponsoring the XVI Spring School and for their precious help. Finally, a special thanks goes to the Director of the Frascati Laboratories Prof. Umberto Dosselli for his encouragement and unconditional support.

Frascati, July 2012

Enrico Nardi

Frascati Physics Series
3rd YOUNG RESEARCHERS WORKSHOP: “Physics Challenges in the LHC Era”
Frascati, May 7 and 10, 2012

A COMPACT REPRESENTATION OF THE THREE-GLUON VERTEX

N. Ahmadinia, C. Schubert

*Dipartimento di Fisica, Università di Bologna and INFN,
Sezione di Bologna Via Irnerio 46, I-40126 Bologna, Italy*

*Instituto de Física y Matemáticas
Universidad Michoacana de San Nicolás de Hidalgo
Apdo. Postal 2-82
C.P. 58040, Morelia, Michoacán, México*

Abstract

The three-gluon vertex is a basic object of interest in nonabelian gauge theory. It contains important structural information, in particular on infrared divergences, and also figures prominently in the Schwinger-Dyson equations. At the one-loop level, it has been calculated and analyzed by a number of authors. Here we use the worldline formalism to unify the calculations of the scalar, spinor and gluon loop contributions to the one-loop vertex, leading to an extremely compact representation. The SUSY - related sum rule found by Binger and Brodsky follows from an off-shell extension of the Bern-Kosower replacement rules. We explain the relation of the structure of our representation to the low-energy effective action.

1 Introduction

The off-shell three-gluon vertex has been under investigation for more than three decades. By an analysis of the nonabelian gauge Ward identities, Ball and Chiu ¹⁾ in 1980 found a form factor decomposition of this vertex which is valid at any order in perturbation theory, with the only restriction that a covariant gauge be used. At the one-loop level, they also calculated the vertex explicitly for the case of a gluon loop in Feynman gauge. Later Cornwall and Papavassiliou ²⁾ applied the pinch technique to the non-perturbative study of this vertex. Davydychev, Osland and Sax ³⁾ calculated the massive quark contribution of the one loop three-gluon vertex. Binger and Brodsky ⁴⁾ calculated the one-loop vertex in the pinch technique and found the following SUSY-related identity between its scalar, spinor and gluon loop contributions,

$$3\Gamma_{\text{scalar}} + 2\Gamma_{\text{spinor}} + \Gamma_{\text{gluon}} = 0 \quad (1)$$

In this talk, I present a recalculation of the scalar, spinor and gluon loop contributions to the three-gluon vertex using the worldline formalism ^{5, 6, 7, 8)}. The vertex is shown in fig. 1 (for the fermion loop case).

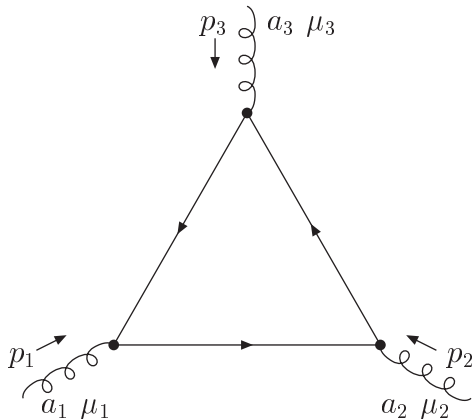


Figure 1: Three-gluon vertex.

Following the notation of ³⁾, we write

$$\Gamma_{\mu_1\mu_2\mu_3}^{a_1a_2a_3}(p_1, p_2, p_3) = -igf^{a_1a_2a_3}\Gamma_{\mu_1\mu_2\mu_3}(p_1, p_2, p_3) \quad (2)$$

The gluon momenta are ingoing, such that $p_1 + p_2 + p_3 = 0$. There are actually two diagrams differing by the two inequivalent orderings of the three gluons

along the loop. Those diagrams add to produce a factor of two.
The Ball-Chiu decomposition of the vertex can be written as

$$\begin{aligned}
\Gamma_{\mu_1\mu_2\mu_3}(p_1, p_2, p_3) = & A(p_1^2, p_2^2; p_3^2)g_{\mu_1\mu_2}(p_1 - p_2)_{\mu_3} + B(p_1^2, p_2^2; p_3^2)g_{\mu_1\mu_2}(p_1 + p_2)_{\mu_3} \\
& + C(p_1^2, p_2^2; p_3^2) \left[p_{1\mu_2}p_{2\mu_1} - (p_1 \cdot p_2)g_{\mu_1\mu_2} \right] (p_1 - p_2)_{\mu_3} \\
& + \frac{1}{3}S(p_1^2, p_2^2, p_3^2) \left[p_{1\mu_3}p_{2\mu_1}p_{3\mu_2} + p_{1\mu_2}p_{2\mu_3}p_{3\mu_1} \right] \\
& + F(p_1^2, p_2^2; p_3^2) \left[(p_1 \cdot p_2)g_{\mu_1\mu_2} - p_{1\mu_2}p_{2\mu_1} \right] \left[p_{1\mu_3}(p_2 \cdot p_3) - p_{2\mu_3}(p_1 \cdot p_3) \right] \\
& + H(p_1^2, p_2^2, p_3^2) \left\{ -g_{\mu_1\mu_2} \left[p_{1\mu_3}(p_2 \cdot p_3) - p_{2\mu_3}(p_1 \cdot p_3) \right] \right. \\
& \quad \left. + \frac{1}{3} \left[p_{1\mu_3}p_{2\mu_1}p_{3\mu_2} - p_{1\mu_2}p_{2\mu_3}p_{3\mu_1} \right] \right\} \\
& + \left\{ \text{cyclic permutations of } (p_1, \mu_1), (p_2, \mu_2), (p_3, \mu_3) \right\}
\end{aligned} \tag{3}$$

Here the A , C and F functions are symmetric in the first two arguments, B antisymmetric, and $H(S)$ are totally (anti)symmetric with respect to interchange of any pair of arguments. Note that the F and H functions are totally transverse, i.e., they vanish when contracted with any of $p_{1\mu_1}$, $p_{2\mu_2}$ or $p_{3\mu_3}$.

2 The scalar loop case

In the worldline formalism the three-gluon amplitude for the scalar loop case is represented as ^{6, 8)}

$$\begin{aligned}
\Gamma_{\text{scalar}}^{a_1 a_2 a_3}[p_1, \varepsilon_1; p_2, \varepsilon_2; p_3, \varepsilon_3] = & (-ig)^3 \text{tr}(T^{a_1} T^{a_2} T^{a_3}) \int_0^\infty \frac{dT}{T} e^{-m^2 T} \\
\times \int \mathcal{D}x(\tau) \int_0^T d\tau_1 \varepsilon_1 \cdot \dot{x}_1 e^{ip_1 \cdot x_1} \int_0^{\tau_1} d\tau_2 \varepsilon_2 \cdot \dot{x}_2 e^{ip_2 \cdot x_2} \varepsilon_3 \cdot \dot{x}_3 e^{ip_3 \cdot x_3} e^{-\int_0^T \frac{\dot{x}^2}{4}}
\end{aligned} \tag{4}$$

Here T is the total proper time of the loop particle, m the mass of the loop particle, T^a a generator of the gauge group in the representation of the scalar, and $\int \mathcal{D}(x)$ an integral over closed trajectories in Minkowski space-time with periodicity T . Although our calculation will be off-shell, we introduce gluon polarization vectors ε_i as a book-keeping device. Each gluon is represented by a vertex operator $\int d\tau \varepsilon \cdot \dot{x} e^{ip \cdot x}$. Translation invariance in proper-time has been used to set $\tau_3 = 0$.

The path integral (4) is Gaussian so that its evaluation requires only the standard combinatorics of Wick contractions and the appropriate Green's function,

$$\langle x^{\mu_1}(\tau_1)x^{\mu_2}(\tau_2) \rangle = -G_{B12}g^{\mu_1\mu_2}, \quad G_{B12} := G_B(\tau_1, \tau_2) = |\tau_1 - \tau_2| - \frac{(\tau_1 - \tau_2)^2}{T} \quad (5)$$

In this formalism structural simplification can be expected from the removal of all second derivatives \ddot{G}_{Bij} 's, appearing after the Wick contractions, by suitable integrations by part (IBP). After doing this we have (see 8) for the combinatorial details of the Wick contraction and IBP procedure)

$$\begin{aligned} \Gamma_{\text{scalar}} &= \frac{g^3}{(4\pi)^{D/2}} (\Gamma_{\text{scalar}}^3 + \Gamma_{\text{scalar}}^2 + \Gamma_{\text{scalar}}^{\text{bt}}) \\ \Gamma_{\text{scalar}}^3 &= -\text{tr}(T^{a_1}[T^{a_2}, T^{a_3}]) \int_0^\infty \frac{dT}{T^{\frac{D}{2}}} e^{-m^2 T} \int_0^T d\tau_1 \int_0^{\tau_1} d\tau_2 Q_3^3|_{\tau_3=0} e^{(G_{B12}p_1 \cdot p_2 + G_{B13}p_1 \cdot p_3 + G_{B23}p_2 \cdot p_3)} \\ \Gamma_{\text{scalar}}^2 &= \Gamma_{\text{scalar}}^3(Q_3^3 \rightarrow Q_3^2) \\ \Gamma_{\text{scalar}}^{\text{bt}} &= -\text{tr}(T^{a_1}[T^{a_2}, T^{a_3}]) \int_0^\infty \frac{dT}{T^{\frac{D}{2}}} e^{-m^2 T} \int_0^T d\tau_1 \dot{G}_{B12} \dot{G}_{B21} \left[\varepsilon_3 \cdot f_1 \cdot \varepsilon_2 e^{G_{B12}p_1 \cdot (p_2 + p_3)} + 2 \text{perm} \right] \\ Q_3^3 &= \dot{G}_{B12} \dot{G}_{B23} \dot{G}_{B31} \text{tr}(f_1 f_2 f_3) \\ Q_3^2 &= \frac{1}{2} \dot{G}_{B12} \dot{G}_{B21} \text{tr}(f_1 f_2) \sum_{k=1,2} \dot{G}_{B3k} \varepsilon_3 \cdot p_k + 2 \text{perm} \end{aligned} \quad (6)$$

The abelian field strength tensors $f_i^{\mu\nu} := p_i^\mu \varepsilon_i^\nu - \varepsilon_i^\mu p_i^\nu$ appear automatically in the IBP procedure. The $\Gamma_{\text{scalar}}^{\text{bt}}$'s are boundary terms of the IBP.

We rescale to the unit circle, $\tau_i = T u_i, i = 1, 2, 3$, and rewrite these integrals in term of the standard *Feynman/Schwinger* parameters, related to the u_i by

$$u_1 = \alpha_2 + \alpha_3, \quad u_2 = \alpha_3, \quad u_3 = 0, \quad \alpha_1 + \alpha_2 + \alpha_3 = 1 \quad (7)$$

For the scalar case, we find

$$\begin{aligned} \Gamma_{\text{scalar}} &= \frac{g^3}{(4\pi)^{\frac{D}{2}}} \text{tr}(T^{a_1}[T^{a_2}, T^{a_3}]) (\gamma_{\text{scalar}}^3 + \gamma_{\text{scalar}}^2 + \gamma_{\text{scalar}}^{\text{bt}}) \\ \gamma_{\text{scalar}}^3 &= \Gamma\left(3 - \frac{D}{2}\right) \text{tr}(f_1 f_2 f_3) I_{3,B}^D(p_1^2, p_2^2, p_3^2) \\ \gamma_{\text{scalar}}^2 &= \frac{1}{2} \Gamma\left(3 - \frac{D}{2}\right) \left[\text{tr}(f_1 f_2) \left(\varepsilon_3 \cdot p_1 I_{2,B}^D(p_1^2, p_2^2, p_3^2) - \varepsilon_3 \cdot p_2 I_{2,B}^D(p_2^2, p_1^2, p_3^2) \right) + 2 \text{perm} \right] \\ \gamma_{\text{scalar}}^{\text{bt}} &= -\Gamma\left(2 - \frac{D}{2}\right) \left[\varepsilon_3 \cdot f_1 \cdot \varepsilon_2 I_{\text{bt},B}^D(p_1^2) + 2 \text{perm} \right] \end{aligned} \quad (8)$$

where

$$\begin{aligned}
I_{3,B}^D(p_1^2, p_2^2, p_3^2) &= \int_0^1 d\alpha_1 d\alpha_2 d\alpha_3 \delta(1 - \alpha_1 - \alpha_2 - \alpha_3) \\
&\quad \times \frac{(1 - 2\alpha_1)(1 - 2\alpha_2)(1 - 2\alpha_3)}{\left(m^2 + \alpha_1\alpha_2 p_1^2 + \alpha_2\alpha_3 p_2^2 + \alpha_1\alpha_3 p_3^2\right)^{3-\frac{D}{2}}} \\
I_{2,B}^D(p_1^2, p_2^2, p_3^2) &= \int_0^1 d\alpha_1 d\alpha_2 d\alpha_3 \delta(1 - \alpha_1 - \alpha_2 - \alpha_3) \\
&\quad \times \frac{(1 - 2\alpha_2)^2(1 - 2\alpha_1)}{\left(m^2 + \alpha_1\alpha_2 p_1^2 + \alpha_2\alpha_3 p_2^2 + \alpha_1\alpha_3 p_3^2\right)^{3-\frac{D}{2}}} \\
I_{bt,B}^D(p^2) &= \int_0^1 d\alpha \frac{(1 - 2\alpha)^2}{\left(m^2 + \alpha(1 - \alpha)p^2\right)^{2-\frac{D}{2}}}
\end{aligned} \tag{9}$$

3 Fermion and gluon loop calculations

By an off-shell generalization of the Bern-Koswer replacement rules ⁵⁾, whose correctness for the case at hand we have verified, one can get the results for the spinor and gluon loop from the scalar loop one simply by replacing

$$\begin{aligned}
\Gamma_{\text{scalar}} \rightarrow \Gamma_{\text{spinor}} : \quad & I_{\{3,2,\text{bt}\},B}^D \rightarrow I_{\{3,2,\text{bt}\},B}^D - I_{\{3,2,\text{bt}\},F}^D \\
\Gamma_{\text{scalar}} \rightarrow \Gamma_{\text{gluon}} : \quad & I_{\{3,2,\text{bt}\},B}^D \rightarrow I_{\{3,2,\text{bt}\},B}^D - 4I_{\{3,2,\text{bt}\},F}^D
\end{aligned} \tag{10}$$

where the $I_{(\cdot)F}^D$'s are three integrals similar to the $I_{(\cdot)B}^D$'s above (for the spinor loop one must also multiply by a global factor of -2).

From (10) we immediately recover the Binger-Brodsky identity eq.(1).

4 Comparison with the effective action

Finally let us compare our results with the low energy expansion of the QCD effective action induced by a scalar loop,

$$\Gamma_{\text{scalar}}[F] = \int_0^\infty \frac{dT}{T} \frac{e^{-m^2 T}}{(4\pi T)^{\frac{D}{2}}} \text{tr} \int dx_0 \sum_{n=2}^\infty \frac{(-T)^n}{n!} \text{O}_n[F] \tag{11}$$

For our comparison we need only O_2 and O_3 which are ⁸⁾

$$O_2 = -\frac{1}{6}F_{\kappa\lambda}F^{\kappa\lambda} \quad , \quad O_3 = -\frac{2}{15}iF_{\kappa}^{\lambda}F_{\lambda}^{\mu}F_{\mu}^{\kappa} - \frac{1}{20}D_{\kappa}F_{\lambda\mu}D^{\kappa}F^{\lambda\mu} \quad (12)$$

where

$$F_{\mu\nu} = f_{\mu\nu} + ig[A_{\mu}, A_{\nu}] \quad , \quad f_{\mu\nu} = \partial_{\mu}A_{\nu} - \partial_{\nu}A_{\mu} \quad , \quad D_{\mu} = \partial_{\mu} + igA_{\mu} \quad (13)$$

We can recognize the correspondences

$$\begin{aligned} \gamma_{(\cdot)}^3 &\leftrightarrow F_{\kappa}^{\lambda}F_{\lambda}^{\mu}F_{\mu}^{\kappa} = f_{\kappa}^{\lambda}f_{\lambda}^{\mu}f_{\mu}^{\kappa} + \text{higher point terms} \\ \gamma_{(\cdot)}^2 &\leftrightarrow (\partial + igA)\underbrace{F(\partial + igA)}F \\ \gamma_{(\cdot)}^{\text{bt}} &\leftrightarrow (f + ig\underbrace{[A, A]})\underbrace{(f + ig[A, A])} \end{aligned} \quad (14)$$

5 Conclusions and outlook

In our recalculation of the scalar, spinor and gluon contributions to the one-loop three gluon vertex we have achieved a significant improvement over previous calculations both in efficiency and compactness of the result. This improvement is in large part due to the replacement rules (10) whose validity off-shell we have verified. Details and a comparison with the Ball-Chiu decomposition will be presented elsewhere. We believe that along the lines presented here even a first calculation of the four-gluon vertex would be feasible.

References

1. J. S. Ball and T. W. Chiu, Phys. Rev. D **22**, 2550 (1980).
2. J. M Cornwall and J. Papavassiliou, Phys. Rev. D **40**, 3474 (1989).
3. A. I. Davydychev, P. Osland and L. Saks, JHEP 0108:050 (2001).
4. M. Binger and S. J. Brodsky, Phys. Rev. D **74**, 054016 (2006).
5. Z. Bern and D. A. Kosower, Phys. Rev. Lett. **66**, 1669 (1991); Nucl. Phys. B **379**, 451 (1992).
6. M. J. Strassler, Nucl. Phys. B **385**, 145 (1992).
7. M. Reuter, M. G. Schmidt and C. Schubert, Ann. Phys. (N.Y.) **259**, 313 (1997).
8. C. Schubert, Phys. Rept. **355**, 73 (2001).

Phenomenology of excited doubly charged heavy leptons at the LHC

Biondini Simone
*Technische Universität Muenchen,
International Max Planck Research School*

Abstract

We consider the production at the LHC of exotic composite leptons of charge $Q = +2e$. Such states are allowed in composite models which contain extended isospin multiplets ($I_W = 1$ and $I_W = 3/2$). These doubly charged leptons couple with Standard Model fermions via gauge interactions, thereby delineating and restricting their possible decay channels. We discuss the production cross section at the LHC of L^{++} ($pp \rightarrow L^{++}, \ell^-$) and concentrate on the leptonic signature deriving from the cascade decays $L^{++} \rightarrow W^+ \ell^+ \rightarrow \ell^+ \ell^+ \nu_\ell$ i.e. $pp \rightarrow \ell^- (\ell^+ \ell^+) \nu_\ell$ showing that the invariant mass distribution of the like-sign dilepton has a sharp end point corresponding to excited lepton mass m^* . We find that the $s = \sqrt{7}$ TeV run is sensible at the 3-sigma (5-sigma) level to a mass of the order of 600 GeV if $L = 10 \text{ fb}^{-1}$ ($L = 20 \text{ fb}^{-1}$). The $s = \sqrt{7}$ TeV run can reach a sensitivity at 3-sigma (5-sigma) level up to $m^* = 1 \text{ TeV}$ for $L = 20 \text{ fb}^{-1}$ ($L = 60 \text{ fb}^{-1}$).

1 Introduction

It is the ambitious goal of particle physics to understand how Nature works involving only the smallest number of fundamental elements. However, during the last century, the number of fundamental particles grew, and at present we have a scheme with three generations of quarks and leptons, twelve in all. Furthermore, we have to add fundamental gauge bosons. It seems that we have three patterns of quarks and leptons organized in growing masses but sharing all remaining features (charge, weak isospin, color). Can we explain this proliferation of fermionic states? A natural explanation for the replication of fermionic generations could be that they are not truly fundamental particles but instead bound states of some unknown constituents. The idea of further level of compositeness has been investigated phenomenologically for quite some time ^{1), 2)}. In this work, we emphasize a particular aspect of compositeness: the weak isospin invariance. In this view, proposed in ³⁾, the usual singlet ($I_W = 0$) and doublet ($I_W = \frac{1}{2}$) isospin values are extended to include $I_W = 0$ and $I_W = \frac{3}{2}$. Hence, multiplets (triplets and quartets) appear that contain exotic doubly charged leptons of charge $Q = +2e$ and exotic excited quark states of charge $Q = +(5/3)e$. These exotic states are expected to generate interesting signatures to be searched for at the LHC since this accelerator can provide sufficient energy to produce such new hypothetical massive particles.

2 Model

In the early days of hadronic physics, much progress was made by using strong isospin to discuss the possible patterns of baryon and meson resonances even when quarks and gluons were still unknown. In the same spirit, as a great number of strong resonant low energy $\mathcal{O}(1)$ GeV states which were found, we may expect something similar in the electroweak interaction, of course at much higher energies. Here, the Higgs vacuum expectation value parameter $v \simeq 238$ GeV ought to play the role of the energy scale for possible fermionic resonances, thereby an expectation of some new physics at $\mathcal{O}(1)$ TeV scale seems natural. With this point of view, weak isospin spectroscopy could reveal some properties of excited fermions without reference to a direct internal dynamics of the building blocks. We begin then with all SM fermions as belonging to isospin doublets or singlets, as usual, i.e. $I_W = 0$ and $I_W = \frac{1}{2}$, and the electroweak

bosons having $I_W = 0$ and $I_W = 1$. Thus, only fermionic excited states with $I_W \leq \frac{3}{2}$ can arise provided one only uses the light SM fermions and EW gauge bosons. In order to compute the production cross section and decays of these excited fermions, we need to define their couplings to light fermions and gauge bosons. The rules are easily derived referring to weak Isospin and Y (hypercharge). Since, all the gauge fields have $Y = 0$, excited fermions can only couple to light fermions with the same Y value. Moreover, to satisfy gauge invariance, we need a transition current containing a $\sigma_{\mu\nu}$ term and not a single γ_μ , i.e. an anomalous magnetic moment type coupling. (This consideration automatically provides current conservation). The effective Lagrangian density for $I_W = 1$ is (L stands for excited leptons spinor) :

$$\mathcal{L} = \frac{gf_1}{m^*} \left(\bar{L} \sigma_{\mu\nu} \partial^\nu W^\mu \frac{1 + \gamma^5}{2} \ell \right) + h.c. \quad (1)$$

while for $I_W = \frac{3}{2}$ reads:

$$\mathcal{L} = C_{(\frac{3}{2}, M|1, m; \frac{1}{2}, m')} \frac{gf_3}{m^*} \left(\bar{L}_M \sigma_{\mu\nu} \partial^\nu W^\mu \frac{1 - \gamma^5}{2} \ell_{m'} \right) + h.c. \quad (2)$$

In the above equations, m^* is the excited fermion mass, and f_1, f_3 are dimensionless coupling constants, expected to be of order one, whose precise value can only be fixed through a specific compositeness model.

In order to perform the needed numerical calculations of the production cross sections and kinematical distributions, we need to implement our model in CalcHEP. We implemented the above lagrangians through FeynRules ⁵⁾, a Mathematica ⁴⁾ package that generates the Feynman rules of any given quantum field theory model as specified by a particular lagrangian.

3 Doubly charged leptons phenomenology

Considering the interaction lagrangians discussed above and the fact that the doubly charged L^{--} and L^{++} can interact with the light fermion only via the W^\pm gauge boson one can easily compute the partial and total decay width of these exotic states. Indeed the only available decay channel of the doubly charged lepton is $L^{++} \rightarrow W^+ \ell^+$ with $\mathcal{B}(L^{++} \rightarrow W^+ \ell^+) = 1$. The analytic

expression of the total decay width is easily derived:

$$\Gamma_{L^{++}} = \Gamma(L^{++} \rightarrow W^+ \ell^+) = \left(\frac{f}{\sin \theta_W} \right)^2 \alpha_{QED} \frac{m^*}{8} \left(2 + \frac{M_W^2}{m^{*2}} \right) \left(1 - \frac{M_W^2}{m^{*2}} \right)^2 \quad (3)$$

According to the expected large mass for the excited states we can use the approximation $M_W \ll m^*$ and Eq. 3 suggests that decay width increases linearly with the mass i.e. $\Gamma = \kappa m^*$ as shown in Fig.1. Following the convention and

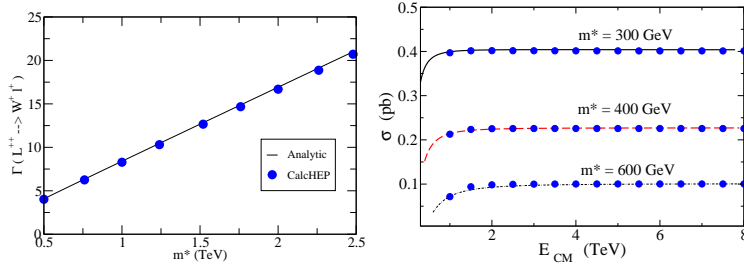


Figure 1: a) The decay width of the exotic lepton L^{++} , as a function of its mass m^* . We compare the analytical result with the CalcHEP output (blue dots) b) we show the total parton cross section for L^{++} or L^{--} against energy in center of mass frame. We give parton cross section for three different values of excited lepton mass. The analytical result is compared with CalcHEP output (blue dots).

notation of 3) we write down the parton cross section for both $I_W = 1$ and $I_W = \frac{3}{2}$. We give the expressions for L^{++} using Maldestam variables:

$$\left(\frac{d\hat{\sigma}}{d\hat{t}} \right)_{u\bar{d} \rightarrow L^{++}\ell^-} = \frac{1}{4m^{*2}s^2} \frac{G_1^2}{4\pi} \frac{s}{(s - M_W^2)^2 + (M_W \Gamma_W)^2} \left\{ \left(\frac{g^2}{4} \right) [m^{*2}(s - m^{*2}) + 2ut] \pm 2 \left(-\frac{g^2}{8} \right) m^{*2}(t - u) \right\} \quad (4)$$

where $G_1^2 = g^2 f^2/3$ or $G_1^2 = g^2 f'^2/3$. There is a difference which should be stressed. The plus $+sign$ in Eq. 5 must be used for $I_W = 1$ while the same $-sign$ must be used for $I_W = 3/2$. We obtain the expression for the total parton cross section integrating all over the angular variables.

In order to obtain the production cross section we need CalcHEP numerical session. We have used the CTEQ6m parton distribution functions and the

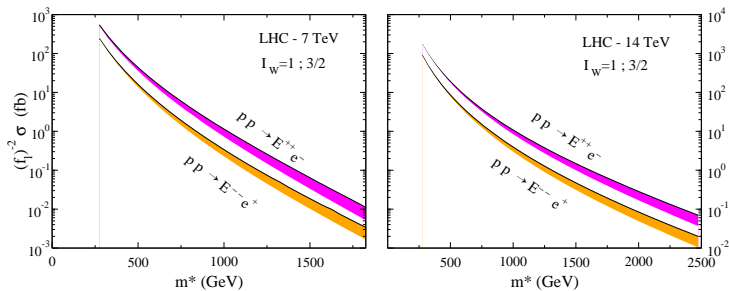


Figure 2: The uncertainty bands (magenta and orange) correspond to running the factorization and renormalization scale from $Q = M_W$ (solid line) up to $Q = m_*$. All contributing sub-processes within the first two generations have been summed up. The results are the same for both isospin values $I_W = 1$ and $I_W = \frac{3}{2}$, due to the structure of parton cross section.

results are shown in the Fig.2. It is easier to produce positively doubly charged leptons at the LCH due to the parton proton content.

4 Invariant mass distribution

We are considering particles coming from two decays, leading to the final state particle set: in this case, as suggested in ⁶⁾ one should observe a like sign dilepton mass invariant distribution with a sharp end point at m_* , which is also close to the maximum of the distribution. This is what we clearly get for the signal. Considering all the irreducible Standard Model background we provide a comparison between the invariant mass in the two cases.

Finally we give a more realistic description of the final state event at LHC. The distributions of the main kinematic variables given in previous section are related to numerical CalcHEP outputs and they do not refer to reconstructed objects. They are ideal particles. The Pretty Good Simulator ⁷⁾ software reconstructs all particles in the final state event, introducing the efficiency of each detector such as trackers resolution, calorimeter geometrical acceptance and resolution. The result for reconstructed invariant mass distribution for signal and background is shown in Fig.3.

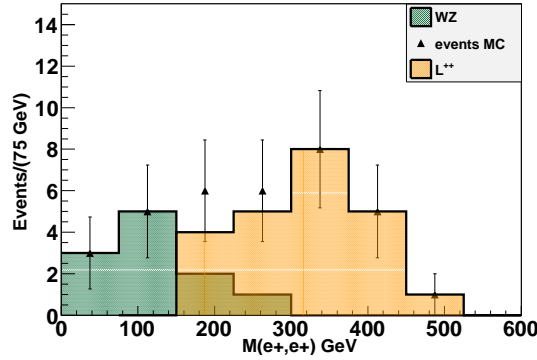


Figure 3: The invariant mass distribution of the SSDL after the fast detector simulation for the run at $\sqrt{s} = 7$ TeV. A value of $m^* = 500$ GeV is assumed for the mass of the doubly charged lepton. The signal is the orange filled line while the background is the green filled line. The panel refers to integrated luminosity of $L = 10 \text{ fb}^{-1}$.

References

1. E. Eichten, K. D. and M. E. Peskin, Phys. Rev. Lett. **50**, 811 (1983).
2. N. Cabibbo, L. Maiani and Y. N. Srivastava, Phys. Lett. **B 149**, 459 (1984).
3. G. Pancheri and Y. N. Srivastava, Phys. Lett. B **146**, 87 (1984).
4. Mathematica Edition (Wolfram Research, Inc., Champaign, IL, 2008), Version 7.0.
5. A. Pukhov E. Boos, M. Dubinin, V. Edneral, V. Ilyin, D. Kovalenko, A. Kryukov, V. Savrin, S. Shichanin, and A. Semenov, arXiv:hep-ph/9908288v2.
6. A. J. Barr and C. G. Lester, J. Phys. G **146** 123001 (2010)
7. <http://physics.ucdavis.edu/conway/research/software/pgs/pgs4-general.htm>.

Frascati Physics Series
3rd YOUNG RESEARCHERS WORKSHOP: “Physics Challenges in the LHC Era”
Frascati, May 7 and 10, 2012

SEARCH FOR THE HIGGS BOSON IN THE $H \rightarrow WW^{(*)} \rightarrow l\nu l\nu$ CHANNEL

Valerio Bortolotto
Università degli studi Roma Tre

Abstract

I will report the recent results for the Standard Model Higgs Boson searches using 4.7 fb^{-1} of proton-proton collisions data at $\sqrt{s} = 7 \text{ TeV}$, recorded with the ATLAS detector at the Large Hadron Collider in 2011. The analysis considers the decay channels $H \rightarrow WW \rightarrow l\nu l\nu$ where $l = (e \text{ or } \mu)$ with final states containing charged leptons and missing transverse energy.

1 Introduction

All particles predicted by the Standard Model (SM) have been observed but one, the Higgs boson. This is a fundamental part of the SM because it's connected to the Higgs Mechanism ¹⁾ which in the SM gives mass to all other massive elementary particles. For this reason one of the main goal of the experiments at the Large Hadron Collider (LHC) is the search of this particle.

ATLAS reported the results for a search of the decay $H \rightarrow WW \rightarrow l\nu l\nu$ with l electron or muon, for 4.7 fb^{-1} of pp collision at $\sqrt{s} = 7 \text{ TeV}$ of data acquired during the 2011 ²⁾. In this analysis a SM Higgs boson in the mass range from 133 GeV to 261 GeV is excluded at 95% CL. In this proceeding a description of this analysis is reported. Section 2 describes the event selection while at the Section 3 the result of the analysis is presented.

2 Event Selection

For the total leptonic decay $H \rightarrow WW$ a preselection is made requiring exactly two oppositely charged leptons with high p_T . At least one selected lepton must match a triggering object. To suppress leptons coming from heavy-flavour decays and jet the leptons are required to be isolated: the scalar sum of the p_T of charged particles and of the calorimeter energy deposits within $\Delta R = \sqrt{\Delta\phi^2 + \Delta\eta^2} = 0.3$ of the lepton direction is required to be less than 0.15 the lepton p_T . To reject the two opposite-sign high p_T leptons coming from the Drell-Yan production of Z/γ^* or Υ resonances backgrounds in the same flavour channel (ee and $\mu\mu$) a dilepton invariant mass greater than 12 GeV is required. In those channels the dilepton invariant mass must also differ from the Z-boson mass M_Z by at least 15 GeV. For the $e\mu$ channel (different flavour channel), the dilepton invariant mass is required to be larger than 10 GeV. The remaining multijet and Drell-Yan events are suppressed by requiring large E_T^{miss} . The E_T^{miss} is the magnitude of p_T^{miss} , the opposite of the vector sum of the reconstructed object's trasverse momenta, including muons, electrons, photons jets and calorimeter clusters not associated with these objects. $E_{T,\text{rel}}^{\text{miss}}$ is defined as $E_{T,\text{rel}}^{\text{miss}} = E_T^{\text{miss}} \sin\Delta\phi_{\text{min}}$ with $\phi_{\text{min}} \equiv \min(\Delta\phi, \frac{\pi}{2})$. Here $\Delta\phi$ is the angle between $E_{T,\text{rel}}^{\text{miss}}$ and transverse momentum of the nearest lepton or jet which passed the selection criteria explained above. The Drell-Yan and the multijet production via QCD processes background events are suppressed by requiring $E_{T,\text{rel}}^{\text{miss}} > 45 \text{ GeV}$ for the same flavor leptons and $E_{T,\text{rel}}^{\text{miss}} > 25 \text{ GeV}$ for the $e\mu$ where the Drell-Yan background originates predominantly from the $\tau\tau$ production channel.

To maximise the sensitivity further selections, depending on the jet multiplicity, are introduced. All events are subdivided into H+0, H+1 and H+2-jet channels according to the jet counting obtained using the antikt algorithm ³⁾ with distance parameter $R = 0.4$. In figure 1 the jet multiplicity for all events

satisfying the preselection criteria described previously are shown. Only jets with $p_T > 25\text{GeV}$ and $|\eta| < 4.5$ are counted. As shown in figure 1 the background composition depends significantly on jet multiplicity, as does the signal topology. Without accompanying jets the signal is dominated by the ggF process, while in the presence of two or more jets the signal receives the main contribution from VBF process. Due to the spin-0 nature of the Higgs boson a spin correlation in the $WW^{(*)}$ system is present. The two charged leptons tend to emerge from the interaction point in the same direction. This kinematic feature is exploited in all jet multiplicities by requiring the azimuthal opening angle between the two leptons $\Delta\phi_{ll}$ to be less than 1.8 radians and the dilepton invariant mass m_{ll} to be less than 50 GeV for the H+0jet and H+1jet channels and 80 GeV for the H+2jets.

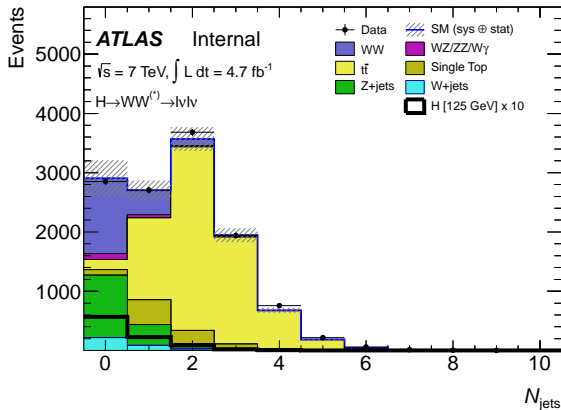


Figure 1: *Multiplicity of jets within the acceptance described in the text, after the cut on $E_{T,rel}^{miss}$. The shaded region indicates the total uncertainty on the background prediction. The superimposed signal shown is for $m_H = 125\text{ GeV}$.*

For large Higgs boson masses the leptons tend to have higher p_T and a larger angular separation therefore the opening angle cut $\Delta\phi_{ll}$ is used only for the low m_H defined as $m_H < 200\text{ GeV}$. For an intermediate m_H ($200\text{ GeV} \leq m_H \leq 300\text{ GeV}$) only a $m_{ll} < 150\text{ GeV}$ criteria is retained, with the exclusion of the mass region $|m_{ll} - M_Z| < 15\text{ GeV}$ in the ee and $\mu\mu$ final states.

For high m_H ($300 < m_H < 600$ GeV) the $m_{ll} < 150$ GeV is also omitted. After those selections to improve the rejection of Drell-Yan background in the H+0-jet channel a requirement on trasverse momentum of the dilepton system P_{Tll} is also done. The P_{Tll} is required to be larger than 30 GeV for the $e\mu$ channel and larger than 45 GeV for the ee and $\mu\mu$ channels.

In the H+1jet channel the main background originates from the top quark decay. This background is suppressed rejecting any event containing a b-tagged jet ⁴⁾ and using the total momentum P_{Ttot} . The P_{Ttot} , defined as the magnitude of the vector sum $P_{Ttot} = p_{Tll} + p_{T1j} + p_{Tmiss}$, is required to be smaller than 30 GeV to suppress background events with jets with p_T below threshold. To reject events with two τ the dilepton invariant mass must differ from the Z-boson mass M_Z by at least 25 GeV. The H+2jet selection is based on the same selection criteria of the H+1jet channel (with the P_{Ttot} definition modified to include the second jet) and on other jet-related cuts: the two highest- p_T jets ("tag" jets) in the event are required to lie in opposite rapidity hemispheres ($\eta_{j1} \times \eta_{j2} < 0$) and must be separated in pseudorapidity by a distance $|\Delta\eta_{jj}|$ of at least 3.8 units. In addition the invariant mass of the "tag" jets, m_{jj} , must be at least 500 GeV and there must be no other jet within $|\eta| < 3.2$. In all the jet multiplicity channels a trasverse mass variable, m_T ⁵⁾, is used to test for the presence of a signal. This variable is defined as:

$$m_T = \sqrt{(E_T^{ll} + E_T^{miss})^2 - |p_T^{ll} + p_T^{miss}|^2} \quad (1)$$

3 Results

In table 1 the expected number of events from signal with a higgs mass hypothesis of $m_H = 125$ GeV and background and data after all the selection

Table 1: *The expected numbers of signal and background events after the trasverse mass selection ($0.75m_H < m_T < m_H$). In the rightmost column the observed numbers of events in data are also shown.*

$m_H = 125\text{GeV}$	Signal	Total Bkg.	Obs.
0-jet	26 ± 7	172 ± 21	174
1-jet	6 ± 2	42 ± 6	56
2-jet	0.5 ± 0.1	0.4 ± 0.3	0

criteria for all lepton flavours combined are shown. The statistical analysis of the data is made using a likelihood function $\mathcal{L}(\mu, \theta)$ constructed as the product of Poisson probability terms in each lepton flavour channel. The test statistic q_μ is then constructed using a profile likelihood: $q_\mu = -2 \ln \left(\mathcal{L}(\mu, \hat{\theta}_\mu) / \mathcal{L}(\hat{\mu}, \hat{\theta}) \right)$. This test statistic is used to compute the exclusion limits following the CL_s ⁶⁾ method. Figure 2 shows the observed and expected cross section upper limit at 95% CL for all the jet multiplicity analyses as a function of m_H . No significant excess of events over the expected background has been observed and a Standard Model Higgs boson with a mass in the range from 133 GeV to 261 GeV is excluded at 95% CL while the expected exclusion range is from 127 GeV to 233 GeV.

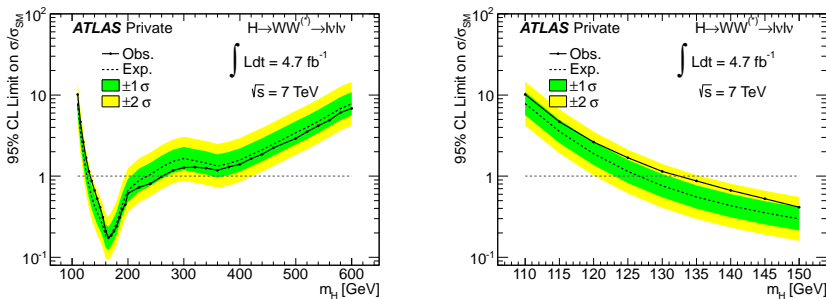


Figure 2: *Expected (dashed) and observed (solid) 95% C.L. upper limits on the cross section, normalised to the SM cross section, as a function of m_H . The green and yellow regions indicate the $\pm 1\sigma$ and $\pm 2\sigma$ uncertainty bands on the expected limit, respectively. The results at neighbouring mass points are highly correlated due to the limited mass resolution in this final state.*

4 Conclusion

A search for the SM Higgs boson using the $H \rightarrow WW \rightarrow l\nu l\nu$, based on the pp collision with $\sqrt{s} = 7$ TeV recorded in the 2011 with the ATLAS detector, has been presented. No significant excess of events over the expected background has been observed and a Standard Model Higgs boson with a mass in the range

from 133 GeV to 261 GeV is excluded at 95% CL while the expected exclusion range is from 127 GeV to 233 GeV.

References

1. P.W. Higgs, Broken Symmetries and the Masses of Gauge Bosons, *Phys. Rev. Lett.* **13**, 321 (1964).
2. ATLAS Collaboration, Search for the Standard Model Higgs boson in the $H \rightarrow WW^{(*)} \rightarrow l\nu l\nu$ decay mode with $4.7fb^{-1}$ of ATLAS data at $\sqrt{s} = 7$ TeV, submitted to *Phys.Lett.B*, arXiv:1206.0756.
3. M. Cacciari, G.P. Salam, and G.Soyez, Anti- K_t jet clustering algorithm, *JHEP* **0804** 063 (2008), arXiv:0802.1189.
4. ATLAS Collaboration, Commissioning of the ATLAS high-performance b-tagging algorithms in the 7 TeV collision data, ATLAS-CONF-2011-102 (2011).
5. A.J. Barr, B. Gripaios, and C.G. Lester, Measuring the Higgs boson mass in dileptonic W-boson decays at hadron colliders, *JHEP* **0907** 072 (2009), arXiv:0902.4864 [hep-ph].
6. G.Cowan, K. Cranmer, E. Gross, and O. Vitellis, Asymptotic formulae for likelihood-based test of new physics, *Eur.Phys.J.* **C71** 1554 (2011).

Frascati Physics Series
3rd YOUNG RESEARCHERS WORKSHOP: “Physics Challenges in the LHC Era”
Frascati, May 7 and 10, 2012

**FORWARD-BACKWARD ASYMMETRY MEASUREMENT IN
 $pp \rightarrow Z/\gamma^* \rightarrow \mu^+\mu^-$ EVENTS AT $\sqrt{s} = 7$ TeV WITH THE ATLAS
EXPERIMENT AT THE LHC**

Giordano Cattani
INFN, Sezione di Roma “Tor Vergata”
Dipartimento di Fisica, Università degli Studi di Roma “Tor Vergata”

Abstract

The forward-backward asymmetry, A_{fb} , is one of the first precision measurements that can be performed at the Large Hadron Collider (LHC). It will improve the knowledge of Standard Model parameters giving a direct insight on the vector (g_V^f) and axial-vector (g_A^f) couplings to the Z/γ^* , and thus to the effective weak mixing angle and at the same time it tests the existence of possible New Physics scenarios.

In this paper I will present a preliminary measurement of the ongoing studies on the mass dependence of the forward-backward asymmetry in $pp \rightarrow Z/\gamma^* \rightarrow \mu^+\mu^-$ interactions with collision data corresponding to approximately 4.7 fb^{-1} of integrated luminosity, collected by the ATLAS experiment at the LHC at $\sqrt{s} = 7$ TeV during 2011 data taking.

1 Introduction

Muon pairs can be produced through the Drell-Yan process over a large invariant mass range at CERN Large Hadron Collider (LHC) ¹). In the Standard Model (SM) of particle physics, the process occurs to first order via $q\bar{q}$ annihilation into a real (or virtual) Z boson or a virtual photon (γ^*). The presence of both vector and axial-vector couplings of the fermions to the Z boson gives rise to a forward-backward asymmetry (A_{fb}) in the distribution of the polar angle θ of the negatively charged muon relative to the incoming quark direction in the rest frame of the muon pair.

This asymmetry is particularly useful in searching for new interactions at large momentum transfers ($Q^2 = m_{\mu\mu}^2$) where $m_{\mu\mu}^2$ is the invariant mass of the muon pair. Moreover, the asymmetry shape would be modified by new resonances (e.g. additional heavier Z' bosons). The measurement of A_{fb} can also improve QCD measurements with higher order corrections, constraint Parton Distribution Functions (PDFs) and be used to extract basic SM parameters as the effective weak mixing angle.

2 The forward-backward asymmetry

At the LHC the Drell-Yan process is $q\bar{q} \rightarrow Z/\gamma^* \rightarrow \mu^+\mu^-$. The differential cross section for muon pairs production can be written as:

$$\frac{d\sigma(q\bar{q} \rightarrow \mu^+\mu^-)}{d\cos\theta} = A(1 + \cos^2\theta) + B\cos\theta \quad (1)$$

where A and B are functions dependent of the weak isospin and charge of the incoming quarks and Q^2 of the interaction.

The $\cos\theta$ term integrates to zero in the total cross section but induces the forward-backward asymmetry. Events with $\cos\theta > 0$ are called forward events, while events with $\cos\theta < 0$ are called backward events. The integrated cross section for forward events is thus $\sigma_F = \int_0^1 \frac{d\sigma}{d\cos\theta} d\cos\theta$ and the integrated cross section for backward events is $\sigma_B = \int_{-1}^0 \frac{d\sigma}{d\cos\theta} d\cos\theta$. The A_{fb} is defined as

$$A_{fb} = \frac{\sigma_F - \sigma_B}{\sigma_F + \sigma_B} = \frac{N_F - N_B}{N_F + N_B} = \frac{3B}{8A} \quad (2)$$

where N_F and N_B are the number of forward and backward events.

The Collins-Soper formalism ²⁾ is adopted to minimize the effect of the transverse momentum of the incoming quarks. In this formalism, the polar axis is defined as the one bisecting the angle between the momentum of one of the partons and the opposite of the momentum of the second one when they are boosted into the center-of-mass frame of the muon pair. The cosine of the decay angle, $\cos\theta^*$, can be written as a function of the muon momenta in the laboratory reference frame. Let $Q(Q_T)$ be the four momentum (transverse momentum) of the muon pair, P_1 and P_2 be the four-momentum of the muon and anti-muon respectively, all measured in the lab frame. Then $\cos\theta^*$ is given by

$$\cos\theta^* = \frac{2}{Q\sqrt{Q^2 + Q_T^2}}(P_1^+ P_2^- - P_1^- P_2^+) \quad (3)$$

where $P_i^\pm = \frac{1}{\sqrt{2}}(P_i^0 \pm P_i^3)$, with P^0 and P^3 representing the energy and the longitudinal component of the momentum.

3 Data sets and event selection

This analysis is based on an integrated luminosity of approximately 4.7 fb^{-1} , obtained with stable LHC beams and on-line muon triggers, together with high-quality data from the ATLAS detector. A detailed description of the ATLAS detector can be found elsewhere ³⁾.

Collision events are selected by requiring the timing information of the event to be in coincidence with a paired LHC proton bunch and a trigger from the muon system with a momentum threshold of $p_T = 18 \text{ GeV}$. Furthermore event selection requires at least three inner detector tracks associated with a reconstructed primary vertex. The subset of data used in this paper is then obtained by requiring two muons with $p_T > 20 \text{ GeV}$ and $|\eta| < 2.4$, the muons are identified by the match of an inner-detector track with a track reconstructed in the muon spectrometer and the muon parameters are derived from the inner-detector measurement. Both muons are required to be isolated from other tracks and in particular from jets. The p_T of all the tracks are summed in a cone of radius $\Delta R = 0.2$ around the muon candidate and a cut on the quantity $I_\mu = \frac{\sum_{tracks} p_T}{p_T^\mu} < 0.1$ is applied. The invariant mass of the di-muon system is required to be in the window $60 \text{ GeV} < m_{\mu\mu} < 1000 \text{ GeV}$.

Simulated ATLAS Monte Carlo samples are used to model the properties of signal and backgrounds, as well as to correct for several experimental

effects. The main signal event sample for Z/γ^* production is generated using the PYTHIA ⁴⁾ event generator and other generators are used to produce background samples. Passage of particles through the ATLAS detector is modeled using GEANT4. The effect of multiple interactions per bunch crossing (“pileup”) is modeled by overlaying simulated minimum bias events over the original hard-scattering event.

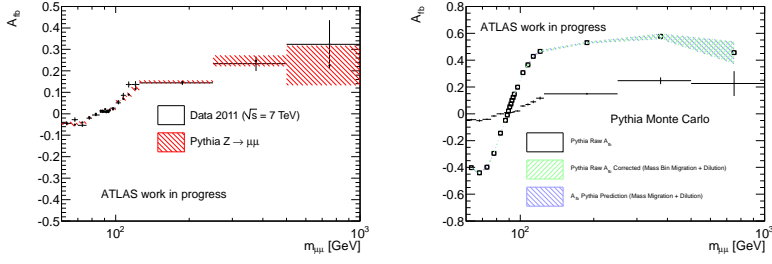
Differences between data and simulation need to be accounted for applying proper trigger/reconstruction scale factors (SFs) and muon momentum scale and resolution corrections to the Monte Carlo simulation.

4 A_{fb} measurement and corrections

A_{fb} depends on the center-of-mass energy s and it is thus measured as a function of the di-muon invariant mass, $m_{\mu\mu}$, dividing the invariant-mass range from 60 to 1000 GeV into 21 bins of different width.

Another important aspect of this measurement concerns the corrections that have to be applied to the measured A_{fb} distribution. This quantity is indeed measured as a *reconstructed* quantity, meaning that its value is measured with a finite detector resolution and, in principle, could not correspond to its *true* physical value. Moreover, other effects influence the shape of the reconstructed A_{fb} distribution. The emission of photons in the final state (Final State Radiation, FSR) can change the reconstructed p_T of the muons, resulting in a bad reconstruction of the Z/γ^* invariant mass and asymmetry. Finally, the lack of knowledge of the incoming quark direction can lead to a bad identification of a forward(backward) event as a backward(forward) one, resulting in a *dilution* of the asymmetry. The combined contributions of these effects modify the *true* A_{fb} spectrum resulting in the measured, *raw*, A_{fb} distribution (Fig. 1(a)), that has to be corrected to get back to the physical, *true*, distribution. Fig. 1(b) shows the closure test on Monte Carlo. The final result is in finalization within the ATLAS collaboration. Therefore, in summary, three main effects are taken into account: radiative corrections and detector resolution, accounted for with the mass bin migration correction, and dilution. The A_{fb} measurement is corrected for these effects by means of a Monte Carlo response-matrix based unfolding (Fig. 2). The RooUnfold toolkit ⁵⁾ is used to perform the unfolding based on the iterative Bayesian method ⁶⁾.

Propagation of the statistical error on the *raw* spectrum through the un-



(a) *Raw* A_{fb} as a function of di-muon invariant mass. Points with errors refer to data, red boxes refer to the *true* PYTHIA A_{fb} distribution to MC signal. (b) Closure test. The *unfolded* PYTHIA A_{fb} has been compared with the predicted A_{fb} distribution to make sure that the result of the unfolding agrees with the predicted A_{fb} distribution.

Figure 1: *Raw* A_{fb} distribution 1(a) and Monte Carlo closure test 1(b).

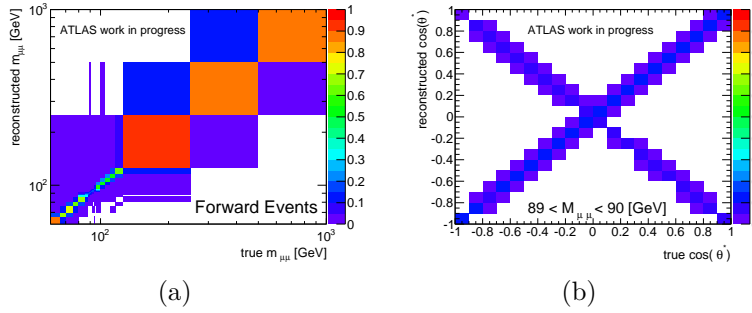


Figure 2: Response matrices to account for mass bin migration effect 2(a) and for dilution effect in a given mass bin 2(b).

folding procedure is not straightforward, due to the iterative nature of the method. For this analysis, an approach based on pseudo-experiments was chosen. The input to the unfolding algorithm (i.e. the *raw* A_{fb}) is randomly fluctuated around its mean value, thus producing pseudo-experiments. Each of the pseudo-experiments is then used to produce an *unfolded* A_{fb} spectrum. As

expected, the pseudo-experiments peak around the reference value. A Gaussian fit to these distributions yields a standard deviation per mass bin, which is used as statistical error on the *unfolded* A_{fb} value.

The systematic uncertainty on the asymmetry spectrum receives contributions from different sources:

- one specific algorithm was chosen for the unfolding. A different algorithm would have given a different *unfolded* distribution;
- the unfolding is completely MC-based and some specific MC samples were used. Different MC samples (e.g. with different generator or PDFs) could in principle lead to a different *unfolded* spectrum;
- once the MC samples are chosen, they only provide a limited number of events, i.e. the statistical error on the response matrices used for unfolding propagates (as a systematic) to the error on the *unfolded* spectrum.

5 Conclusions

The preliminary measurement at the ATLAS experiment of the Z/γ^* forward-backward asymmetry in $pp \rightarrow Z/\gamma^* \rightarrow \mu^+\mu^-$ events has been described and the main systematic uncertainties have been studied. Further analyses are in progress to extract a precision measurement of the effective weak mixing angle.

References

1. E. Lyndon and B. Philip (ed.), *LHC Machine*, JINST **3** (2008) S08001.
2. J. C. Collins and D. E. Soper, Phys. Rev. **D16**, 2219-2225 (1977).
3. ATLAS Collaboration, *The Atlas Experiment at the CERN Large Hadron Collider*, JINST **3** (2008) S08003.
4. T. Sjostrand, S. Mrenna and P. Z. Skands. *PYTHIA 6.4 Physics and Manual*, arXiv:hep-ph/0603175v2.
5. T. Adye, *Unfolding algorithms and tests using RooUnfold*, arXiv:1105.1160v1.
6. G. D'Agostini, Nucl. Instrum. Meth. A **362** (1995) 487-498.

Frascati Physics Series
3rd YOUNG RESEARCHERS WORKSHOP: “Physics Challenges in the LHC Era”
Frascati, May 7 and 10, 2012

IR BEHAVIOR OF THE PROPAGATORS IN YANG-MILLS THEORY

Pietro Dall’Olio

Instituto de Física y Matemática, UMSNH, 58040 Morelia, Michoacán, Mexico.

Abstract

It is widely known that in QCD the infrared region is not available to perturbative calculations due to the presence of a Landau pole in the running of the coupling constant. We present non perturbative solutions for the propagators in Yang-Mills theory by numerically solving a truncated system of Dyson-Schwinger equations and compare them with analytical results found by applying Callan-Symanzik renormalization group equations in an epsilon expansion near the infrared fixed point, when a mass term for the gluon is added to the action.

1 Gribov-Zwanziger scenario

The investigation of Yang-Mills theory, i.e. the pure gauge sector of QCD, has been pushed forward in the last decades, with the aim of exploring the physical

consequences of the gauge self-interaction, due to the non Abelianity of the symmetry $SU(N)$ involved.

In a continuum definition of the theory different analytical and semi-analytical approaches have been developed to extract non-perturbative information about correlation functions, whose infrared (IR) behavior can be related to the explanation of phenomena such as confinement and dynamical chiral symmetry breaking.

The first who made an important step ahead in this sense was Gribov ¹⁾, who realized that in a non Abelian theory, the Faddeev-Popov prescription for fixing the gauge (a mandatory step in a continuum formulation of a gauge theory) in a covariant manner, is incomplete, i.e. there are still gauge configurations on the same orbit that satisfy the gauge condition. In particular, in Landau gauge, the condition $\partial_\mu A_\mu^a(x) = 0$ is satisfied by two configurations connected by an infinitesimal gauge transformation $\theta(x)$ if the Faddeev-Popov operator satisfies $-\partial_\mu D_\mu \theta(x) = 0$. Therefore Gribov conjectured that, in order to get rid of the undesired gauge copies, one should confine the functional integration on those gauge configurations that make the Faddeev-Popov operator positive definite, the first Gribov region.

It is important to stress that such a restriction forbids the generation of a Landau pole for the renormalized coupling constant for values of momentum different from zero (no-pole condition ¹⁾).

Later Zwanziger ^{2, 3)} managed to implement this restriction, to all orders of perturbation theory, directly into the action through a non-local extra term. In this new action, known as Gribov-Zwanziger (GZ) action, BRST symmetry ⁵⁾ is softly broken (the breaking term has dimension 2) and the gluon propagator at tree level takes the form

$$\langle A_\mu(p)^a A_\nu(-q)^b \rangle = \frac{p^2}{p^4 + 2g^2 N \gamma^4} \left(\delta_{\mu\nu} - \frac{p_\mu p_\nu}{p^2} \right) \delta^{ab} (2\pi)^D \delta^D(p - q), \quad (1)$$

where γ is a mass parameter fixed by the horizon condition ²⁾. In the deep infrared the ghost propagator, at one loop, behaves like

$$\langle c^a(p) \bar{c}^b(-q) \rangle \propto \frac{1}{p^4} \delta^{ab} (2\pi)^D \delta^D(p - q). \quad (2)$$

Therefore, for low values of momenta, the GZ action predicts a vanishing gluon

propagator and an infrared enhanced ghost propagator (this behavior is known as *ghost dominance*).

2 Dyson-Schwinger equations

Calculating higher order corrections to the propagators from the GZ action is rather cumbersome, therefore it is more practical to use other techniques to investigate the IR behavior of the propagators. Dyson-Schwinger equations (DSEs) ^{6, 7}, in particular, proved to be a powerful tool for non perturbative calculations. These constitute an infinite collection of equations for the n-point Green's function, each one involving proper vertices of higher order, so that the tower of equations needs to be truncated in order to get a closed system numerically solvable.

It is noteworthy, as clarified by Zwanziger ⁴), that the restriction to the Gribov region does not change the structure of DSEs, since these are derived by taking a total derivative inside the generating functional of connected diagrams, and the boundary term generated by this restriction is zero, since the determinant of the Faddeev-Popov operator vanishes on the boundary of the Gribov region by definition. Therefore, the DSEs are derived by the usual Euclidean Faddeev-Popov action in Landau gauge

$$S = \int d^D x \left[\frac{1}{4} F_{\mu\nu}^a(x) F_{\mu\nu}^a(x) + \partial_\mu \bar{c}^a(x) D_\mu^{ab} c^b(x) + i \partial_\mu A_\mu^a(x) B^a(x) \right], \quad (3)$$

$$F_{\mu\nu}^a(x) = \partial_\mu A_\nu^a(x) - \partial_\nu A_\mu^a(x) + g f^{abc} A_\mu^b(x) A_\nu^c(x), \quad D_\mu^{ab} = \delta^{ab} \partial_\mu + g f^{acb} A_\mu^c(x).$$

Nevertheless, the effect of the Gribov horizon is taken into account in the truncation scheme and in the boundary conditions for the correlation functions. In particular, in solving the DSEs for the ghost and the gluon propagators we have considered only the diagrams with internal ghost propagators, since we are interested in the IR behavior and as it has been stressed, at low momenta the ghost propagator dominates over the gluon one, due to the presence of the Gribov horizon. Moreover, the dressed ghost-gluon vertex has been approximated with the bare one, relying on the Taylor's argument ⁸) on the non-renormalization of the ghost-gluon vertex in Landau gauge. The truncated DSEs are depicted in fig.1.

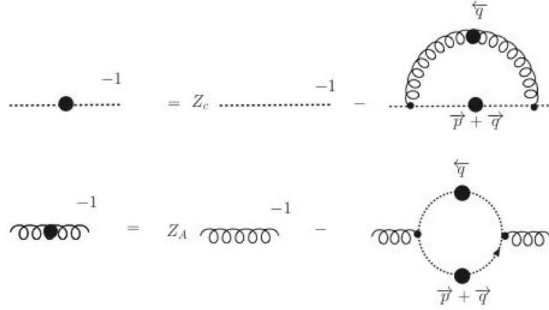


Figure 1: *The truncated DSEs. The large black circles stand for the full propagators, the small ones for the bare ghost-gluon vertices.*

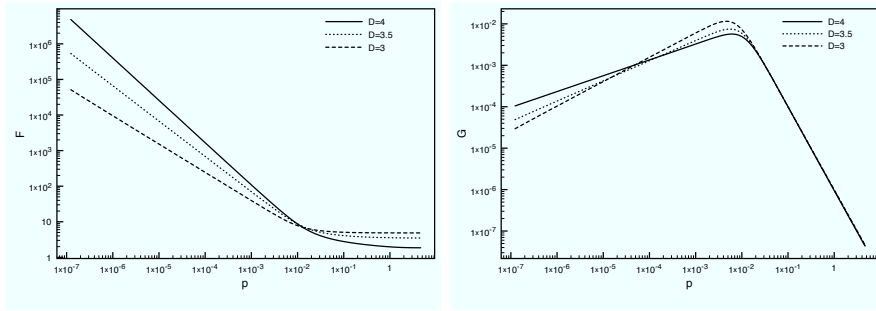


Figure 2: *The ghost dressing function $F(p)$ and the gluon propagator $G(p)$ for Euclidean dimensions $D=3, 3.5, 4$. The momenta and the gluon propagator are scaled in units of the UV cut-off.*

We have solved the system of equations numerically by an iteration process, with a regularization function insertion that smoothly suppress the ultraviolet (UV) modes, as described in ⁹).

If the ghost renormalization constant Z_c is fixed by imposing the *horizon condition*, i.e., the singularity of the ghost dressing function $F(p)$ at vanishing momenta (as suggested by the first order GZ action), while Z_A is fixed by im-

Table 1: IR exponents and running coupling constant at zero momentum for the scaling solutions.

dimension	α	β	$\alpha_R(0)$
3	0.60	0.80	0.76
3.5	0.48	0.99	1.52
4	0.38	1.19	2.97

posing that the gluon propagator $G(p)$ coincides with its tree-level counterpart in UV (asymptotic freedom), then a power-like behavior is found for the propagators in IR, with a vanishing gluon propagator, $G(p) \sim p^\alpha$, and an enhanced ghost dressing function $F(p) \sim p^{-\beta}$. These are known as the *scaling* solutions (they are depicted in fig.2 for different values of Euclidean dimension).

Due to the non-renormalization of the gluon-ghost vertex is also possible to define a dimensionless running coupling constant $\alpha_R(p) = p^{D-2}G(p)F^2(p)$, which approaches to a constant value in IR, corresponding to an IR fixed point (see Table 1).

Implementing a different renormalization scheme, where the Z_c is fixed, similarly to Z_A , by requiring that the renormalized ghost propagator approaches its classical value in the UV, we have obtained a different type of solution, where both $G(p)$ and $F(p)$ approach constant values for vanishing momenta. These are known as the *decoupling* solutions. In particular, solving the system for different values of the Euclidean dimension, we found in the IR that the gluon propagator fits very well the power law $G(p) = A + Bp^{D-2}$, and the renormalized coupling constant vanishes at zero momentum.

Furthermore, both scaling and decoupling solutions for the gluon have been found to violate reflection positivity ¹⁰⁾, corroborating the confined nature of the gluon.

3 Renormalization Group

The numerical solutions of the DSEs are in good agreement with the analytical expressions for the propagators found by applying the renormalization group machinery to the Faddeev-Popov action when a mass term for the gluon is included ¹¹⁾, as naturally generated by the breaking of the BRST symmetry in Landau gauge due to the restriction to the Gribov region. The presence of a

mass term for the gluon changes the scaling behavior of the gluon field, under the renormalization group transformation, and generates a high-temperature IR fixed point of upper critical dimension $D = 2$, where all the couplings with the exception of the ghost-gluon vertex becomes irrelevant, i.e. the ghost dominance is recovered.

Calculating the anomalous dimensions at one loop for the ghost and gluon propagator and integrating the Callan-Symanzik equations near the IR stable fixed point, one recovers the same behavior that we found for the decoupling solutions from the DSEs. Moreover, implementing the horizon condition by a fine tuning through which a *Lifshitz point* is realized in the IR ghost sector, corresponding to a non trivial stable fixed point whose upper critical dimension is $D = 6$, one recovers the scaling solutions and the IR exponents are found to be¹ $\alpha = (6 - D)/5$ and $\beta = (2D - 2)/5$, in good agreement with the ones numerically found.

References

1. V.N. Gribov, Nucl. Phys. B **139**, (1978).
2. D. Zwanziger, Nucl. Phys. B **323**, 513-544, (1989).
3. D. Zwanziger, Nucl. Phys. B **399**, 477-513, (1993).
4. D. Zwanziger, Phys. Rev. D **65**, 094039, (2002).
5. C. Becchi, A. Rouet and R. Stora, Phys. Lett. B **52**, 344, (1974).
6. F.J. Dyson, Phys. Rev. **75**, 1736, (1949).
7. J.S. Schwinger, Proc. Nat. Acad. Sci. **37**, 452, (1951).
8. J.C. Taylor, Nucl. Phys. B **33**, 436-444, (1971).
9. M. Leder *et al* Phys. Rev. D **83**, 025010, (2011).
10. K. Osterwalder and R. Schrader, Commun. Math. Phys. **31**, 83-112, (1973)
11. A. Weber *Preprint* arXiv:1112.1157 [hep-th], (2011).

¹In [11] a different convention for the IR exponents is used.

Minimal seesaw models and minimal lepton flavor violation

Audrey Degée
*IFPA, Dep. AGO, Université de Liège,
Bat B5, Sart Tilman B-4000 Liege 1, Belgium*

Abstract

We study the implications of the global $U(1)_R$ symmetry present in minimal lepton flavor violating implementations of the seesaw mechanism for neutrino masses. Our discussion is done in the context of explicit minimal type-I seesaw scenarios, where depending on the R-charge assignment different models can be constructed. We study the charged lepton flavor violating phenomenology of a concrete realization paying special attention to $\mu \rightarrow e\gamma$ and $\mu \rightarrow 3e$.

1 Introduction

The observation of neutrino flavor oscillations constitutes an experimental proof of lepton flavor violation¹⁾. In principle, other manifestations of such effects could be expected to show up in the charged lepton sector as well. However, the lack of a definitive model for neutrino mass generation implies that conclusive

predictions for lepton flavor violating processes can not be made, and even assuming a concrete model realization for neutrino masses, predictions for such effects can only be done if the flavor structure of the corresponding realization is specified.

In this regards the minimal flavor violating hypothesis ^{2, 3, 4)} is a very useful guide for constructing predictive models in which lepton violating signals are entirely determined by the low-energy neutrino data. However minimal lepton flavor violation (MLFV) can not be uniquely implemented and depends on the new physics responsible for neutrino masses. Here considering a type-I seesaw mechanism i.e. taking the new degrees of freedom to be heavy fermionic electroweak singlets (right-handed (RH) neutrinos), we study the implications of the $U(1)_R$ present in MLFV models assuming it is slightly broken. The full analysis is done in the context of a minimal type-I seesaw setup (2 RH neutrinos) where the number of parameters and low energy observables are such that all flavor effects are entirely determined by neutrino observables up to normalizations factors.

2 The setups

The kinetic Lagrangian of the standard model extended with two RH neutrinos exhibits the global $G = U(3)_e \times U(3)_\ell \times U(2)_N$ symmetry. This group can be rewritten as $U(1)_Y \times U(1)_L \times U(1)_R \times G_F$ where $U(1)_{Y,L}$ can be identified with global hypercharge and lepton number whereas the $U(1)_R$ is a “new” global symmetry, already mentioned in the introduction ^{4, 5)}.

The charges associated with this global transformation (hereafter denoted by R) are arbitrary, and thus different R -charge assignments define different models. Here we will explicitly consider the seesaw Lagrangian with a slightly broken $U(1)_R$ and discuss a generic model¹ that arises from a particular R -charge assignment.

Precisely speaking we refer to the following: $R(N_1, \ell_i, e_i) = +1$, $R(N_2) = -1$, $R(H) = 0$ where ℓ_i, e_i and $N_{1,2}$ are respectively the electroweak lepton

¹A second class of models can be constructed in which the small breaking of $U(1)_R$ allows to decouple the lepton number breaking scale from the RH neutrino mass scale. But this decoupling implies also a suppression of the corresponding Yukawa couplings, thus leading to non-observable charged lepton flavor violating effects. For more details see ⁶⁾

doublets, singlets and RH neutrinos. The Lagrangian is thus given by

$$\mathcal{L} = -\bar{\ell}\boldsymbol{\lambda}_1^* N_1 \tilde{H} - \epsilon_\lambda \bar{\ell}\boldsymbol{\lambda}_2^* N_2 \tilde{H} - \frac{1}{2} N_1^T C M N_2 - \frac{1}{2} \epsilon_N N_a^T C M_{aa} N_a + \text{h.c.} \quad (1)$$

The dimensionless $\epsilon_{\lambda,N}$ parameters determine the amount of $U(1)_R$ breaking and thus are tiny, $\tilde{H} = i\sigma_2 H^*$, C is the charge conjugation operator, the $\boldsymbol{\lambda}_a$'s are Yukawa vectors in flavor space and M and M_{aa} are the parameters that define the RH neutrino mass matrix. The diagonalization of the Majorana RH neutrino mass matrix leads to two quasi-degenerate states with masses given by $M_{N_{1,2}} = M \mp \frac{M_{11}+M_{22}}{2} \epsilon_N$ and in the basis in which the RH neutrino mass matrix is diagonal the Yukawa couplings λ_{ka} become $-\frac{(i)^a}{\sqrt{2}} [\lambda_{k1} + (-1)^a \epsilon_\lambda \lambda_{k2}]$ ($k = e, \mu, \tau$ and $a = 1, 2$). In terms of these redefined Yukawa couplings, the effective light neutrino mass matrix, up to $\mathcal{O}(\epsilon_N \epsilon_\lambda^2)$, is given by

$$\mathbf{m}_\nu^{\text{eff}} = -\frac{v^2 \epsilon_\lambda}{M} |\boldsymbol{\lambda}_1| |\boldsymbol{\Lambda}| \left(\hat{\boldsymbol{\lambda}}_1^* \otimes \hat{\boldsymbol{\Lambda}}^* + \hat{\boldsymbol{\Lambda}}^* \otimes \hat{\boldsymbol{\lambda}}_1^* \right), \quad (2)$$

with $\hat{\boldsymbol{\Lambda}}^* = \hat{\boldsymbol{\lambda}}_2^* - \frac{M_{11}+M_{22}}{4M} \frac{\epsilon_\lambda}{\epsilon_N} \hat{\boldsymbol{\lambda}}_1^*$. Note that we have expressed the parameters space vector $\boldsymbol{\lambda}_1$ and $\boldsymbol{\Lambda}$ in terms of their unitary vector $\hat{\boldsymbol{\lambda}}_1$, $\hat{\boldsymbol{\Lambda}}$ and moduli $|\boldsymbol{\lambda}_1|$, $|\boldsymbol{\Lambda}|$. Since $\epsilon_\lambda \ll 1$ small neutrino masses do not require heavy RH neutrinos or small Yukawa couplings, thus potentially implying large lepton flavor violating effects.

It turns out that due to the structure of (2) the vectors $\boldsymbol{\lambda}_1$ and $\boldsymbol{\Lambda}$ can be entirely determined by means of the solar and atmospheric mass scales and mixing angles, up to the factors $|\boldsymbol{\lambda}_1|$ and $|\boldsymbol{\Lambda}|$. The expression depend on the light neutrino mass spectrum, in the normal case they read ⁷⁾

$$\boldsymbol{\lambda}_1 = |\boldsymbol{\lambda}_1| \hat{\boldsymbol{\lambda}}_1 = \frac{|\boldsymbol{\lambda}_1|}{\sqrt{2}} \left(\sqrt{1+\rho} \mathbf{U}_3^* + \sqrt{1-\rho} \mathbf{U}_2^* \right), \quad (3)$$

$$\boldsymbol{\Lambda} = |\boldsymbol{\Lambda}| \hat{\boldsymbol{\Lambda}} = \frac{|\boldsymbol{\Lambda}|}{\sqrt{2}} \left(\sqrt{1+\rho} \mathbf{U}_3^* - \sqrt{1-\rho} \mathbf{U}_2^* \right), \quad (4)$$

where \mathbf{U}_i denote the columns of the leptonic mixing matrix and

$$\rho = \frac{\sqrt{1+r} - \sqrt{r}}{\sqrt{1+r} + \sqrt{r}}, \quad r = \frac{m_{\nu_2}^2}{m_{\nu_3}^2 - m_{\nu_2}^2}. \quad (5)$$

3 Lepton flavor violating processes

With potentially large Yukawa couplings and RH neutrinos in the TeV ballpark, charged lepton flavor violating processes could be expected to have large rates.

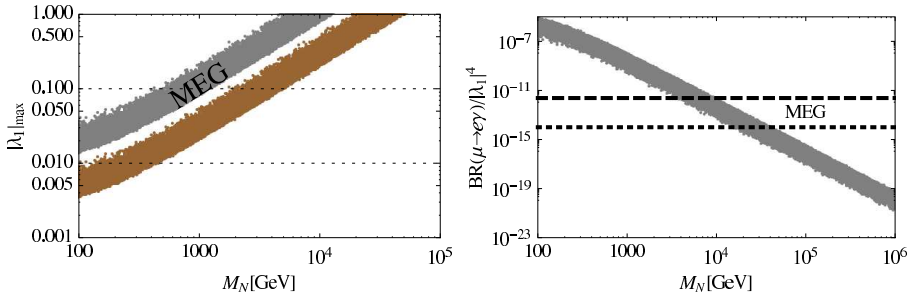


Figure 1: Radiative LFV decay branching ratio $BR(\mu \rightarrow e\gamma)$ for normal light neutrino mass spectra as a function of the common RH neutrino mass. The upper horizontal dashed line indicates the current limit on $BR(\mu \rightarrow e\gamma)$ from the MEG experiment ⁸⁾, whereas the lower one the future experimental sensitivities ⁹⁾.

In what follows we analyze $l_i \rightarrow l_j \gamma$ and $l_i^- \rightarrow l_j^- l_j^+ l_j^+$.

3.1 $l_i \rightarrow l_j \gamma$ processes

The decay branching ratios can be approximated by ⁶⁾:

$$BR(l_i \rightarrow l_j \gamma) \simeq \frac{\alpha}{1024\pi^4} \frac{m_i^5}{M^4} \frac{|\lambda_{\mathbf{1}}|^4}{\Gamma_{\text{Tot}}^{l_i}} \left| \hat{\lambda}_{i1} \hat{\lambda}_{j1}^* \right|^2, \quad (6)$$

where $\Gamma_{\text{Tot}}^{l_i}$ stands for the total decay width of the corresponding decaying charged lepton l_i .

Among these lepton flavor violating processes, presently the $\mu \rightarrow e\gamma$ transition is the most severely constrained. The MEG collaboration recently established an upper bound of 2.4×10^{-12} at the 90% C.L. ⁸⁾. So from now on we focus on that process. To quantify this effect, we randomly generate low energy observables in their 2σ ranges and the parameters $|\lambda_{\mathbf{1}}|$ and M in the ranges $[10^{-5}, 1]$ and $[10^2, 10^6]$ GeV allowing RH neutrino mass splittings in the range $[10^{-8}, 10^{-6}]$ GeV.

The results for the normal mass spectrum case are displayed in figure 1. It can be seen that $BR(\mu \rightarrow e\gamma)$ can reach the current experimental limit reported by the MEG experiment ⁸⁾ for RH neutrino masses $M_N <$

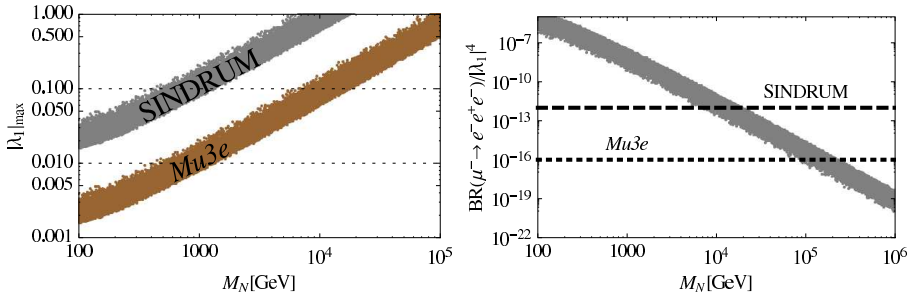


Figure 2: Decay branching ratio $BR(\mu^- \rightarrow e^- e^+ e^-)$ for normal light neutrino mass spectra as a function of common RH neutrino mass. The upper horizontal dashed line indicates the current bound for $\mu^- \rightarrow e^+ e^- e^-$ placed by the SINDRUM experiment ¹¹⁾, whereas the lower one future experimental sensitivities ¹²⁾.

0.1 TeV, 1 TeV, 10 TeV provided $|\lambda_1| \gtrsim 2 \times 10^{-2}, 10^{-1}, 1$, respectively.

3.2 $l_i^- \rightarrow l_j^- l_j^- l_j^+$ processes

The decay branching ratios for these processes have been calculated in ^{10, 6)}. The most constrained process in this case is $\mu^- \rightarrow e^+ e^- e^-$ for which the SINDRUM experiment has placed a bound on the decay branching ratio of 10^{-12} at 90% C.L. ¹¹⁾. Following the same numerical procedure used in the previous section we calculate the decay branching ratio for $\mu^- \rightarrow e^+ e^- e^-$. The results are shown in figure 2. Again, as in the $\mu \rightarrow e\gamma$ case, it can be seen that the decay branching ratio can saturate the current experimental bound for RH neutrino masses $M_N < 0.1$ TeV, 1 TeV, 10 TeV provided $|\lambda_1| \gtrsim 2 \times 10^{-2}, 10^{-1}, 1$, respectively.

4 Conclusion

The presence of an extra global $U(1)_R$ in the seesaw Lagrangian allows the construction of different types of models, all of them determined by the R-charge assignments of the lepton sector. We have considered a concrete realization and analyzed its consequences for the most promising charged lepton flavor violating decays, namely $\mu \rightarrow e\gamma$ and $\mu^- \rightarrow e^- e^+ e^-$. Our analysis shows that

for a large mass range of the lepton flavor violating mediators these processes might be observed in near future experiments.

5 Acknowledgements

I would like to thank D. Aristizabal Sierra and J. F. Kamenik for the fruitful collaboration. D. Aristizabal Sierra also for the help during the preparation of this work.

References

1. T. Schwetz, M. Tortola and J. W. F. Valle, *New J. Phys.* **13**, 109401 (2011) [arXiv:1108.1376 [hep-ph]]; M. C. Gonzalez-Garcia, M. Maltoni and J. Salvado, *JHEP* **1004**, 056 (2010) [arXiv:1001.4524 [hep-ph]].
2. R. S. Chivukula and H. Georgi, *Phys. Lett. B* **188**, 99 (1987).
3. L. J. Hall and L. Randall, *Phys. Rev. Lett.* **65**, 2939 (1990).
4. G. D'Ambrosio, G. F. Giudice, G. Isidori and A. Strumia, *Nucl. Phys. B* **645**, 155 (2002) [hep-ph/0207036].
5. R. Alonso, G. Isidori, L. Merlo, L. A. Munoz and E. Nardi, *JHEP* **1106**, 037 (2011) [arXiv:1103.5461 [hep-ph]].
6. D. Aristizabal Sierra, A. Degee and J. F. Kamenik, arXiv:1205.5547 [hep-ph].
7. M. B. Gavela, T. Hambye, D. Hernandez and P. Hernandez, *JHEP* **0909**, 038 (2009) [arXiv:0906.1461 [hep-ph]].
8. J. Adam *et al.* [MEG Collaboration], *Phys. Rev. Lett.* **107**, 171801 (2011) [arXiv:1107.5547 [hep-ex]].
9. http://meg.icepp.s.u-tokyo.ac.jp/docs/prop_psi/proposal.pdf
10. A. Ilakovac and A. Pilaftsis, *Nucl. Phys. B* **437**, 491 (1995) [hep-ph/9403398].
11. U. Bellgardt *et al.* [SINDRUM Collaboration], *Nucl. Phys. B* **299**, 1 (1988).
12. http://www.physi.uni-heidelberg.de/Forschung/he/mu3e/documents/LOI_Mu3e_PSI.pdf

Search for Hidden Higgs decays in the ATLAS detector

Andrea Gabrielli
INFN, sezione di Roma 1
Dipartimento di Fisica, Universita' di Roma "Sapienza"

Abstract

In this paper, a brief overview of the search for the Higgs boson in Hidden Valley models is given. Hidden Valley models predict Higgs decays to neutral particles, which can be also long lived with decay paths comparable to the LHC detectors dimensions. Decay final states consist of collimated leptons (Lepton Jets) or heavy flavors. Results are presented of a search for Higgs decays to long lived particles in the ATLAS detector at the LHC with a 7 TeV center of mass energy, based on 1.94 fb^{-1} of data collected during 2011.

1 Hidden Valley scenario

Many extensions of the Standard Model (SM) predict a light Higgs ¹⁾, in the mass range $100 - 140 \text{ GeV}c^{-2}$, with decays branching fractions significantly different than the SM ones (Figure 1). An interesting possibility arises if additional light hidden sectors, weakly coupled to the SM, exist.

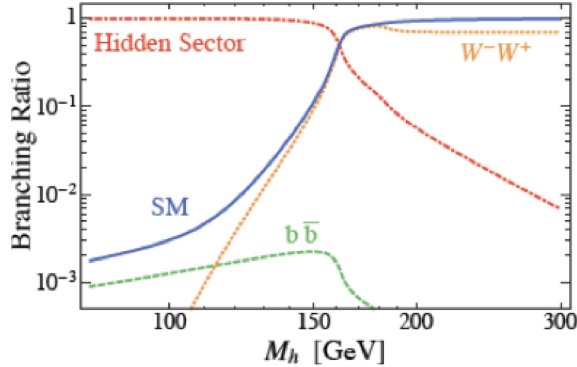


Figure 1: *The Higgs boson can have different Branching Ratios compared to the predictions of SM for low masses of the Higgs, the decay is dominant in the hidden sector.*

These sectors include neutral particles that can be long-lived, with decay lengths comparable or larger than the detector dimensions ^{2) 3) 4) 7) 8)}, and to which the Higgs may decay¹. Possible topological signatures of such extensions of the SM are the clusters of highly collimated charged particles: electrons, muons, pions and heavy quarks. Neutral particles with long decay paths and collimated final states represent, from an experimental point of view, a challenge both for the trigger and for the reconstruction capabilities in the detector due to the finite granularity of the detectors; moreover charged tracks from decay vertices far from the interaction point (IP) will be difficult to reconstruct, missing the central tracking detector information and the main vertex constraint. The ATLAS air core toroid Muon Spectrometer ⁵⁾ (MS) allows to reconstruct charged tracks in a standalone configuration, a crucial feature for detecting tracks not coming from the primary vertex of interaction.

¹These long-lived particles occur in many models, including gauge-mediated extensions of the Minimal Supersymmetric Standard Model (MSSM), MSSM with R-parity violation and the Hidden Valley (HV) scenario.

2 Higgs to v-pions

The first benchmark model studied is the search for the Higgs decay to two pseudoscalar hidden particles "v-pions" ($h_0 \rightarrow \pi_V \pi_V$)^{2) 6)}. Signal Monte Carlo (MC) samples were generated using PYTHIA to simulate gluon-gluon fusion production ($gg \rightarrow h_0$) and decay of the Higgs. Four samples were generated: $m_{h_0} = 120$ and $140 \text{ GeV}c^{-2}$ and for each m_{h_0} two π_V masses of 20 and $40 \text{ GeV}c^{-2}$. The predicted Higgs production cross sections are: $\sigma(m_{h_0} = 120 \text{ GeV}c^{-2}) = 16.6 \text{ pb}$, $\sigma(m_{h_0} = 140 \text{ GeV}c^{-2}) = 12.1 \text{ pb}$, and the branching ratio for h_0 to v-pions is assumed to be 100%. The peculiarity of the final state is the presence of clusters of charged and neutral hadrons in the MS. To detect this signal, you need to use specialized tracking and vertex reconstruction algorithms and dedicated trigger, which uses the first level muon trigger (L1) of ATLAS. The L1 muon trigger requires hits in the middle station to create a low p_T muon Region of Interest (RoI) or hits in both the middle and outer stations for a high p_T RoI. A dedicated trigger (muon RoI cluster trigger) expects a cluster of three or more muon RoIs in a $\Delta R = 0.4$ cone in the MS (Figure 2 a). The vertex reconstruction algorithm uses the structure design of the MDT chambers, which have two multilayers (MLs), the tracks used in the vertex reconstruction are formed by matching single ML segment between the two MLs, using hits in single muon chambers.

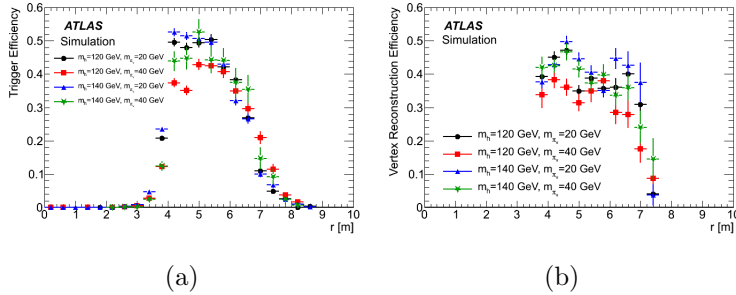


Figure 2: a) Efficiency of the trigger, as a function of the radial decay distance of the π_V b) Vertex reconstruction efficiency for π_V decays in the barrel for events that pass the muon RoI cluster trigger as a function of the radial decay distance.

The algorithm begins by grouping the tracks using a simple cone algorithm with $\Delta R = 0.6$, after the tracks are extrapolated through the magnetic field, and the vertex position is reconstructed as the point in (r, z) (Figure 2 b). The suppression of backgrounds is made possible by requiring two back-to-back vertices ($\Delta R \equiv \sqrt{\Delta\eta^2 + \Delta\phi^2} > 2$) in the muon spectrometer, no calorimeter activity $E_T \leq 30 \text{ GeV}$ in a cone of $\Delta R = 0.7$ and no inner detector tracks with $p_T \geq 5 \text{ GeV}c^{-1}$ within a region of $\Delta\eta \times \Delta\phi = 0.2 \times 0.2$ around the RoI cluster center. These isolation criteria result in a negligible loss in the simulated signal while significantly reducing the backgrounds.

In 1.94 fb^{-1} of pp collision data at a center-of-mass energy of 7 TeV there are not events containing two isolated, back-to-back vertices in the ATLAS muon spectrometer. Since no significant excess over the background prediction is found, exclusion limits for $\sigma_{h_0} BR(h_0 \rightarrow \pi_V \pi_V)$ are set by rejecting the signal hypothesis at the 95% confidence level using the CLs procedure (Figure 3). These limits also apply to models in which the Higgs decays to a pair of weakly-interacting scalars that in turn decay to heavy quark pairs.

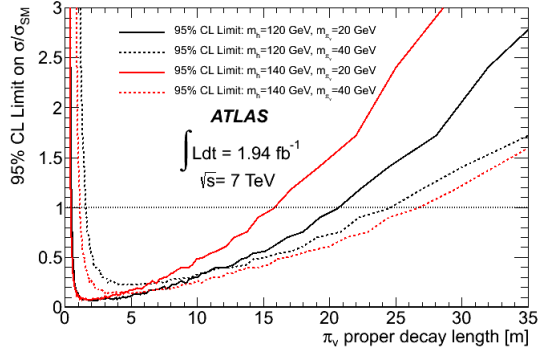


Figure 3: Observed 95% CL upper limit on $\sigma_{h_0} BR(h_0 \rightarrow \pi_V \pi_V) / \sigma_{SM}$ as a function of the π_V proper decay length ($c\tau$), assume $BR(h_0 \rightarrow \pi_V \pi_V) = 100\%$.

3 Higgs to LeptonJets

Another possible characteristic topological signatures with light Higgs of such extensions of the SM ^{7) 8)} are the so called Lepton Jets (LJs)². A LJ is a cluster of highly collimated charged particles: electrons, muons and possibly pions. These arise if light unstable vector boson with masses in the MeV to GeV range (dark or hidden photons, γ_d) reside in the hidden sector and decay predominantly to SM particles. The search presented in this note is focused on long lived LJ containing only muons (MuonJet) The benchmark channel used for this analysis is the simplest Higgs decay scenario with two dark-photons (Figure 4 a) resulting to only two MJs in the final state. The mass of the $\gamma_d = 400 \text{ MeV}c^{-2}$ is chosen to maximize its decay branching fraction to muons (45% Figure 4 b).

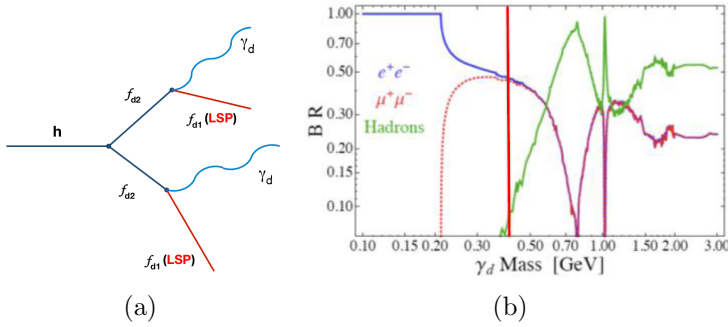


Figure 4: a) The Higgs decays to two hidden fermions (fd_2). Each hidden fermion decays to a γ_d and to a stable (LSP) hidden fermion (fd_1) b) Branching ratio of γ_d as a function of its mass.

The decay branching fractions of γ_d are dictated from its mass and are found to be: 45% e^+e^- , 45% $\mu^+\mu^-$, 10% $\pi^+\pi^-$. For the signal MC simulation the PYTHIA generator was used, linked together with MadGraph and BRIDGE for the production (through gluon fusion) and decay of hidden sector

²The production of LJs can occur through different channels, e.g. in SUSY models, the lightest visible superpartner may decay to the hidden sector.

particles. The SM backgrounds have been generated using PYTHIA (W+Jets, and Z+Jets) and MC@NLO (tt, WW, WZ, and ZZ) while, for the QCD background evaluation, a data driven method has been used. These events are selected using an trigger with 3 muons of $p_T \geq 6 \text{ GeV}c^{-1}$ reconstructed only in the Muon Spectrometer. MJs from γ_d displaced decays are characterized by a pair of muons, not linked to the primary vertex of the event, in a very narrow cone ($\Delta R \leq 0.1$). These objects are reconstructed with a simple clustering algorithm, associating all the muons in cones of opening $\Delta R = 0.2$. Only events with 2 MJs are kept for the subsequent analysis. A certain number of discriminating variables have been studied in order to separate the signal from the background. The main background source, the QCD di-jet production, can be strongly reduced using: calorimeter criteria isolation around the MJ direction, the $\Delta\phi$ (azimuth angle) between the two MJs and the Σp_T for the MJs ³. Finally, to reduce the background coming from cosmic muons a cut on the impact parameters of the muon tracks with respect to the primary interaction vertex is used. This analysis is work in progress, currently have been studied only the decay into muons. The analysis strategy can be applied to more complex signal topologies.

References

1. F. Englert *et al*, Phys. Rev. Lett. **13**, 321 (1964).
2. M. J. Strassler *et al*, Phys. Lett. **B651**, 374 (2007).
3. M. J. Strassler *et al*, Phys. Lett.**B661** , 263-267 (2008).
4. T. Han *et al*, JHEP **07** (2008) 008.
5. The ATLAS Collaboration *et al*, 2008 JINST **3** S08003.
6. The ATLAS Collaboration, CERN-PH-EP-2011-228 arXiv:1203.1303v2 [hep-ex].
7. C. Cheung *et al*, JHEP **04** (2010) 116.
8. A. Falkowski *et al*, JHEP **05** (2010) 077.

³defined as the sum p_{Ts} of the inner detector tracks inside a cone $\Delta R < 0.4$ around the direction of the MJ.

Frascati Physics Series
3RD YOUNG RESEARCHERS WORKSHOP: PHYSICS CHALLENGES IN THE LHC ERA” Frascati,
May 7 and 10, 2012

THE SUPERFIELD FORMALISM IN A 5D SUSY MODEL

J.D. García-Aguilar
A. Pérez-Lorezana

*Departamento de Física, Centro de Investigación y de Estudios Avanzados del I.P.N.
Apdo. Post. 14-740 07000 México D.F., México.*

Abstract

We construct a supersymmetric higher dimensional theory which include Lorentz violation terms in a superfield formalism, to obtain this formalism is necessary to redefine the supersymmetric auxiliary fields.

1 Introduction

In December 2011 the CMS and ATLAS groups presented the latest results on the Higgs searching. They found the possibility to find this particle with a mass between 119 and 130 GeV ^{?)}. A Higgs particle with this mass leads to the famous hierarchy problem in the Standard Model. Supersymmetry ^{?)} (SUSY) and the Extra Dimensional theories (XD) ^{?)} offer some suggestions to solve this problem, unfortunately we do not have any experimental evidence of the existence of them.

The extra dimensional theories introduce one or more space coordinates in the usual theories to try solve some conceptual problems of the Standard Model (SM), however, the compactification process leads to obtain the Kaluza-Klein towers, these towers are composed by an infinity number of modes and one of these correspond to one particle of SM and the others correspond to particles with same charge and spin but different mass ⁴⁾.

By the other hand, SUSY is introduced as a global symmetry of the Lagrangian which transform the fermions to boson and viceversa, that implies the existence at least to one superpartner for each particle of the SM. The particle and its superpartner have same charge and spin but different mass. We have not observed any indication to the existence of these superpartners, for this reason the global symmetry must be broken, but the people do not know a convincing mechanism to obtain this rupture ⁵⁾.

The most of supersymmetric theories can be rewritten in the super-space formalism which was proposed by Salam and Strathdee in 1974 ⁶⁾, this formalism involves the consideration of superfield $\Phi(x, \theta, \bar{\theta})$ defined on an 8-dimensional space which is the product of ordinary spacetime with a 4-dimensional space whose points are labeled by the anticommuting Grassman variables θ_α .

In a previous work we build a SUSY model with one extra dimension in which the Lorentz symmetry is broken in an explicit way, but this symmetry is recovered after the compactification process ⁷⁾. The goal of this work is present the model discussed above in the superfield formalism.

The outline for this work is as follow: In the section 2 we show the convention for Dirac matrices in five dimensions for the model, and rewritten the Dirac Lagrangian on terms of two Weyl spinors. In the section 3 and 4 present the SUSY model on a superfield formalism. Our conclusions are presented in section 6.

2 Spinors in five dimensions.

A massless fermion field is defined as the solution of the equation of motion for the Dirac Lagrangian

$$\mathcal{L} = i\bar{\Psi}\Gamma^M\partial_M\Psi$$

where the gamma matrices (Γ^M) satisfy the Clifford algebra relation

$$\{\Gamma^M, \Gamma^N\} = 2\eta^{MN}\mathbb{I}$$

where \mathbb{I} is the identity matrix and η^{MN} is the Minkowski metric, in this work we use the convention $\eta^{MN} = \text{diag}(1, -1, \dots, -1)$.

In five dimension we use the Weyl basis

$$\Gamma^\mu = \begin{pmatrix} 0 & \sigma^\mu \\ \bar{\sigma}^\mu & 0 \end{pmatrix}, \quad \Gamma^5 = i \begin{pmatrix} -\mathbb{I} & 0 \\ 0 & \mathbb{I} \end{pmatrix}. \quad (1)$$

Therefore, a fermion on five space-time dimension is necessarily a four component spinor and we can see it as a two vector-like of two-component spinors

$$\Psi = \begin{pmatrix} \psi_\alpha \\ \bar{\chi}^{\dot{\alpha}} \end{pmatrix}.$$

Under this decomposition, the 5D Dirac Lagrangian can be rewritten as

$$\mathcal{L} = i\chi\sigma^\mu\partial_\mu\bar{\chi} + i\psi\sigma^\mu\partial_\mu\bar{\psi} - \psi\partial_5\chi + \bar{\chi}\partial_5\bar{\psi} + \text{total derivatives} \quad (2)$$

3 Superfield formalism for a 5D SUSY model.

In this section we will to develop the action

$$S = \int d^5x (\partial_M A^\dagger \partial^M A + \partial_M B^\dagger \partial^M B + i\bar{\Psi}\Gamma^M \partial_M \Psi + P^\dagger P + Q^\dagger Q) \quad (3)$$

in the superfield formalism using the following definition for a chiral superfield

$$\begin{aligned} \Phi(x^\mu, \theta, \bar{\theta}) &= A(x) + \sqrt{2}\theta\chi(x) + \theta^2 F(x) - i(\theta\sigma^\mu\bar{\theta})\partial_\mu A(x) \\ &+ \frac{i}{\sqrt{2}}\theta^2(\partial_\mu\chi(x)\sigma^\mu\bar{\theta}) - \frac{1}{4}\theta^2\bar{\theta}^2\partial_\mu\partial^\mu A(x) \end{aligned}$$

here $\mu = 0, \dots, 3$, A is a complex scalar field, χ is a Weyl spinor, F is an auxiliary field and $\sigma^\mu = (\mathbb{I}, \vec{\sigma})$.

In the last section we saw how a fermion field in five dimensions requires a vector-like treatment and that implies to have two Weyl spinor. For a SUSY transformation each Weyl spinor requires their own complex scalar field and its own auxiliary field, that means the necessity to have two chiral superfields.

Let us define the chiral superfields as

$$\begin{aligned}\Phi &= \Phi(A(x^M), \psi(x^M), F(x^M)) \\ \Omega &= \Omega(B(x^M), \chi(x^M), G(x^M))\end{aligned}$$

where $M = 0 \dots, 3, 5$, A and B are complex scalar fields, ψ and χ are Weyl spinors and F and G are the auxiliary fields.

These superfields can form two 4D Wess-Zumino model

$$S' = \int d^5x (\Phi^\dagger \Phi|_D + \Omega^\dagger \Omega|_D)$$

but these terms not produce the total action, due the difference

$$S - S' = \int d^5x (\partial_5 A^\dagger \partial^5 A + \partial_5 B^\dagger \partial^5 B + i\bar{\Psi}\Gamma^5 \partial_5 \Psi + P^\dagger P + Q^\dagger Q - F^\dagger F - G^\dagger G). \quad (4)$$

However we can consider the following interaction between superfields

$$S_{int} = \int d^5x (\Phi \partial_5 \Omega|_F + h.c.) \quad (5)$$

where

$$\begin{aligned}\Phi \partial_5 \Omega &\supset \theta^2 (F \partial_5 B - G \partial_5 A - \psi \partial_5 \chi) \\ \Phi^\dagger \partial_5 \Omega^\dagger &\supset \bar{\theta}^2 (F^\dagger \partial_5 B^\dagger - G^\dagger \partial_5 A^\dagger + \bar{\chi} \partial_5 \bar{\psi})\end{aligned}$$

The equality $S - S' = S_{int}$ leads to relation

$$\partial_5 A^\dagger \partial^5 A + \partial_5 B^\dagger \partial^5 B + P^\dagger P + Q^\dagger Q - F^\dagger F - G^\dagger G = F \partial_5 B - G \partial_5 A + F^\dagger \partial_5 B^\dagger - G^\dagger \partial_5 A^\dagger$$

that can only be satisfied iff

$$\begin{aligned}F &= P - \partial_5 B^\dagger \\ G &= Q + \partial_5 A^\dagger.\end{aligned} \quad (6)$$

So, the action (3) can be rewritten in terms of superfields considering two Kähler potentials, one superpotential and the redefinition of the auxiliary fields.

4 The Lorentz violation terms.

If we change one parameter in the relations (6) and in the superpotential (5)

$$\begin{aligned} F' &= P - a\partial_5 B^\dagger \\ G' &= Q + a\partial_5 A^\dagger \\ S'_{int} &= a \int d^5x (\Phi\partial_5\Omega|_F + h.c.) \end{aligned}$$

we obtain the action

$$S'' = S_{4D} + S_{x^5}$$

where

$$S_{4D} = \int d^5x (\partial_\mu A^\dagger \partial^\mu A + \partial_\mu B^\dagger \partial^\mu B + i\bar{\Psi}\Gamma^\mu \partial_\mu \Psi + P^\dagger P + Q^\dagger Q) \quad (7)$$

$$S_{x^5} = \int dx^5 (a^2 \partial_5 A^\dagger \partial^5 A + a^2 \partial_5 B^\dagger \partial^5 B + ia\bar{\Psi}\Gamma^5 \partial_5 \Psi) \quad (8)$$

Considering $a = 1 + \kappa$ we can rewritten the action

$$\begin{aligned} S'' &= \int d^5x (\partial_M A^\dagger \partial^M A + \partial_M B^\dagger \partial^M B + i\bar{\Psi}\Gamma^M \partial_M \Psi + P^\dagger P + Q^\dagger Q) \\ &\quad + \int d^5x ((2\kappa + \kappa^2) (\partial_5 A^\dagger \partial^5 A + \partial_5 B^\dagger \partial^5 B) + i\kappa\bar{\Psi}\Gamma^5 \partial_5 \Psi) \end{aligned} \quad (9)$$

the same action and same relations between parameters which leads the Lorentz symmetry violation obtained in our previous work (7).

5 Conclusions

In this work we have presented the superfield formulation for a five dimensional susy theory, this formulation was did for a model which can be Lorentz invariant and presented how a little modification in the superpotential leads to a model which is not Lorentz invariant. These formulations requires redefinitions for the SUSY auxiliary fields, the construction also requires two superfields which means the possibility under certain conditions the rupture of $N = 1$ to $N = 2$ supersymmetries.

References

1. <http://cms.web.cern.ch/org/cms-papers-and-results>
2. S. P. Martin, In *Kane, G.L. (ed.): Perspectives on supersymmetry II* 1-153 [hep-ph/9709356].
3. N. Arkani-Hamed, S. Dimopoulos and G. R. Dvali, Phys. Lett. B **429** (1998) 263 [hep-ph/9803315].
4. A. Perez-Lorenzana, AIP Conf. Proc. **562**, 53 (2001) [arXiv:hep-ph/0008333].
5. D. Bailin and A. Love, *Bristol, UK: IOP (1994) 322 p. (Graduate student series in physics)*
6. A. Salam and J. A. Strathdee, Phys. Rev. D **11**, 1521 (1975).
7. J. D. Garcia-Aguilar, A. Perez-Lorenzana and O. Pedraza-Ortega, AIP Conf. Proc. **1396**, 140 (2011).

$\eta - \eta'$ MIXING ANGLE FROM THE SEMILEPTONIC DECAYS
 $D^+ \longrightarrow \eta(\eta')e^+\nu_e$, $D_s^+ \longrightarrow \eta(\eta')e^+\nu_e$ and $B^+ \longrightarrow \eta(\eta')l^+\nu_l$

Sergi González-Solís
Departament de Física, Universitat Autònoma de Barcelona
Facultat de Ciències, 08193 Bellaterra (Barcelona), Spain.

Abstract

In the present work, we study the semileptonic decays $D^+ \longrightarrow \eta(\eta')e^+\nu_e$, $D_s^+ \longrightarrow \eta(\eta')e^+\nu_e$ and $B^+ \longrightarrow \eta(\eta')l^+\nu_l$ which are suggested to be used to extract the $\eta - \eta'$ mixing angle as well as to test its sensitivity to a variety of hadronic form factors models. Using the quark-flavour basis and neglecting gluonic contributions in the physical states η and η' we find an average value for the mixing angle of $\phi_P = (42.2 \pm 1.1)^\circ$.

1 Introduction and motivation

Studies of the $\eta - \eta'$ mixing angle has lasted for several decades, so it does not seem a trivial issue. Determining the mixing from processes where hadrons are involved is model dependent inevitably, because evaluation of hadronic matrix elements is necessary as we will see. In this work, the $\eta - \eta'$ mixing angle is

revisited from the study of $D_{(s)}^+ \rightarrow \eta(\eta')e^+\nu_e$ and $B^+ \rightarrow \eta(\eta')l^+\nu_l$.

Among the nine possible $q\bar{q}$ combinations containing the light u, d and s quarks, η_8 and η_1 have exactly the same quantum numbers, so it is natural to believe that these states are mixed. This is what precisely happens, the physical states η and η' are mixtures of η_8 and η_1 . This mixing can be expressed in two different bases as a rotation of a given angle, the octet-singlet Eq.(1) and the quark-flavor Eq.(2)

$$\begin{pmatrix} \eta \\ \eta' \end{pmatrix} = \begin{pmatrix} \cos \theta_P & -\sin \theta_P \\ \sin \theta_P & \cos \theta_P \end{pmatrix} \begin{pmatrix} \eta_8 \\ \eta_1 \end{pmatrix} \quad (1)$$

$$\begin{pmatrix} \eta \\ \eta' \end{pmatrix} = \begin{pmatrix} \cos \phi_P & -\sin \phi_P \\ \sin \phi_P & \cos \phi_P \end{pmatrix} \begin{pmatrix} \eta_q \\ \eta_s \end{pmatrix} \quad (2)$$

These parameterizations are related through $\theta_P = \phi_P - \arctan \sqrt{2} \simeq \phi_P - 54.7^\circ$. Due to both phenomenological and theoretical reasons, the mixing is best described by the angle ϕ_P of the quark-flavor bases. Despite the naive quark model describes reasonably well the $q\bar{q}$ states, gluons themselves, can also contribute to the η and η' state's wave function. On the other hand, this question has been extensively investigated but it is still without a definitive conclusion unfortunately, so we have not considered it in this work.

2 Experimental data

Semileptonic decays are good sources to obtain physical quantities, since the final state interaction is absent. This advantage motivates us to obtain the mixing angle ϕ_P via the before cited semileptonic decays instead from radiative and non-leptonic decays as done in ¹⁾. The most recent experimental values of $D^+ \rightarrow \eta(\eta')e^+\nu_e$ by the CLEO Collaboration are ²⁾

$$B(D^+ \rightarrow \eta e^+\nu_e) = (11.4 \pm 0.9 \pm 0.4) \times 10^{-4}, \quad (3)$$

$$B(D^+ \rightarrow \eta' e^+\nu_e) = (2.16 \pm 0.53 \pm 0.07) \times 10^{-4}, \quad (4)$$

which imply

$$R_D^{exp} \equiv \frac{B(D^+ \rightarrow \eta' e^+\nu_e)}{B(D^+ \rightarrow \eta e^+\nu_e)} = 0.19 \pm 0.05, \quad (5)$$

while the updated 2011 PDG fit values ³⁾ of the $D_s^+ \rightarrow \eta(\eta')e^+\nu_e$ are

$$B(D_s^+ \rightarrow \eta e^+\nu_e) = (2.67 \pm 0.29) \times 10^{-2}, \quad (6)$$

$$B(D_s^+ \longrightarrow \eta' e^+ \nu_e) = (9.9 \pm 2.3) \times 10^{-3}, \quad (7)$$

which imply

$$R_{D_s}^{exp} \equiv \frac{B(D_s^+ \longrightarrow \eta' e^+ \nu_e)}{B(D_s^+ \longrightarrow \eta e^+ \nu_e)} = 0.37 \pm 0.10, \quad (8)$$

and of $B^+ \longrightarrow \eta(\eta') l^+ \nu_l$

$$B(B^+ \longrightarrow \eta l^+ \nu_l) = (3.9 \pm 0.8) \times 10^{-5}, \quad (9)$$

$$B(B^+ \longrightarrow \eta' l^+ \nu_l) = (2.3 \pm 0.8) \times 10^{-5}, \quad (10)$$

which imply

$$R_B^{exp} \equiv \frac{B(B^+ \longrightarrow \eta' l^+ \nu_l)}{B(B^+ \longrightarrow \eta l^+ \nu_l)} = 0.59 \pm 0.24. \quad (11)$$

3 The differential decay width and form factors

If D^+ is made up only of $c\bar{d}$, then when the c quark decays into a lepton-neutrino and a d quark, we test the $d\bar{d}$ component of the η and η' . Similarly, if D_s^+ is constituted only of $c\bar{s}$, the c quark decays into a lepton-neutrino and a s quark, we test the $s\bar{s}$ component of the η and η' . Finally, for a pure $u\bar{b}$ B^+ meson, the \bar{b} decays into a lepton-neutrino and a \bar{u} so now we test the $u\bar{u}$ component of the η and η' . The amplitude of these decays reads as ($P = \eta, \eta'$)

$$\mathcal{M}(D_q^+ \longrightarrow P e^+ \nu) = \frac{G_F}{\sqrt{2}} V_{cq} \bar{\nu} \gamma_\mu (1 - \gamma_5) e^+ \langle P(p_P) | \bar{q} \gamma^\mu (1 - \gamma_5) c | D_q^+(p_{D_q^+}) \rangle, \quad (12)$$

with $q = d, s$ for (D^+, D_s^+) respectively, and

$$\mathcal{M}(B^+ \longrightarrow P e^+ \nu) = \frac{G_F}{\sqrt{2}} V_{ub} \bar{\nu} \gamma_\mu (1 - \gamma_5) l^+ \langle P(p_P) | \bar{b} \gamma^\mu (1 - \gamma_5) u | B^+(p_{B^+}) \rangle, \quad (13)$$

for the B^+ . In the amplitudes we have a pure leptonic Standard Model interaction vertex, but there is no way to write down all the underlying physics of the hadronic matrix element (M.E.). Fortunately, we could parameterize it as in Eq.(14) by functions which gives us the properties of the interaction, the so-called form factors

$$\text{M.E.} = \left(P^\mu - \frac{m_H^2 - m_P^2}{q^2} q^\mu \right) f_+^{H \rightarrow P}(q^2) + \frac{m_H^2 - m_P^2}{q^2} q^\mu f_0^{H \rightarrow P}(q^2), \quad (14)$$

where $H = D_{(s)}^+, B^+, P^\mu = (p_H + p_P)^\mu$, $q^\mu = (p_H - p_P)^\mu$ and q^2 is the dilepton invariant mass while $f_+(q^2)$ and $f_0(q^2)$ are the vector and scalar form factors respectively. The differential decay width of $H \rightarrow Pl^+\nu_l$ in the $m_l \rightarrow 0$ is given by

$$\frac{d\Gamma(H \rightarrow Pl^+\nu_l)}{dq^2} = \frac{G_F^2 |V_{cq}(V_{ub})|^2}{24\pi^3} |\mathbf{p}_P|^3 |f_+^{H \rightarrow P}(q^2)|^2, \quad (15)$$

where $\mathbf{p}_P = [(m_H^2 + m_P^2 - q^2)^2 - 4m_H^2 m_P^2]^{1/2} / 2m_H$.

Assuming the isospin symmetry between the u and d quarks, we have

$$f_+^{D^+(B^+) \rightarrow \eta}(q^2) \propto \cos \phi f_+^{D^+(B^+) \rightarrow \eta_{d\bar{d}(u\bar{u})}}(q^2) \approx \cos \phi f_+^{D^+(B^+) \rightarrow \pi}(q^2), \quad (16)$$

$$f_+^{D^+(B^+) \rightarrow \eta'}(q^2) \propto \sin \phi f_+^{D^+(B^+) \rightarrow \eta'_{d\bar{d}(u\bar{u})}}(q^2) \approx \sin \phi f_+^{D^+(B^+) \rightarrow \pi}(q^2), \quad (17)$$

while for the transition form factors of $D_s \rightarrow \eta(\eta')$ we have

$$f_+^{D_s^+ \rightarrow \eta}(q^2) = -\sin \phi f_+^{D_s^+ \rightarrow \eta_s}(q^2), \quad f_+^{D_s^+ \rightarrow \eta'}(q^2) = \cos \phi f_+^{D_s^+ \rightarrow \eta_s}(q^2). \quad (18)$$

The most common form factor to parameterize the q^2 dependence has been the single pole, $n = 1$ in Eq.(19), where the pole is the lowest mass resonance formed by the initial and final state hadron. Furthermore, I have considered two more form factors, the dipole where $n = 2$ in Eq.(20) and the Becirovic-Kaidalov Eq.(20).

$$f_+^{D_{(s)}^+, B^+ \rightarrow \pi}(q^2) = \frac{f_+^{D_{(s)}^+, B^+ \rightarrow \pi(\eta_s)}(0)}{\left(1 - q^2/m_{D_{(s)}^*, B^*}^2\right)^n}, \quad (19)$$

$$f_+^{D^+, B^+ \rightarrow \pi}(q^2) = \frac{f_+^{D^+, B^+ \rightarrow \pi}(0)}{\left(1 - q^2/m_{D^*, B^*}^2\right) \left(1 - \alpha_{D\pi, B\pi} q^2/m_{D^*, B^*}^2\right)}, \quad (20)$$

To eliminate uncertainties in V_{cq}, V_{ub} and $f_+(0)$ we calculate ratios of branching, that is why in Table 1 only the relevant input parameters are shown.

4 Theoretical predictions

Theoretical predictions for the ratio of branching ratios are given by

$$R_H^{th} = \frac{B(H \rightarrow \eta' l^+ \nu_l)}{B(H \rightarrow \eta l^+ \nu_l)} = \frac{\int_0^{(m_H - m_{\eta'})^2} dq^2 \frac{d\Gamma(H \rightarrow \eta' l^+ \nu_l)}{dq^2}}{\int_0^{(m_H - m_\eta)^2} dq^2 \frac{d\Gamma(H \rightarrow \eta l^+ \nu_l)}{dq^2}}, \quad (21)$$

Table 1: *Input parameters necessary in the Becirovic-Kaidalov form factor.*

Method	α_{D_π}	α_{B_π}
LCSR I ⁴⁾	$0.01^{+0.011}_{-0.07}$	$0.32^{+0.21}_{-0.07}$
LCSR II ⁵⁾		0.53 ± 0.06
Lattice I	0.44 ± 0.04 ⁶⁾	0.63 ± 0.05 ⁷⁾
Lattice II ⁸⁾	0.27 ± 0.14	0.40 ± 0.15
Lattice III ⁸⁾	0.36 ± 0.16	0.45 ± 0.17
CLEO ⁹⁾	$0.37^{+0.20}_{-0.31}$	
BELLE ¹⁰⁾	0.10 ± 0.21	

Table 2: *Mixing angle from each R_H considered depending on the form factor.*

Form factor	R_{D^+}	$R_{D_s^+}$	R_{B^+}
Pole	$\phi_P = (42.0 \pm 3.8)^\circ$	$\phi_P = (40.5 \pm 3.8)^\circ$	$\phi_P = (41.3 \pm 5.8)^\circ$
Dipole	$\phi_P = (44.8 \pm 3.8)^\circ$	$\phi_P = (37.7 \pm 3.8)^\circ$	$\phi_P = (45.1 \pm 5.8)^\circ$
LCSR I	$\phi_P = (42.0 \pm 3.8)^\circ$		$\phi_P = (41.8 \pm 5.8)^\circ$
LCSR II			$\phi_P = (42.3 \pm 5.8)^\circ$
Lattice I	$\phi_P = (43.0 \pm 3.8)^\circ$		$\phi_P = (42.7 \pm 5.8)^\circ$
Lattice II	$\phi_P = (42.6 \pm 3.8)^\circ$		$\phi_P = (42.7 \pm 5.8)^\circ$
Lattice III	$\phi_P = (42.8 \pm 3.8)^\circ$		$\phi_P = (42.1 \pm 5.8)^\circ$
CLEO	$\phi_P = (42.9 \pm 3.8)^\circ$		
BELLE	$\phi_P = (42.2 \pm 3.8)^\circ$		
weighted	$\phi_P = (42.8 \pm 1.3)^\circ$	$\phi_P = (39.1 \pm 2.7)^\circ$	$\phi_P = (42.5 \pm 2.2)^\circ$

which by equating to their respective experimental values allow us to extract the $\eta-\eta'$ mixing angle. So, once the relative phase space integrals are calculated and the ratio of η' and η form factors is integrated over the appropriate range in q^2 we obtain the results shown in Table 2 for each of the semileptonic decays considered. The combined result which takes into account the three weighted averaged values in Table 2 yields

$$\phi_P = (42.2 \pm 1.1)^\circ. \quad (22)$$

Finally, from Table 2, we have seen that the mixing angle is not sensitive to the form-factor parametrization.

5 Conclusions

To sum up, we have obtained an average value of $\phi_P = (42.2 \pm 1.1)^\circ$ for the $\eta - \eta'$ mixing angle from studying the semileptonic decays $D_{(s)}^+ \rightarrow \eta(\eta')e^+\nu_e$ and $B^+ \rightarrow \eta(\eta')l^+\nu_l$. This value is in accordance with the results obtained by recent estimates, see for example ¹). We have also seen that present data on these decays is not sensitive to the form-factor parametrization.

6 Acknowledgements

I would thank Rafel Escribano who has lately dedicated part of his time to me and for giving me the opportunity to present this work at the XVI Frascati Spring School "Bruno Touschek" 2012. I would also thank the Laboratori Nazionale di Frascati for the hospitality during the congress.

References

1. R. Escribano, Eur.Phys.J. C **65**, 467-473, (2010). R. Escribano and J. Nadal, JHEP05 (2007) 006. C.E. Thomas, JHEP10 (2007) 026.
2. J. Yelton *et al.* (Cleo Collaboration), Phys. Rev. D **84**, 032001 (2011).
3. K. Nakamura *et al.* (Particle Data Group), J.Phys. G **37**, 075021 (2010) and 2011 partial update for the 2012 edition.
4. A. Khodjamirian, R. Ruckl, S. Weinzierl, C.W. Winhart, O. Yakovlev, Phys.Rev. D **62**, 114002, (2000).
5. G. Duplancic *et al.* JHEP04 (2008) 014.
6. C. Aubin *et al.* Phys.Rev.Lett **94**, 011601, (2005).
7. M. Okamoto *et al.* Nucl.Phys.Proc.Suppl. **140**, 461-463, (2005).
8. A. Abada, D. Becirevic, Ph. Boucaud, J.P. Leroy, V. Lubicz, F. Mescia, Nucl.Phys. B **619**, 565-587, (2011).
9. GS. Huang *et al.* Phys.Rev.Lett **94**, 0111802, (2005).
10. L. Widhalm *et al.* Phys.Rev.Lett. D **97**, 061804, (2006).

Frascati Physics Series
3rd YOUNG RESEARCHERS WORKSHOP: “Physics Challenges in the LHC Era”
Frascati, May 7 and 10, 2012

Search for Higgs boson in the four lepton final state with the ATLAS experiment

Valerio Ippolito
Sapienza Università di Roma & INFN Sezione di Roma / CERN

Abstract

Results of a search for the Standard Model Higgs boson at the ATLAS experiment in the decay channel $H \rightarrow ZZ^{(*)} \rightarrow 4\ell$ where $\ell = e, \mu$ are presented. Data collected in $p-p$ collisions at $\sqrt{s} = 7$ TeV for a total integrated luminosity of about 5 fb^{-1} are compared to the Standard Model expectations and upper limits on the production cross section of a SM Higgs boson in the mass range $100 - 600$ GeV are set.

1 Event selection

A search for the Standard Model Higgs boson has been performed at the ATLAS experiment in its decay channel $H \rightarrow ZZ^{(*)} \rightarrow 4\ell$ where $\ell = e, \mu$, using about 5 fb^{-1} of pp collision data collected in 2011 at the LHC ¹).

Events are selected using single and dilepton triggers, with a single lepton threshold of transverse momentum $p_T > 18$ GeV for muons and of transverse energy $E_T > 20 \div 22$ GeV for electrons, depending on LHC instantaneous luminosity, and dilepton trigger thresholds of $p_T > 10$ GeV and $E_T > 12$ GeV, respectively.

Leptons are selected if they have $p_T > 7$ GeV, pseudorapidity $|\eta| < 2.7$ (muons) or $|\eta| < 2.47$ (electrons) and if they are isolated (low energy deposit in the calorimeter and $\sum p_T$ of inner detector tracks lying within a cone open around the lepton). Higgs candidates are reconstructed searching for two same-flavour opposite-charge lepton pairs, with an additional $p_T > 20$ GeV requirement on two of the leptons, a cut on the invariant mass of the lepton pair Z_1 closest to the Z mass $|m_{Z_1} - m_Z| < 15$ GeV and a $m_{4\ell}$ -dependent cut on the (possibly virtual) second lepton pair Z_2 . The significance of the transverse impact parameter d_0 of the two lowest p_T leptons must be compatible with their provenance from the primary interaction vertex, to reject $Z + bb$ backgrounds.

The signal reconstruction and selection efficiencies for $m_H = 130$ GeV ($m_H = 360$ GeV) are 27% (60%) for the 4μ channel, 18% (52%) for the $2e2\mu$ channel and 14% (45%) for the $4e$ channel. With the integrated luminosity collected in 2011, the expected yield for the 130 GeV mass hypothesis is 1.00 ± 0.17 signal events in the 4μ channel, 1.22 ± 0.21 in the $2e2\mu$ channel and 0.43 ± 0.08 events in the $4e$ channel.

2 Backgrounds

Relevant backgrounds to this search are $pp \rightarrow ZZ^{(*)} \rightarrow 4\ell$, $Z + jj$ and $t\bar{t}$. The last two backgrounds are strongly suppressed by the isolation cuts on the four leptons and by the m_{Z_1} and m_{Z_2} cuts, while the irreducible background $pp \rightarrow ZZ^{(*)} \rightarrow 4\ell$ has the same final state and similar kinematics as the signal, thus it gives the dominant contribution to the overall background.

Background estimation is done both using Monte Carlo (MC) simulation and data-driven techniques (extrapolating from background-enriched control regions). The irreducible background is estimated from MC, with an assigned systematic uncertainty on its yield of 15%. The $Z + jj$ background is estimated from a data sample obtained selecting events with a Z boson plus another lepton pair, without applying isolation and impact parameter cuts on these two

leptons; a systematic uncertainty of $20 \div 40\%$ has been assigned to its yield, depending on the flavour of the jets. The $t\bar{t}$ background is estimated from MC and its normalization has been verified with a control sample of opposite sign electron–muon pairs with mass consistent with m_Z and two additional same–flavour leptons.

3 Results

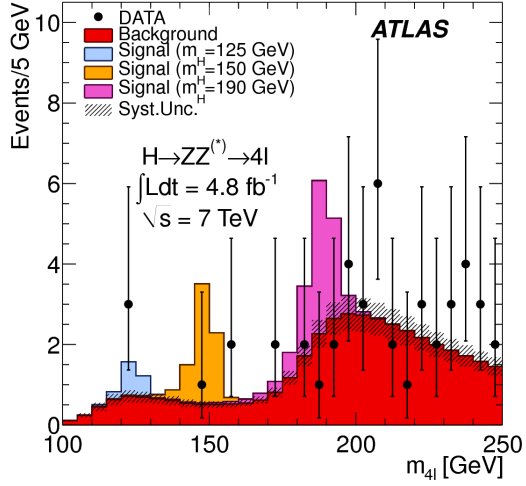
Figure 1 shows the invariant mass distribution of the selected Higgs candidates; 71 events in the full mass range $100 \div 600$ GeV are observed, while expecting 62 ± 9 from background.

Limits on m_H obtained from these distributions are shown in Fig. 2. Three excesses of events with respect to the background–only hypothesis for Higgs boson masses of 125 GeV, 244 GeV and 500 GeV are observed, with local significances of 2.1, 2.2 and 2.1 standard deviations. Combining this result with all the other ATLAS Higgs searches ²⁾, the limit shown in Fig. 3 is obtained: a SM Higgs boson is excluded at the 95% confidence level in the mass ranges from 110.0 GeV to 117.5 GeV, 118.5 GeV to 122.5 GeV, and 129 GeV to 539 GeV.

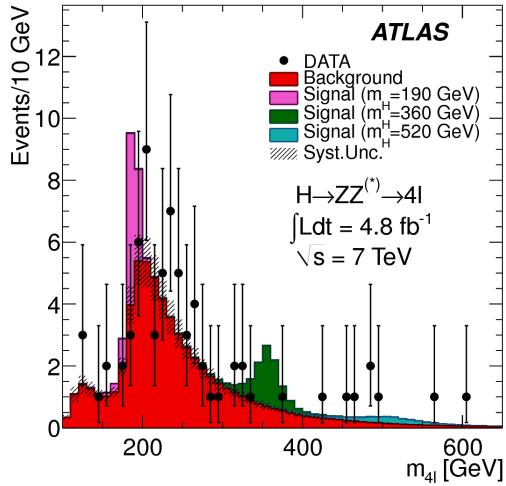
An excess of events is observed in the combination around $m_H = 126$ GeV, with a local significance of 2.5 standard deviations, the main contributions being those coming from $H \rightarrow \gamma\gamma$ and $H \rightarrow ZZ^{(*)} \rightarrow 4\ell$. Results of the analysis of 2012 data, together with the 2011 data analysis, will allow to either exclude or confirm the nature of this excess.

References

1. The ATLAS Collaboration, “Search for the Standard Model Higgs boson in the decay channel $H \rightarrow ZZ^{(*)} \rightarrow 4\ell$ with 4.8 fb^{-1} of pp collision data at $\sqrt{s} = 7$ TeV with ATLAS”, Phys. Lett. B710 (2012) 383-402
2. The ATLAS Collaboration, “An update to the combined search for the Standard Model Higgs boson with the ATLAS detector at the LHC using up to 4.9 fb^{-1} of pp collision data at $\sqrt{s} = 7$ TeV”, ATLAS-CONF-2012-019



(a)



(b)

Figure 1: Invariant mass of the reconstructed Higgs candidates (black dots), with overlaid the background expectation (red histogram) and the signal expectation for various Higgs mass hypotheses, in the low mass range (left) and in the full mass range considered by this analysis (right).

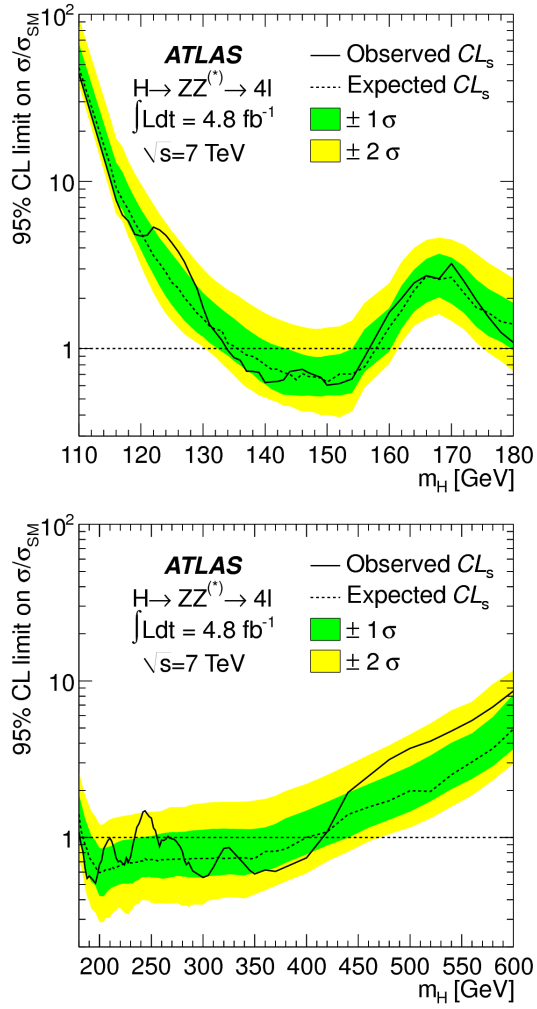


Figure 2: Observed (full line) and expected (dashed line) 95% CL upper limits on the SM Higgs boson production cross section divided by the Standard Model expectation as a function of m_H , obtained from the $H \rightarrow ZZ^{(*)} \rightarrow 4\ell$ analysis.

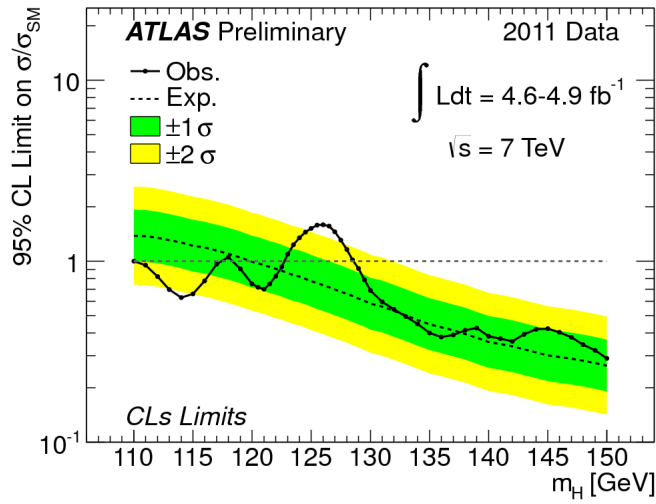
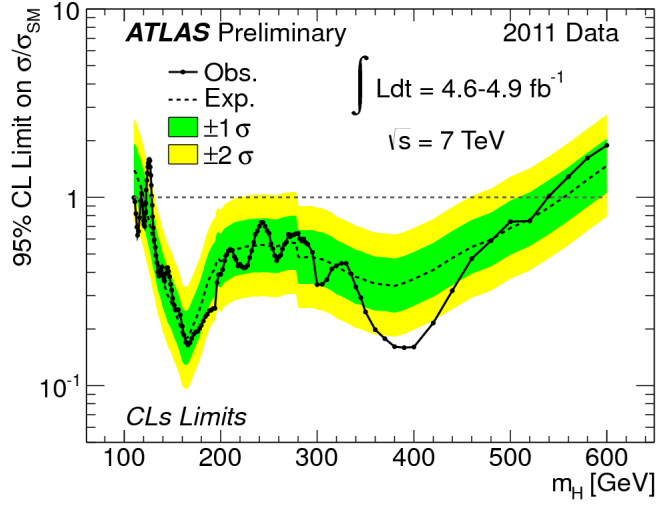


Figure 3: Observed (full line) and expected (dashed line) 95% CL upper limits on the SM Higgs boson production cross section divided by the Standard Model expectation as a function of m_H , obtained combining all ATLAS Higgs searches.

Frascati Physics Series
3rd YOUNG RESEARCHERS WORKSHOP: “Physics Challenges in the LHC Era”
Frascati, May 7 and 10, 2012

ANISOTROPY IN THE COSMIC RADIATION AT TEV ENERGY

Roberto Iuppa

*University of Tor Vergata and INFN, sez.ne Roma Tor Vergata
via della Ricerca Scientifica 1, Rome - 00133, Italy*

Abstract

In recent years very important results were obtained from cosmic ray experiments about the arrival direction distribution of primaries in the TeV energy range. As most of these particles are charged nuclei, they are deflected by the magnetic field they pass through before reaching the Earth surface, the effect of the Lorentz force being inversely proportional to the particle energy. As far as the local interstellar medium is known, the gyroradius of a 10 TeV proton is expected to be only 100 a.u., small enough to make the arrival direction distribution isotropic. Since 1930s a ”large scale” (90-120) anisotropy is known to exist, generally interpreted as the combined effect of sources far away and magnetic fields nearby. Nonetheless, in the last decade experiments like Tibet-ASg, Milagro, ARGO-YBJ and IceCube discovered structures as wide as 10-30 all over the sky at 10 TeV energy, what is unexplainable within the standard model of cosmic rays. In this paper a review of the most recent experimental results about cosmic ray anisotropy is given, together with the status of the

art of theoretical efforts aimed at interpreting them within the current cosmic ray paradigm.

1 Introduction

As CRs are mostly charged nuclei, their paths are deflected and highly isotropized by the action of galactic magnetic field (GMF) they propagate through before reaching the Earth atmosphere. The GMF is the superposition of regular field lines and chaotic contributions and the local total intensity is supposed to be $B = 2 \div 4 \mu\text{G}^{-1}$). In such a field, the gyro-radius of CRs is given by $r_{a.u.} \approx 100 R_{\text{TV}}$, where $r_{a.u.}$ is in astronomic units and R_{TV} is the rigidity in TeraVolt. Clearly, there is very little chance of observing a point-like signal from any radiation source below 10^{17}eV , as they are known to be at least several hundreds parsecs away.

If it is true that magnetic fields are the most important “isotropizing” factor when they randomly vary on short distances, it is clear as much that some particular features of the magnetic field at the boundary of the solar system or farther might focus CRs along certain lines and the observed arrival direction distribution turns out to be consequently an-isotropic.

Different experiments observed an energy-dependent “*large scale*” anisotropy with amplitude spanning 10^{-4} to 10^{-3} , from tens GeV to hundreds TeV, suggesting the existence of two distinct broad regions, an excess named “*tail-in*” (distributed around 40° to 90° in Right Ascension (R.A.) and a deficit named “*loss cone*” (distributed around 150° to 240° in R.A.).

Moreover, in the last decade smaller excesses ($\sim 30^\circ$ wide) were found to exist in the CR arrival direction distribution.

The origin of the galactic CR anisotropy is still unknown, but the study of its evolution over the energy spectrum has an important valence to understand the propagation mechanisms and the structure of the magnetic fields through which CRs have traveled.

2 Experimental results

In 2006 the Tibet AS γ experiment, located at Yangbajing (4300 m a.s.l.), published the first 2D high-precision measurement of the CR anisotropy in the

Northern hemisphere in the energy range from few to several hundred TeV 2). In the figure 1 the CR intensity map observed by Tibet AS γ is shown (panel (a)), together with some theoretical model. The Tibet AS γ collaboration carried out the first measurement of the energy and declination dependences of the R.A. profiles in the multi-TeV region with a single EAS array, revealing finer details of the known anisotropy. They found that the first harmonic amplitude is remarkably energy-independent in the range 4 - 53 TeV and all the components of the anisotropy fade out for CR energy higher than a few hundred TeV, showing a co-rotation of galactic CRs with the local Galactic magnetic environment.

The Milagro collaboration published in 2009 a 2D display of the sidereal anisotropy projections in R.A. at a primary CR energy of about 6 TeV 3). They observed a steady increase in the magnitude of the signal over seven years, in disagreement with the Tibet AS γ results 4). It is worth noting that the energy at which the Tibet AS γ and Milagro results were obtained (~ 10 TeV) is too high for Sun effects play an important role.

In 2007, modeling the large scale anisotropy of 5 TeV CR, the Tibet-AS γ collaboration ran into a “skewed” feature over-imposed to the broad structure of the so-called tail-in region 5). They modeled it with a couple of intensity excesses in the hydrogen deflection plane 6, 7), each of them 10° - 30° wide. A residual excess remained in coincidence with the helio-tail. See the figure 1 (d) and its caption for more details.

Afterwards the Milagro collaboration claimed the discovery of two localized regions of excess 10 TeV CRs on angular scales of 10° with greater than 12σ significance 8). The figure 2 reports the pre-trial significance map of the observation. Regions “A” and “B”, as they were named, are positionally consistent with the “skewed feature” observed by Tibet-AS γ .

The strongest and most localized of them (with an angular size of about 10°) coincides with the direction of the helio-tail. The fractional excess of region A is $\sim 6 \times 10^{-4}$, while for region B it is $\sim 4 \times 10^{-4}$. The deep deficits bordering the excesses are due to a bias in the reference flux calculation. This effect slightly underestimates the significance of the detection. The Milagro collaboration excluded the hypothesis of gamma-ray induced excesses. In addition, they showed the excess over the large scale feature without any data handling (see the figure 2 of 8).

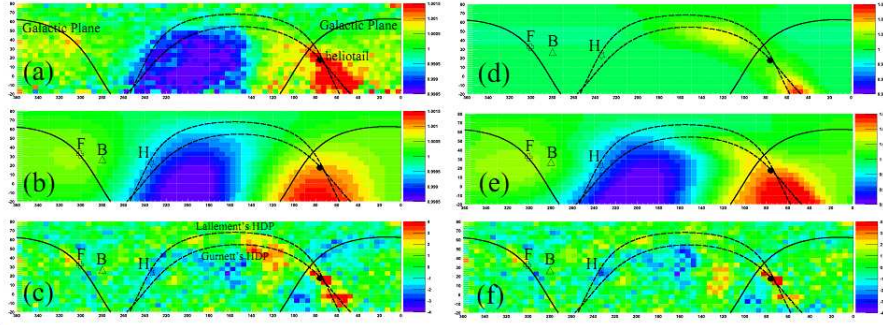


Figure 1: Anisotropy maps of galactic CRs observed and reproduced at the modal energy of 7 TeV by the Tibet-AS γ experiment ⁴). (a): the observed CR intensity; (b): the best-fit large scale component; (c): the significance map of the residual anisotropy after subtracting the large scale component; (d): the best-fit medium scale component; (e): the best-fit large+medium scale components; (f): the significance map of the residual anisotropy after subtracting the large and the medium scale component. The solid black curves represent the galactic plane. The dashed black curves represent the Hydrogen Deflection Plane. The helio-tail direction is indicated by the black filled circle. The open cross and the inverted star with the attached characters “F” and “H” represent possible orientations of the local interstellar magnetic field. The open triangle with “B” indicates the orientation of the best-fit bi-directional cosmic-ray flow obtained in the reference ⁴).

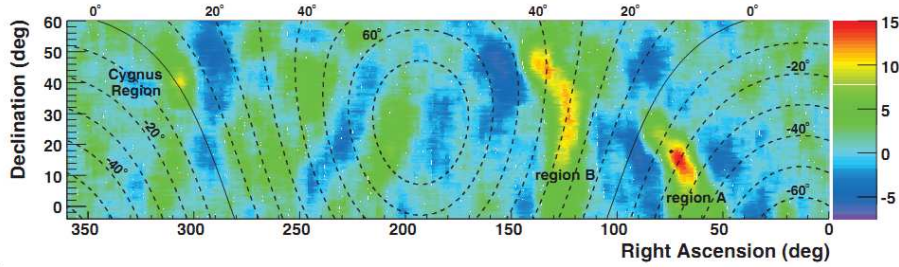


Figure 2: Significance map for the Milagro data set without any cuts to remove the hadronic CR background. A 10° bin was used to smooth the data, and the color scale gives the statistical significance. The solid line marks the Galactic plane, and every 10° in Galactic latitude are shown by the dashed lines. The black dot marks the direction of the helio-tail, which is the direction opposite the motion of the solar system with respect to the local interstellar matter.

The excesses in both regions are harder than the spectrum of the isotropic part of CRs.

Easy to understand, more beamed the anisotropies and lower their energy, more difficult to fit the standard model of CRs and galactic magnetic field to experimental results. In addition, the observation of a possible small angular scale anisotropy region contained inside a larger one rely on the capability for suppressing the smooth global CR anisotropy at larger scales without, at the same time, introducing effects of the analysis on smaller scales.

Nonetheless, this observation has been confirmed by the ARGO-YBJ experiment ^{9, 10)} at median energy of the isotropic CR proton flux of about $E_p^{50} \approx 1.8$ TeV (mode energy ≈ 0.7 TeV)

3 Models and interpretations

Some authors suggested that the large scale anisotropy can be explained within the diffusion approximation taking into account the role of the few most nearby and recent sources ^{11, 12)}. Other studies suggest that a non-di-polar anisotropy could be due to a combined effect of the regular and turbulent GMF ¹³⁾, or to local uni- and bi-dimensional inflows ⁴⁾. In particular the authors modeled the observed anisotropy by a superposition of a large, global anisotropy and a midscale one. The first one is proposed to be generated by galactic CRs interacting with the magnetic field in the local interstellar space surrounding the heliosphere (scale ~ 2 pc).

About the medium scale anisotropy, no theory of CRs in the Galaxy exists yet which is able to explain few degrees anisotropies in the rigidity region 1-10 TV leaving the standard model of CRs and that of the local galactic magnetic field unchanged at the same time. All the solutions proposed to explain the phenomenon are too complex to fit in this work. For quite a complete review see ¹⁴⁾.

4 Conclusions

Current experimental results show that the main features of the anisotropy are uniform in the energy range (10^{11} - 10^{14} eV). Structures are there in every region of the harmonic domain down to angular scales as narrow as 10° . So far, no theory of CRs in the Galaxy exists which is able to explain both large

scale and few degrees anisotropies leaving the standard model of CRs and that of the local galactic magnetic field unchanged at the same time.

5 Acknowledgements

The author wishes to thank Prof. R. Santonico and Dr. G. Di Sciascio for their support in data analysis and critical review of theoretical models.

References

1. Beck R., *Space Sci. Rev.*, **99**, 243 (2001)
2. Amenomori M. et al., *Science*, **314**, 439 (2006).
3. Abdo A.A. et al., *ApJ*, **698**, 2121 (2009).
4. Amenomori M. et al., *Astrophys. Space Sci. Trans.*, **6**, 49 (2010).
5. Amenomori M. et al., *AIP Conf. Proc.*, **932**, 283 (2007).
6. Gurnett D.A. et al., *AIP Conf. Proc.*, **858**, 129 (2006).
7. Lallement R. et al., *Science*, **307**, 1447 (2005).
8. Abdo A.A. et al., *Phys. Rev. Lett.*, **101**, 221101 (2008).
9. Di Sciascio G. and Iuppa R., *Proc. of the 32th ICRC*, Beijing, CH; **0507** (2011).
10. Di Sciascio G. and Iuppa R., [arXiv:1112.0666]
11. Blasi P. and Amato E., arXiv:1105.4521 and arXiv:1105.4529 (2011).
12. Erlykin A.D. and Wolfendale A.W., *Astropart. Phys.*, **25**, 183 (2006).
13. Battaner E. et al *ApJ* **703**, L90 (2009).
14. G. Di Sciascio and R. Iuppa, "On the observation of the Cosmic Ray Anisotropy below 10^{15} eV", to appear in the book "Cosmic Rays: Composition, Physics and Emissions", Nova Science Publishers, Inc., New York (2012).

Model of the $B^0 \rightarrow D^* \omega \pi$ and status of Belle analysis

Dmitry Matvienko
Budker Institute of Nuclear Physics, Novosibirsk

Abstract

We construct a model of the $B^0 \rightarrow D^* \omega \pi$ decay, in which the decay amplitude is a sum of the intermediate $\omega \pi$ and $D^* \pi$ -states with different spins and perform MC simulation based on the obtained expressions. This model is convenient for Dalitz plot analysis. Using the Belle data on $\Upsilon(4S) \rightarrow B \bar{B}$, corresponding to an integrated luminosity of 711 fb^{-1} , we report a status of analysis of the $B^0 \rightarrow D^* \omega \pi$ decay.

1 Introduction

The $B^0 \rightarrow D^* \omega \pi$ decay is interesting from the point of view of the spectroscopy of excited D -states (referred to as D^{**} -states).

The D^{**} -states have been studied in both semileptonic and hadronic B -decays¹). One possible way of D^{**} production is via $B \rightarrow D^* \omega \pi$. Here,

	$\mathcal{L}, \text{fb}^{-1}$	$\mathcal{B} \times 10^{-3}$
CLEO	9	$2.9 \pm 0.3(\text{stat}) \pm 0.4(\text{syst})$
BaBar	211	$2.88 \pm 0.21(\text{stat}) \pm 0.31(\text{syst})$
This work	711	–

Table 1. *Integrated luminosity and branching fraction for different experiments.*

D^{**} production is described by the W vertex instead of the transition Isgur-Wise functions, which describe these states in the $D^{(*)}\pi\pi$ modes. This channel has been first observed by the CLEO ²⁾ and BaBar ³⁾ collaborations, the latter finding an enhancement in $D^*\pi$ mass due to the broad $D_1(2430)^0$ -state, representing a P -wave of a D meson. The integrated luminosities and the measured branching fraction for these experiments as well as for our Belle analysis are presented in Table 1.

Moreover, the light mesons, decaying to the $\omega\pi$ final state (e.g., virtual $\rho_v(770)$, $\rho(1450)$, $\rho(1700)$ and so on), appear in the color-favored mode of this process. Thus, a possible contribution of these resonant structures to the total branching fraction can be measured. Of special interest are studies of the $\rho_v(770)$, $\rho(1450)$ and $\rho(1700)$ contributions. Before, the $\rho(1450)$ -state in this mode was observed in B -decays by CLEO only ²⁾, but without the $\rho_v(770)$ contribution in the fit. By now, the $\rho(1700)$ -state has not yet been observed in B -decays.

2 A model of $B^0 \rightarrow D^*\omega\pi$ decay

Let us discuss kinematic properties of the considered process. There are six particles in the final state, namely, D^0 and π^+ from the D^{*+} decay, π^+ , π^- and π^0 from the ω decay and π^- from the \bar{B}^0 decay. The latter is described by two invariant masses squared of the $D^*\pi$ ($m_{D^*\pi}^2$) and $\omega\pi$ ($m_{\omega\pi}^2$) systems. Moreover, there are two angles, describing the decay of the vector D^* and two angles for the ω . Thus, we have six-dimensional phase space. However, we can choose different bases of these variables. In our study ⁴⁾ we use two bases, describing $\omega\pi$ and $D^*\pi$ -states, respectively. In Fig. 1 we show a definition of the angles for the $\omega\pi$ -resonances.

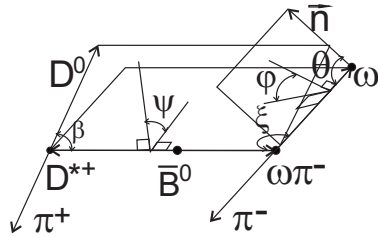


Figure 1. Complete visual definition of the angles for the $\omega\pi$ -resonances. The angles θ and ϕ are defined in the ω rest frame, the angles β and ψ are defined in the D^* rest frame and the angle ξ is defined in the $\omega\pi$ rest frame.

A similar decay scheme takes place for the channel with D^{**} resonance production. The phase space factor to be used in the signal density function is:

$$d\Phi = \frac{\mathbf{p}_\omega \mathbf{p}_{D^*}}{\sqrt{m_{\omega\pi}^2}} dm_{\omega\pi}^2 d \cos \xi d \cos \theta d\phi d \cos \beta d\psi, \quad (1)$$

where \mathbf{p}_ω and \mathbf{p}_{D^*} are momenta of ω and D^* , respectively, in the rest frame of the parent particle.

We parameterize a matrix element as a coherent sum of quasi-two-body amplitudes. Each resonant amplitude is parameterized using the basis of covariant amplitudes, which describe the decay with fixed angular orbital momenta in the B and resonance rest frames. All resonant amplitudes are expressed via a set of selected kinematic variables. In Table 2 we show intermediate states, which are included in our model.

3 Event selection

The analysis is performed using the Belle detector ⁵). A data sample of 711 fb⁻¹ (771 million B -pairs) collected at the $\Upsilon(4S)$ resonance is used in our analysis. In analysis D^0 candidates are reconstructed via the $K^-\pi^+$ mode.

For charged tracks we require the origin to be within $|\Delta r| < 0.2$ cm ¹ of the interaction point (IP) in the radial direction, and $|\Delta z| < 1$ cm in the z -direction. (For slow tracks we require $|\Delta r| < 0.3$ cm and $|\Delta z| < 1.5$ cm). The

¹All the parameters mentioned below are given in the laboratory frame.

$\omega\pi$ -states	D^{*} -states
$J^P = 0^-$	$J_{j_u}^P = 1_{1/2}^+ (D_1^0)$
$J^P = 1^- (\rho(1450)^-)$	$J_{j_u}^P = 1_{3/2}^+ (D_1^{\prime 0})$
$J^P = 1^+ (b_1(1235)^-)$	$J_{j_u}^P = 2_{3/2}^+ (D_2^0)$
$J^P = 2^-$	$J_{j_u}^P = 1_{3/2}^-$
$J^P = 2^+$	$J_{j_u}^P = 2_{3/2}^-$
$J^P = 3^- (\rho_3(1690)^-)$	$J_{j_u}^P = 2_{5/2}^-$
	$J_{j_u}^P = 3_{5/2}^-$

Table 2. *Resonant intermediate states to be included in the discussed signal model.*

cut on the transverse momentum of the charged particle (except for slow pion) is $p^\perp > 100 \text{ MeV}/c^2$; for slow pion this cut is $p^\perp > 50 \text{ MeV}/c^2$.

In this analysis, a particle is considered as a kaon, if the likelihood ratio $PID(K/\pi) = L_K/(L_K + L_\pi) > 0.6$, which is about 90% efficient for kaons with (5 – 10)% of the misidentification rate for pions. To identify pions we do not require any cut.

To reduce combinatorial background we apply additional cuts. We require an energy of each photon $E_{\gamma_1}, E_{\gamma_2} > 70 \text{ MeV}$ and the total energy $E_{\gamma_1} + E_{\gamma_2} > 250 \text{ MeV}$.

Neutral pion candidates are formed from the photon pairs that have an invariant mass in the range $123.75 \text{ MeV}/c^2 < m_{\pi^0} < 146.25 \text{ MeV}/c^2$. We select ω candidates with the invariant mass in the range $761.35 \text{ MeV}/c^2 < m_\omega < 803.85 \text{ MeV}/c^2$. To reconstruct $D^0 \rightarrow K^-\pi^+$ candidates, we require their measured invariant mass to be within $1849.5 \text{ MeV}/c^2 < m_{D^0} < 1879.5 \text{ MeV}/c^2$. The D^* candidates are selected by requiring the mass difference $\Delta m = M_{D^{*+}} - M_{D^0}$ to lie within $2 \text{ MeV}/c^2$ of the world average Δm mass $145.5 \text{ MeV}/c^2$.

B -meson candidate events are identified by their C.M. energy difference $\Delta E = E_B^{CM} - E_{beam}^{CM}$, and the beam-constrained mass $m_{bc} = \sqrt{(E_{beam}^{CM})^2 - (P_B^{CM})^2}$, where E_{beam}^{CM} and E_B^{CM} are the C.M. beam energy and reconstructed energy of B -meson candidates and P_B^{CM} is the reconstructed momentum of the B -

meson candidates in the C.M. frame. We require $5.2735 \text{ GeV}/c^2 < m_{bc} < 5.2855 \text{ GeV}/c^2$.

4 Dalitz analysis

We have measured the total branching fraction using the parameterization of the reconstruction efficiency in the Dalitz plot. We have divided the Dalitz plot into cells, measure the efficiency and estimate the partial branching fraction in each cell. The total branching fraction is the sum of all partial branching fractions. However, this method has a large systematic uncertainty due to a finite cell size. Therefore, we can estimate the integrated efficiency relying on the decay model with parameters fixed from the Dalitz analysis.

In our unbinned six-dimensional fit we use various resonant hypotheses in the signal decay model. The non-resonant constant term $\bar{B}^0 \rightarrow D^{*+}\omega\pi^-$, $\bar{B}^0 \rightarrow \rho(770)^-D^{*+}$, $\bar{B}^0 \rightarrow \rho(1450)^-D^{*+}$, $\bar{B}^0 \rightarrow \rho(1700)^-D^{*+}$, $\bar{B}^0 \rightarrow b_1(1235)^-D^{*+}$, $\bar{B}^0 \rightarrow D_1^0(2430)\omega$ and $\bar{B}^0 \rightarrow D_1^0(2420)\omega$ contributions are taken into account.

All resonances are described by relativistic Breit-Wigner functions with energy-dependent widths and the following decay modes:

$$\begin{aligned}
 \rho(770) &\rightarrow \pi\pi + (\rho\omega\pi) \text{ interaction}; \quad \rho(1450) \rightarrow 1/2\pi\pi + 1/2\omega\pi; \\
 \rho(1700) &\rightarrow \omega\pi; \quad b_1(1235) \rightarrow \omega\pi; \\
 D_1(2420) &\rightarrow D^*\pi; \quad D_1(2430) \rightarrow D^*\pi.
 \end{aligned} \tag{2}$$

The fit yields various contributions: the $\rho(770)$ tail is dominant, the $D_1(2420)$ (narrow) and $D_1(2430)$ (broad) as well as $\rho(1450)$ are significant, the non-resonant constant term is also significant and improves the fit quality and the $\rho(1700)$ and $b_1(1235)$ are not significant.

In Fig. 2 we show as an illustration the distributions for the $D^*\pi$ and $\omega\pi$ mass spectra in the pure D^{**} and ρ regions, respectively.

5 Conclusions

In our study we have described a model of the $\bar{B}^0 \rightarrow D^{*+}\omega\pi^-$ decay as a sum of different intermediate states. We study the discussed mode using Belle experimental data. At this moment, we have performed the procedure of the signal reconstruction and estimation of the total branching fraction. We have also performed the Dalitz analysis.

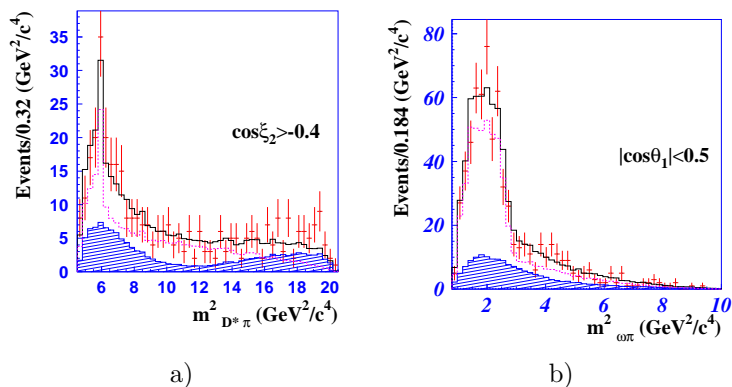


Figure 2. a) $m_{D^*\pi}^2$ and b) $m_{\omega\pi}^2$ distributions in the pure D^{**} and ρ regions, respectively. Data (points), the total fit (black histogram), background (hatched histogram) and signal component (dotted histogram) are shown.

6 Acknowledgements

I thank my scientific advisors S. Eidelman and A. Kuzmin for numerous useful discussions. I thank the KEKB group for the excellent operation of the accelerator.

References

- 1 . Particle Data Group, K. Nakamura *et al.*, J. Phys. G **37**, 075021 (2010).
- 2 . J. P. Alexander *et al.* [CLEO Collaboration], Phys. Rev. D **64** , 092001 (2001).
- 3 . B. Aubert *et al.* [BABAR Collaboration], Phys. Rev. D **74** , 012001 (2006).
- 4 . D. Matvienko, A. Kuzmin and S. Eidelman, JHEP **1109**, 129 (2011).
- 5 . A. Abashian *et al.* [Belle Collaboration], Nucl. Instr. and Meth. A **479** , 117 (2002).

ATLAS SEARCHES FOR SUPERSYMMETRY AT LHC

Federico Meloni
Università degli Studi di Milano & INFN Milano

Abstract

Supersymmetry with large mixing angle predicts that the lightest superpartners of the Standard Model fermions belong to the third generation. Furthermore, naturalness arguments favor masses not too far from the top quark mass. This document presents the status of the searches for supersymmetric particles with the ATLAS detector at LHC, in proton proton collisions at $\sqrt{s} = 7$ TeV. It has been possible to put stringent limits on many supersymmetric particle masses and extend the search for scalar partners of the third generation, both in direct and gluino mediated production.

1 Introduction

Supersymmetry (SUSY) provides an extension of the Standard Model (SM) by introducing supersymmetric partners of the known bosons and fermions. In

the framework of an R-parity conserving minimal supersymmetric extension of the SM (MSSM), SUSY particles are produced in pairs and the lightest supersymmetric particle (LSP), in many models the lightest neutralino χ_1^0 , is stable and a possible candidate for dark matter. An important motivation for SUSY third generation searches is the fact that SUSY can naturally resolve the hierarchy problem, by preventing a large fine-tuning in the Higgs sector, provided that the superpartners of the top quark have relatively low masses.

Furthermore, in the MSSM the scalar partners of right-handed and left-handed fermions, can mix to form two mass eigenstates. This mixing is proportional to the corresponding SM fermion masses and is therefore more important for the third generation. Large mixing can yield sbottom and stop mass eigenstates which are significantly lighter than other sparticles. Consequently, they could be produced with large cross sections at the LHC.

In this document, several ATLAS searches for first two and third generation supersymmetry are reported, using 4.7 fb^{-1} (unless otherwise specified) of LHC proton proton collision data at $\sqrt{s} = 7 \text{ TeV}$.

2 Search for first and second generation squarks and gluinos

The most sensitive search for the first two generations squarks and gluinos selects fully hadronic events with significant missing transverse momentum ($E_{\text{T}}^{\text{miss}} > 1$). The effective mass m_{eff} (defined as the sum of $E_{\text{T}}^{\text{miss}}$ and the p_{T} of all jets) is chosen as discriminant variable because of the high mass scale expected for the SUSY signal. In total, 11 signal regions with various jet multiplicities (ranging from 2 to 6) and different cuts on m_{eff} have been defined, in order to achieve maximal coverage in the squark-gluino mass plane, while enhancing the sensitivity to models with small mass splittings. No evidence is found for physics beyond the SM and the results are hence interpreted in the context of a MSUGRA/CMSSM and a simplified MSSM scenario. This simplified model considers only strong production of gluinos and first and second generation squarks with direct decays to jets and massless neutralinos: gluino masses below 940 GeV, and squark masses below 1380 GeV (for gluino masses up to 2 TeV) are excluded at the 95% confidence level (Fig. 1).

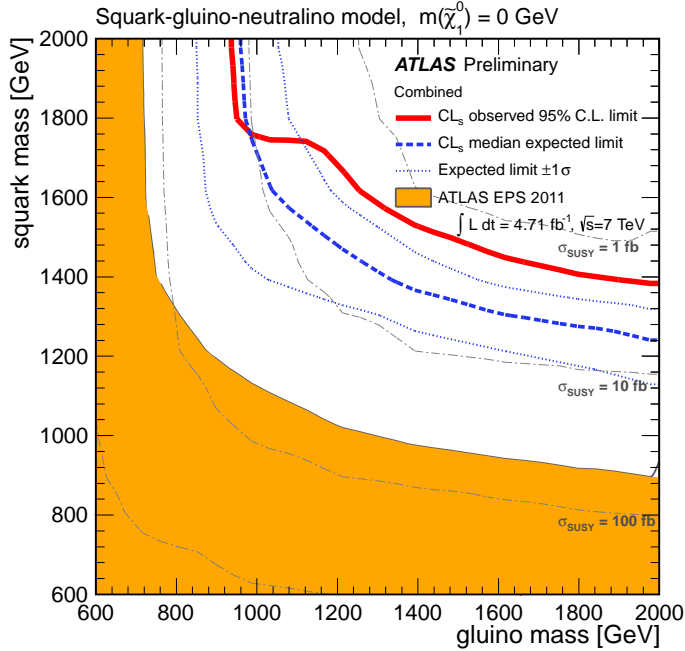


Figure 1: $95\% CL_s$ exclusion limits obtained by using the signal region with the best expected sensitivity at each point in a simplified MSSM scenario. The red line shows the observed limit, the dashed-blue line the median expected limit, and the dotted blue lines the ± 1 sigma variation on the expected limit.

3 Third generation squark searches

Third generation squarks searches have been designed taking into account the possible mass spectra of the involved particles: if the gluino is sufficiently light, pair production of gluinos decaying into bottom and top quarks via on-shell or off-shell sbottoms and stops is possible. A large number of b-tagged jets, large E_T^{miss} and possibly leptons (coming from top quark's leptonic decays) are expected in the final state. Whereas if the gluino is too heavy, the only remaining production process is the direct production of a pair of sbottoms or stops. The former case leads possibly to a final state with exactly two bottom quarks and large E_T^{miss} . The latter case is more complicated to constrain due to

its similarity with top quark pair production and the large number of possible decay processes.

3.1 Search for gluino mediated stop production

Two analyses targeting gluino mediated stop pair production have been performed selecting events with two isolated leptons (e, μ) or events with large jet multiplicity. The two leptons analysis ²⁾ (using 2.05 fb^{-1} of data) assumes that $\tilde{t} \rightarrow t\tilde{\chi}_1^0$ or $\tilde{t} \rightarrow b\tilde{\chi}_1^\pm$, where $\tilde{\chi}_1^\pm$ is the chargino. Two leptons with the same charge (the gluino being a Majorana particle), at least four jets with $p_T > 50 \text{ GeV}$ and $E_T^{miss} > 150 \text{ GeV}$ are required. Two signal regions are defined applying or not a cut on the transverse mass $m_T > 100 \text{ GeV}$. Exclusion limits are derived at 95% CL: $m_{\tilde{g}} < 660 \text{ GeV}$ are excluded for $m_{\tilde{t}} < 460 \text{ GeV}$ (Fig.2).

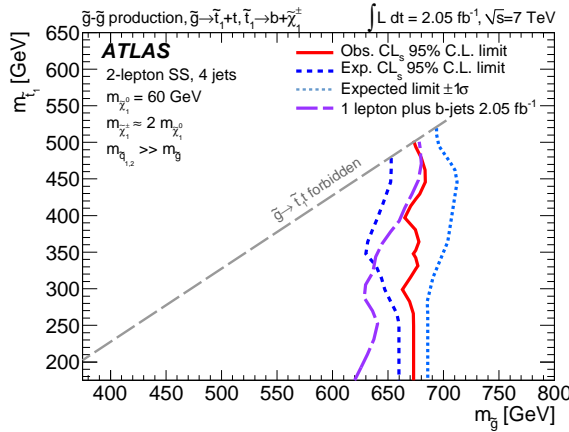


Figure 2: *Expected and observed 95% CL exclusion limits in the $\tilde{g} \rightarrow \tilde{t}_1 t$ with $\tilde{t}_1 \rightarrow b\tilde{\chi}_1^\pm$ model as a function of the gluino and stop masses assuming that $m_{\tilde{\chi}_1^\pm} \approx 2m_{\tilde{\chi}_1^0}$. The -1σ band lies outside the range of the figure.*

Off-shell stop production has been studied ³⁾ searching for events with large jet multiplicities (6-9 jets) and E_T^{miss} . In particular, to suppress the multi jets background, the events are required to have $E_T^{miss}/\sqrt{H_T} > 4 \text{ GeV}^{1/2}$, where H_T is the scalar sum of the transverse momenta of all jets. No excess is

found and depending on the model, $m_{\tilde{g}}$ up to 880 GeV can be excluded.

3.2 Search for gauge-mediated Supersymmetry breaking stop production

A search for direct stop pair production has been carried out on 2.05 fb⁻¹ of data⁴), assuming a gauge-mediated Supersymmetry breaking (GMSB) model where the $\tilde{\chi}_1^0$ decays either via $h\tilde{G}$ or $Z\tilde{G}$ and is lighter than the \tilde{t} , where \tilde{G} is the gravitino (LSP). Events with two same flavour opposite-sign leptons (e, μ) with invariant mass consistent with the Z boson mass, large E_T^{miss} and at least two jets with $p_T > 60(50)$ GeV in the final state are selected. At least one of the jets is required to be originating from a b-quark. The results are interpreted in the framework of R-parity conserving, GMSB scenarios where the $\tilde{\chi}_1^0$ is the next-to-lightest supersymmetric particle. Scalar top quark masses up to 310 GeV are excluded for $115 \text{ GeV} < m_{\tilde{\chi}_1^0} < 230 \text{ GeV}$ at 95% confidence-level, reaching an exclusion of $m_{\tilde{t}} < 330 \text{ GeV}$ for $m_{\tilde{\chi}_1^0} = 190 \text{ GeV}$.

3.3 Search for direct sbottom production

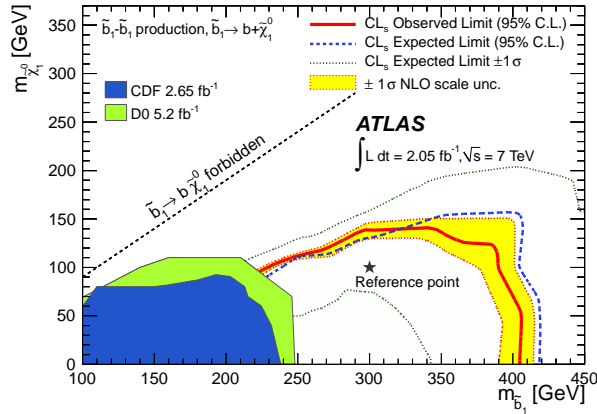


Figure 3: *Expected and observed exclusion limits, as well as ± 1 sigma variation on the expected limit, in the sbottom-neutralino mass plane. The band around the observed limit delimited by the two dashed lines shows the effect of renormalization and factorization scale variation. Results are compared to previous exclusion limits from Tevatron experiments.*

A search for direct sbottom pair production has been performed assuming sbottom decaying into a bottom quark plus a neutralino (LSP) with a branching ratio of 100% using 2.05 fb^{-1} of data⁵⁾. Selected events are required to have exactly two b-tagged jets with $p_T > 130, 50 \text{ GeV}$ and $E_T^{miss} > 130 \text{ GeV}$. Electrons (muons) with $p_T > 20 \text{ GeV}$ (10 GeV) are vetoed, and events are rejected if a third jet with $p_T > 50 \text{ GeV}$ is found. The cuts on the leading jet and the E_T^{miss} are driven by the trigger thresholds. The kinematic variable used to further discriminate the signal from the background is the boosted-corrected contranverse mass m_{CT} , defined as $([E_T(v_1) + E_T(v_2)]^2 - [p_T(v_1) - p_T(v_2)]^2)^{1/2}$ where v_1 and v_2 are the visible products of each decay chain. Three signal regions are defined with $m_{CT} > 100, 150$ and 200 GeV to maximize the sensitivity for different mass splitting between the sbottom and the neutralino. In the most conservative hypothesis, sbottom masses up to 390 GeV are excluded for neutralino masses below 60 GeV (Fig.3).

4 Conclusions

ATLAS has carried out several searches for superpartners of third generation fermions. No excess in data with respect to the SM expectation has been observed so far. However, large regions of the parameter space for natural SUSY are still not excluded and new data with increased centre-of-mass energies together with the study of new channels will bring new opportunities for the discovery of a potential excess.

References

1. ATLAS Collaboration, ATLAS-CONF-2012-033, <http://cdsweb.cern.ch/record/1432199>
2. ATLAS Collaboration, arXiv:1203.5763 [hep-ex]
3. ATLAS Collaboration, ATLAS-CONF-2012-037, <http://cdsweb.cern.ch/record/1432204>
4. ATLAS Collaboration, ATLAS-CONF-2012-036, <http://cdsweb.cern.ch/record/1432203>
5. ATLAS Collaboration, Phys. Rev. Lett. **108**, 181802 (2012).

Frascati Physics Series
3rd YOUNG RESEARCHERS WORKSHOP: “Physics Challenges in the LHC Era”
Frascati, May 7 and 10, 2012

The jet vertex for Mueller-Navelet and forward jet production*

*Talk presented by Beatrice Murdaca.

Francesco Caporale^a, Dmitry Yu. Ivanov^b, Beatrice Murdaca^a,
Alessandro Papa^a, Amedeo Perri^a

^a*Università della Calabria and INFN, Gruppo collegato di Cosenza, Italy*

^b*Sobolev Institute of Mathematics and Novosibirsk State University, Russia*

Abstract

We calculate in next-to-leading order BFKL the jet vertex relevant for the production of Mueller-Navelet jets in proton collisions and of forward jets in deep inelastic scattering. Starting from the definition of the totally inclusive quark and gluon impact factors in the BFKL approach and suitably considering the parton densities and the jet selection functions, we show that an infrared-free result can be found for the jet vertex. Finally we compare our expression for the vertex with the previous calculation of Refs. ¹⁾.

1 Introduction

The Mueller-Navelet jet production process ²⁾ was suggested as an ideal tool to study the Regge limit of perturbative Quantum Chromodynamics (QCD)

in proton-proton (or proton-antiproton) collisions. The process under consideration is

$$p(p_1) + p(p_2) \rightarrow J_1(k_{J,1}) + J_2(k_{J,2}) + X, \quad (1)$$

where two hard jets J_1 and J_2 are produced. Their transverse momenta are much larger than the QCD scale, $\vec{k}_{J,1}^2 \sim \vec{k}_{J,2}^2 \gg \Lambda_{\text{QCD}}^2$, so that we can use perturbative QCD. Moreover, they are separated by a large interval of rapidity, $\Delta y \gg 1$, which means large center of mass energy \sqrt{s} of the proton collisions, $s = 2p_1 \cdot p_2 \gg \vec{k}_{J,1,2}^2$, since $\Delta y \sim \ln s / \vec{k}_{J,1,2}^2$. Since large logarithms of the energy compensate the small QCD coupling, they must be resummed to all orders of perturbative theory.

The BFKL approach ³⁾ is the most suitable framework for the theoretical description of the high-energy limit of hard or semi-hard processes. It provides indeed a systematic way to perform the resummation of the energy logarithms, both in the leading logarithmic approximation (LLA), which means resummation of all terms $(\alpha_s \ln(s))^n$, and in the next-to-leading logarithmic approximation (NLA), which means resummation of all terms $\alpha_s (\alpha_s \ln(s))^n$.

In QCD collinear factorization the cross section of the process reads

$$\frac{d\sigma}{dJ_1 dJ_2} = \sum_{i,j=q,\bar{q},g} \int_0^1 \int_0^1 dx_1 dx_2 f_i(x_1, \mu) f_j(x_2, \mu) \frac{d\hat{\sigma}_{i,j}(x_1 x_2 s, \mu)}{dJ_1 dJ_2}, \quad (2)$$

with $dJ_{1,2} = dx_{J_{1,2}} d^{D-2} k_{J_{1,2}}$ and the i, j indices specify parton types (quarks q , antiquarks \bar{q} or gluon g); $f_i(x, \mu)$ denotes the initial proton parton density function (PDF), the longitudinal fractions of the partons involved in the hard subprocess are $x_{1,2}$, μ is the factorization scale and $d\hat{\sigma}_{i,j}(x_1 x_2 s, \mu)$ is the partonic cross section for the production of jets, $\hat{s} = x_1 x_2 s$ being the energy of the parton-parton collision. In the BFKL approach the resummed cross section of the hard subprocess is represented as the convolution of the jet impact factors of the colliding particles with the Green's function G_ω , process-independent and determined through the BFKL equation,

$$\begin{aligned} \frac{d\hat{\sigma}}{dJ_1 dJ_2} &= \frac{1}{(2\pi)^{D-2}} \int \frac{d^{D-2} \vec{q}_1}{\vec{q}_1^2} \frac{d\Phi_{J,1}(\vec{q}_1, s_0)}{dJ_1} \int \frac{d^{D-2} \vec{q}_2}{\vec{q}_2^2} \frac{d\Phi_{J,2}(-\vec{q}_2, s_0)}{dJ_2} \\ &\times \int_{\delta-i\infty}^{\delta+i\infty} \frac{d\omega}{2\pi i} \left(\frac{\hat{s}}{s_0} \right)^\omega G_\omega(\vec{q}_1, \vec{q}_2). \end{aligned} \quad (3)$$

The aim of this work is to illustrate the calculation of the NLA jet vertex.

Since jets are originated by the hadronization of produced partons, the starting point is the impact factors for colliding partons ^{4, 5, 6, 7}. In order to select the partons that will generate the jet, we “open” one of the integrations over the partonic phase space and introduce a suitably defined jet selection function S_J . For the LLA impact factor, where there can be only a one-particle intermediate state, the jet function identifies the jet momentum with the momentum of the one parton ($S_J^{(2)}$). For the NLA impact factor we can have only either a one-particle (virtual corrections) or two-particle intermediate states. In the last case the S_J function identifies the jet momentum with the momentum of one of the two partons or with the sum of the momenta of two partons ($S_J^{(3)}$).

In the calculation of the jet vertex, infrared divergences related with soft emission will cancel in the sum with virtual corrections. The remaining infrared divergences are taken care of by the PDFs’ renormalization. The collinear counterterms appear due to the replacement of the bare PDFs by the renormalized physical quantities obeying DGLAP evolution equations (in the $\overline{\text{MS}}$ factorization scheme). Ultraviolet divergences are removed by the counterterm related with QCD charge renormalization (in the $\overline{\text{MS}}$ scheme).

Starting from the known lowest-order parton impact factors ^{4, 5}, corresponding to the totally inclusive process, we get the LLA jet impact factor by suitably introducing the $S_J^{(2)}$ function

$$\frac{d\Phi_J^{(0)}(\vec{q})}{dJ} = \Phi_q^{(0)} \int_0^1 dx \left(\frac{C_A}{C_F} f_g(x) + \sum_{a=q,\bar{q}} f_a(x) \right) S_J^{(2)}(\vec{q}; x), \quad (4)$$

where $\Phi_q^{(0)} = g^2 \frac{\sqrt{N_c^2 - 1}}{2N_c}$ is the quark impact factor (defined as the imaginary part of the quark-Reggeon diffusion process) at the Born level and \vec{q} is the Reggeon momentum.

Substituting here the bare QCD coupling and bare PDFs by the renormalized ones, we obtain the following expressions for the counterterms:

$$\begin{aligned} \frac{d\Phi_J(\vec{q})|_{\text{charge c.t.}}}{dJ} &= \frac{\alpha_s}{2\pi} \left(\frac{1}{\hat{\varepsilon}} + \ln \frac{\mu_R^2}{\mu^2} \right) \left(\frac{11C_A}{6} - \frac{N_F}{3} \right) \Phi_q^{(0)} \\ &\times \int_0^1 dx \left(\frac{C_A}{C_F} f_g(x) + \sum_{a=q,\bar{q}} f_a(x) \right) S_J^{(2)}(\vec{q}; x) \end{aligned} \quad (5)$$

for the charge renormalization, and

$$\begin{aligned} \frac{d\Phi_J(\vec{q})|_{\text{collinear c.t.}}}{dJ} &= -\frac{\alpha_s}{2\pi} \left(\frac{1}{\hat{\varepsilon}} + \ln \frac{\mu_F^2}{\mu^2} \right) \Phi_q^{(0)} \int_0^1 d\beta \int_0^1 dx S_J^{(2)}(\vec{q}; \beta x) \quad (6) \\ &\times \left[\sum_{a=q, \bar{q}} (P_{qq}(\beta) f_a(x) + P_{qg}(\beta) f_g(x)) \right. \\ &\left. + \frac{C_A}{C_F} \left(P_{gg}(\beta) f_g(x) + P_{gq}(\beta) \sum_{a=q, \bar{q}} f_a(x) \right) \right], \end{aligned}$$

for the collinear counterterm.

Now we have all the necessary ingredients to perform our calculation of the NLA corrections to the jet impact factor.

We will consider separately the subprocesses initiated by the quark and the gluon PDFs and denote

$$V = V_q + V_g \quad \text{with} \quad \frac{d\Phi_J^{(1)}(\vec{q})}{dJ} \equiv \frac{\alpha_s}{2\pi} \Phi_q^{(0)} V(\vec{q}). \quad (7)$$

2 NLA jet impact factor

2.1 The quark contribution

Virtual corrections are the same as in the case of the inclusive quark impact factor (4, 5, 6):

$$\begin{aligned} V_q^{(V)}(\vec{q}) &= -\frac{\Gamma[1-\varepsilon] \Gamma^2(1+\varepsilon)}{\varepsilon (4\pi)^\varepsilon \Gamma(1+2\varepsilon)} \int_0^1 dx \sum_{a=q, \bar{q}} f_a(x) S_J^{(2)}(\vec{q}; x) \quad (8) \\ &\times \left[C_F \left(\frac{2}{\varepsilon} - 3 \right) - \frac{N_F}{3} + C_A \left(\ln \frac{s_0}{\vec{q}^2} + \frac{11}{6} \right) \right] + \text{finite terms}. \end{aligned}$$

For the incoming quark case, real corrections originate from the quark-gluon intermediate state. We denote the momentum of the gluon by k , then the momentum of the quark is $q - k$; the longitudinal fraction of the gluon momentum is denoted by βx . Thus, the real contribution has the form

$$V_q^{(R)}(\vec{q}) = \int_0^1 dx \sum_{a=q, \bar{q}} f_a(x) \left\{ \frac{\Gamma[1-\varepsilon] \Gamma^2(1+\varepsilon)}{\varepsilon (4\pi)^\varepsilon \Gamma(1+2\varepsilon)} \left[C_F \left(\frac{2}{\varepsilon} - 3 \right) S_J^{(2)}(\vec{q}; x) \right. \right.$$

$$\begin{aligned}
& + \int_0^1 d\beta \left(P_{qq}(\beta) + \frac{C_A}{C_F} P_{gq}(\beta) \right) S_J^{(2)}(\vec{q}; x\beta) \Big] + \frac{C_A}{(4\pi)^\varepsilon} \int \frac{d^{D-2}\vec{k}}{\pi^{1+\varepsilon}} \\
& \times \frac{\vec{q}^2}{\vec{k}^2 (\vec{q} - \vec{k})^2} \ln \frac{s_0}{(|\vec{k}| + |\vec{q} - \vec{k}|)^2} S_J^{(2)}(\vec{q} - \vec{k}; x) \Big\} + \text{finite terms} .
\end{aligned} \tag{9}$$

2.2 The gluon contribution

Virtual corrections are the same as in the case of the inclusive gluon impact factor ^{4, 6}):

$$\begin{aligned}
V_g^{(V)}(\vec{q}) &= -\frac{\Gamma[1-\varepsilon] \Gamma^2(1+\varepsilon)}{\varepsilon (4\pi)^\varepsilon \Gamma(1+2\varepsilon)} \int_0^1 dx \frac{C_A}{C_F} f_g(x) S_J^{(2)}(\vec{q}; x) \\
&\times \left[C_A \ln \left(\frac{s_0}{\vec{q}^2} \right) + C_A \left(\frac{2}{\varepsilon} - \frac{11}{6} \right) + \frac{N_F}{3} \right] + \text{finite terms} .
\end{aligned} \tag{10}$$

In the NLA gluon impact factor real corrections come from intermediate states of two particles, which can be quark-antiquark or gluon-gluon ^{4, 6, 7}).

We find

$$\begin{aligned}
V_g^{(R)}(\vec{q}) &= \frac{\Gamma[1-\varepsilon] \Gamma^2(1+\varepsilon)}{\varepsilon (4\pi)^\varepsilon \Gamma(1+2\varepsilon)} \int_0^1 dx f_g(x) \left\{ \frac{C_A}{C_F} \left(\frac{N_F}{3} + \frac{2C_A}{\varepsilon} - \frac{11}{6} C_A \right) \right. \\
&\times S_J^{(2)}(\vec{q}; x) + \int_0^1 d\beta \left[2N_F P_{qg}(\beta) + 2C_A \frac{C_A}{C_F} \left(P(\beta) + \frac{(1-\beta)P(1-\beta)}{(1-\beta)_+} \right) \right] \\
&\times S_J^{(2)}(\vec{q}; x\beta) \Big\} + \frac{C_A}{(4\pi)^\varepsilon} \int_0^1 dx \frac{C_A}{C_F} f_g(x) \int \frac{d^{D-2}\vec{k}}{\pi^{1+\varepsilon}} \frac{\vec{q}^2}{\vec{k}^2 (\vec{k} - \vec{q})^2} \ln \frac{s_0}{(|\vec{k}| + |\vec{q} - \vec{k}|)^2} \\
&\times S_J^{(2)}(\vec{q} - \vec{k}; x) + \text{finite terms} .
\end{aligned} \tag{11}$$

To conclude, we collect the contributions given in Eqs. (5), (6), (8), (9), (10), (11), and we note that we are left with two divergences: the last of (9) and of (11). It is easy to see that the integration of those terms over \vec{q} with any function, regular at $\vec{q} = \vec{k}_J$, will give a divergence-free result. In particular, a finite result will be obtained after the convolution of the jet vertex with BFKL Green's function, which is required for the calculation of the jet cross section.

Note that divergent terms of the two parton intermediate state contributions, shown in Eqs. (9) and (11), are expressed through the jet function $S_J^{(2)}$, due to reduction of $S_J^{(3)} \rightarrow S_J^{(2)}$ in the kinematic regions of soft or collinear parton radiation.

More details about this calculation can be found in Ref. ⁸).

3 Summary

We have recalculated the jet vertices for the cases of quark and gluon in the initial state, first found by Bartels *et al.* ¹⁾. Our approach is different, since the starting point of our calculation is the known general expression for next-to-leading-order impact factors, given in Ref. ⁹⁾, applied to the special case of partons in the initial state. Nevertheless, in many technical steps we followed closely the derivation of Refs. ¹⁾.

In our approach the energy scale s_0 remains untouched and need not be fixed at any definite value. In order to compare our results with those of ¹⁾, we need to perform the transition (see ¹⁰⁾) from the standard BFKL scheme with arbitrary energy scale s_0 to the one used in ¹⁾, where the energy scale depends on the Reggeon momentum. After this procedure, we can see a complete agreement with ¹⁾.

The jet vertex discussed in this paper is an essential ingredient also for the study of the inclusive forward jet production in deep inelastic scattering in the NLA.

References

1. J. Bartels, *et al.*, Eur. Phys. J. C **24**, 83 (2002); C **29**, 235 (2003).
2. A.H. Mueller, *et al.*, Nucl. Phys. B **282**, 727 (1987).
3. V.S. Fadin, *et al.*, Phys. Lett. B **60**, 50 (1975); E.A. Kuraev, *et al.*, Zh. Eksp. Teor. Fiz. **71**, 840 (1976); Ya.Ya. Balitskii, *et al.*, Sov. J. Nucl. Phys. **28**, 822 (1978).
4. V.S. Fadin, *et al.*, Phys. Lett. **D61**, 094005 (2000).
5. V.S. Fadin, *et al.*, Phys. Lett. **D61**, 094006 (2000).
6. M. Ciafaloni, *et al.*, Nucl. Phys. B **538**, 187 (1999).
7. M. Ciafaloni, Phys. Lett. B **429**, 363 (1998).
8. F. Caporale, *et al.*, JHEP **02**, 101 (2012).
9. V.S. Fadin, *et al.*, Phys. Lett. B **440**, 359 (1998).
10. V.S. Fadin, arXiv:hep-ph/9807527.

Frascati Physics Series
3rd YOUNG RESEARCHERS WORKSHOP: “Physics Challenges in the LHC Era”
Frascati, May 7 and 10, 2012

Measurement of the Cosmic Rays primary spectrum with ARGO-YBJ experiment

Beatrice Panico for the ARGO-YBJ Collaboration
Università Roma Tor Vergata - INFN Roma Tor Vergata
Via Della Ricerca Scientifica, 1, 80133 Roma

Abstract

The study of cosmic rays physic of 10^{12} - 10^{15} primary cosmic energy is one of the main goals of ARGO-YBJ experiment. The detector, located at the Yangbajing Cosmic Ray Laboratory (Tibet, 4300 m a.s.l., 606 g/cm²), is an EAS array consisting of a continuous carpet of RPCs. The low energy threshold of the detector allows to study an energy region characterized by the transition from the direct to the indirect measurements. In this paper we will report on the measurement of the cosmic rays energy spectrum at different zenith angles. The phenomenology of horizontal air shower ($> 70^\circ$) will be described and discussed.

1 The ARGO-YBJ experiment

The detector is composed of a central carpet large $\sim 74 \times 78$ m², made of a single layer of Resistive Plate Chambers (RPCs) with $\sim 93\%$ of active area, enclosed

by a guard ring partially ($\sim 20\%$) instrumented up to $\sim 100 \times 110 \text{ m}^2$. The basic data acquisition element is a cluster ($5.7 \times 7.6 \text{ m}^2$), made of 12 RPCs ($2.8 \times 1.25 \text{ m}^2$ each). Each chamber is read by 80 external strips of dimension $6.75 \times 61.8 \text{ cm}^2$ (the spatial pixels), logically organized in 10 independent pads of area $55.6 \times 61.8 \text{ cm}^2$ which represent the time pixels of the detector ¹⁾. The whole system is in stable data taking with the full apparatus since Nov.2007 with a duty cycle $\geq 85\%$. The reconstruction algorithms and the detector performance are described in Bartoli et al. ²⁾.

2 Measurement of the size spectrum

The measured event rate can be modulated on a long time period by the instrumental response and by the atmospheric effects. In order to minimize the first effect, a sample of high quality runs has been selected by requiring that the total number of pads with a counting rate less than 50% of the mean value is less than 3%. The atmospheric effects are responsible of the so called “barometric effect”: owing to the mass absorption provided by the Earth’s atmosphere, variations of the atmospheric pressure result in small fluctuations of the cosmic ray flux. The percentage variation in the cosmic ray intensity caused by a pressure change of 1 mbar is expressed by the use of the barometric coefficient β ($\approx 0.7\%$). We excluded from the analysis all data with a pressure value larger than 3 standard deviations from the mean value. These selections leads to a data set of about 250 days in 2009. A different approach, using Bayesian unfolding procedure, has been used by the ARGO-YBJ collaboration to calculate the light component energy spectrum below 100 TeV in B.Bartoli ³⁾.

2.1 Data analysis

The following analysis refers to events with reconstructed zenith angle of the shower less than 15° and reconstructed shower core position inside a fiducial area $A_{fid}=40 \times 40 \text{ m}^2$ centered on the detector.

In order to correct the fluctuations of the cosmic ray flux, the correlation with atmospheric pressure and temperature has been investigated. We found, as expected, the barometric effect dominant. The rates are normalized to the number of operating pads and at the nominal pressure at YBJ site. The selected events have been divided into “differential classes” defined by strip multiplicity

ΔN_s . The width of the fired strip bins corresponds to $\Delta \text{Log}(N_s) = 0.2$. For each bin, the measured rate has been corrected also for the dead time (4%) and for the average pad efficiency (95%).

2.2 Monte Carlo simulation

The air shower development in the atmosphere has been simulated with the CORSIKA v. 6.7.2 code ⁴⁾. Cosmic rays have been generated in the energy range from 100 GeV to 4 PeV according to different spectra given in 5, 6, 7, 8). About $\sim 10^9$ showers induced by protons, helium, CNO, MgSi and Fe nuclei have been sampled in the zenith angle interval $0^\circ - 20^\circ$. The experimental conditions (trigger logic, time resolution, electronic noises, relation between strip and pad multiplicities, etc.) have been taken into account via a GEANT3-based code.

The effective areas $A_{eff}(E, >N_s)$, for events with core inside the fiducial area, are folded with the energy spectrum of each primary nucleus to obtain the expected rate for each primary mass i . The main contribution to the expected rate is provided by proton primaries. The contribution of the other nuclei increases with the strip multiplicity of the event. The relative fractions (in % of the total) $R_P/R_{He}/R_{CNO}/R_{heavy}$ are 67.6/28.2/2.7/0.7 in the first multiplicity bin ($\Delta N_S = 251-398$) and 51.2/40.4/5.4/2.4 in the last multiplicity bin ($\Delta N_S = 6310 - 10000$) for CREAM spectra. Proton- and helium- induced showers contribute to the rate for more than 90% in the whole strip multiplicity range. The CNO contribution is $< 7\%$, heavier nuclei contribute less than 3%.

2.3 Comparison with data

To obtain the light (p+He) component spectrum, we subtracted from the data the contribution of heavy elements, CNO, MgSi and Fe, calculated with CREAM spectra. In Fig. 1 the experimental event rate, without the contribution of heavy nuclei, is shown as a function of the strip multiplicity (stars) and compared to the expectations according to CREAM, Hörandel, JACEE and RUNJOB (p+He) spectra. The rate has been multiplied by $N^{1.25}$.

The median energy for proton- (helium-) induced showers ranges from 4.5 (9) TeV ($\Delta N_S = 251-398$) up to 56 (90) TeV ($\Delta N_S = 6310-10000$). The statistical error on data is negligible, while the systematic uncertainty is estimated

$\pm 10\%$, mainly due to the reconstruction of the core position.

The different lines in Fig.1 are best fits with the following spectral indices: -1.25 ± 0.03 for data (solid line), -1.21 ± 0.03 for Hörandel spectrum (short-dashed line), -1.32 ± 0.03 for RUNJOB spectrum (dot-dashed line), -1.26 ± 0.02 for JACEE spectrum (long-dashed line) and -1.15 ± 0.03 for CREAM spectrum (dotted line). The uncertainties associated to different measurements are not shown in Fig.1, being of the order of 15%.

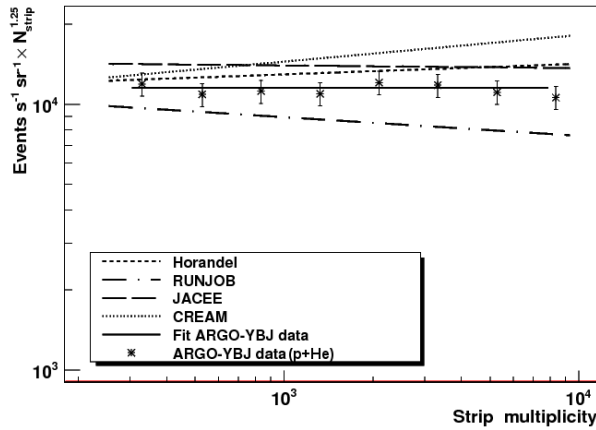


Figure 1: Comparison between the experimental data (stars) and the differential expected rates according to different spectra. The solid line is the best fit to data (see text for details).

3 Horizontal Air Showers (EAS)

Above 60° the exponential attenuation of the CRs rate due to the absorption of the electromagnetic component travelling a large atmospheric depth seems to be violated because new showers are injected due to muon bremsstrahlung. In fact a large number of showers, approximately constant with increasing angle, is observed. The majority of these events are expected to be due to showers produced in hard muon Bremsstrahlung processes ⁹⁾. The observation of EAS

in nearly horizontal directions provides a possible “well shielded laboratory” for the detection of penetrating particles: high energy muons, cosmic neutrinos, possible weakly interacting particles produced in the decays of cosmological superheavy particles. The study of HAS is one of the possible methods of observing the muon flux above 10^{14} eV, that is especially interesting because of its relation both with the primary proton flux and with the production cross section of prompt muons in hadronic interactions.

In Fig.2 typical HAS detected by ARGO-YBJ at large zenith angles ($> 80^\circ$) are shown. The multiplicity spectrum measured as a function of the zenith angle is reported in Fig.3(a). The spectral slopes are nearly constant up to 50° , than steepen with increasing angle in the region $\theta = 50^\circ - 70^\circ$, as can be appreciated in the Fig.3(b), where the evolution of the spectral index as a function of the zenith angle is shown. A transition from typical EAS dominated by electromagnetic component to showers induced by primary muons clearly appears. In fact the size spectrum of secondary muons is one unit less than that of the primary CRs (≈ 3.7). A calculation of the expected size spectrum by muon bremsstrahlung is under way.

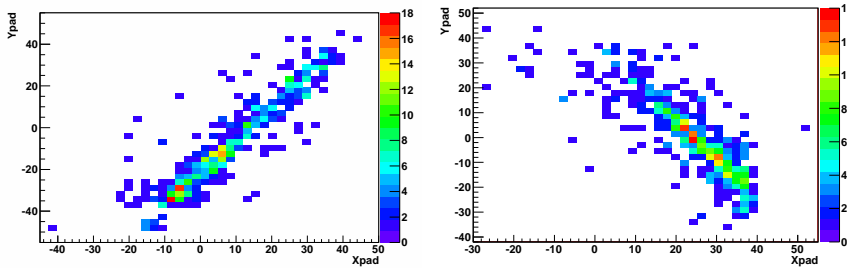


Figure 2: *Events with reconstructed zenith angle $\theta > 80^\circ$*

4 Conclusions

The high segmentation of the ARGO-YBJ read-out detector and its location at high altitude allow the detection and the reconstruction of air showers with unprecedented resolution. Selecting quasi-vertical showers with core located on a fiducial area well inside the ARGO-YBJ central carpet, a sample of events mainly induced by proton and helium primaries with energy < 100 TeV is

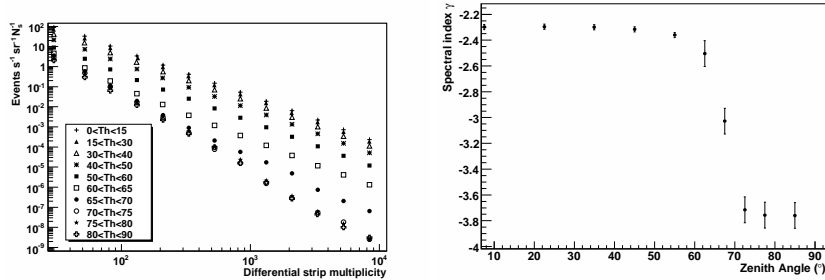


Figure 3: a) *Differential strip spectrum for different bin of incident angle.* b) *Spectral index as a function of the increasing zenith angle.*

obtained. For the first time a ground-based measurement of the CR light component spectrum overlaps data obtained with direct methods for more than one energy decade, thus providing a solid anchorage to the CR primary spectrum measurements in the knee region carried out by EAS arrays. Our results are in good agreement with the CREAM measurements. A preliminary study of HAS is also reported.

References

1. G. Aielli et al., *NIM*, A562, 2006, 92-96.
2. B. Bartoli et al., *Phys. Rev. D*, 84, 2011, 022003.
3. B. Bartoli et al., *Phys. Rev. D*, 85, 2012, 092005.
4. D.Heck et al.,*Report FZKA 6019* (1998).
5. Y. S. Yoon et al., *ApJ* 728, 2011, 122-129.
6. J.H. Hörandel, *Astrop. Phys.* 19, 2003, 193-220.
7. K. Asakimori et al.,*ApJ* 502, 1998, 278-283.
8. A.V. Apanasenko et al., *Astrop. Phys.* 16, 2001, 13-46.
9. G. Parente et al., *Astrop. Phys.*, 3, 1995, 17-28.

DOUBLE PARTON INTERACTIONS IN PROTON DEUTERON COLLISIONS

Simona Salvini
University of Trieste, Strada Costiera 11, Trieste (Italy)

Abstract

MPIs are the tool to obtain information on the correlations between partons in the hadron structure. In the case of pp collisions the effects of correlations in the transverse coordinates and in fractional momenta are in fact unavoidably mixed in the final observables. On the contrary, the contribution to the pA cross section, where the projectile interacts with large momentum exchange with at least two target nucleons simultaneously, has only a weak dependence on the correlations in the transverse coordinates. By studying the simplest case, double parton interactions in pD collisions, one can thus obtain non trivial information on the two-body parton correlations.

1 Proton-Proton Collisions

Double Parton Interactions (DPIs) are the simplest case of Multiple Parton Interactions. In Double-Parton Interactions two high energy subprocesses occur

in a hadronic collision, with two initial partons being active from each incident hadron. Double (or more in general multiple) parton interactions are more relevant when the energy and the luminosity of colliders are large, as in the case of the LHC ²⁾ where, therefore, they are part of the background for the processes of main interest.

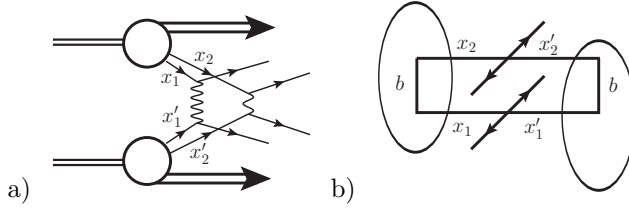


Figure 1: a) *Double parton interaction (or DPI): each incoming hadron offers two partons which undergo in two different interactions.* b) *Geometrical picture of DPI: only partons with the same relative transverse distance can interact.*

The inclusive double-parton interaction for two parton processes A and B in a proton-proton collision (fig. 1,a) is given by ¹⁾

$$\sigma_{double}^{pp(A,B)} = \frac{m}{2} \sum_{i,j,k,l} \int \Gamma_{i,j}(x_1, x_2; b) \hat{\sigma}_{i,k}^A(x_1, x'_1) \hat{\sigma}_{j,l}^B(x_2, x'_2) \Gamma_{k,l}(x'_1, x'_2; b) dx_1 dx'_1 dx_2 dx'_2 db \quad (1)$$

where $m = 1$ (2) for indistinguishable (distinguishable) parton subprocesses. A new non-perturbative input arises, that is the double-parton distribution function $\Gamma_{i,j}(x_1, x_2; b)$, which provides information on the hadron structure not accessible otherwise by means of a single scattering process (fig. 1,b).

Without loss of generality the double parton distribution is written as

$$\Gamma(x_1, x_2; b) = G(x_1, x_2) f_{x_1 x_2}(b), \quad (2)$$

with f_{xy} normalized to 1 and its transverse scale still dependent on the fractional momenta. Moreover

$$G(x_1, x_2) = K(x_1, x_2) G(x_1) G(x_2) \quad (3)$$

$$\int f_{x_1 x_2}(b) f_{x'_1 x'_2}(b) db = \frac{1}{\pi \Lambda^2 (x_1 x'_1 x_2 x'_2)} \quad (4)$$

with G the usual Parton Distribution Functions. K and Λ are related respectively to the longitudinal and transverse correlations¹. In terms of the parametrization 2, eq. 1 becomes

$$\sigma_{double}^{pp(A,B)} = \frac{m}{2} \frac{K(x_1, x_2) K(x'_1, x'_2)}{\pi \Lambda^2(x_1 x'_1 x_2 x'_2)} \sigma_A(x_1, x'_1) \sigma_B(x_2, x'_2) =: \frac{m}{2} \frac{\sigma_A \sigma_B}{\sigma_{eff}}. \quad (5)$$

The last equality relates our phenomenological expression of the cross section to the one exploited in the experimental search. As $\sigma_{A(B)}$ are known, the quantity to evaluate is σ_{eff} . It has been first measured by CDF collaboration at Tevatron⁴). Its value seems to depend weakly on the fractional momenta and has been estimated to be $\sigma_{eff} = 14.5 \pm 1.7_{-2.3}^{+1.7}$. From eq. 5,

$$\sigma_{eff}(x_1 x'_1 x_2 x'_2) = \frac{\pi \Lambda^2(x_1 x'_1 x_2 x'_2)}{K(x_1, x_2) K(x'_1, x'_2)}. \quad (6)$$

The relation 6 shows that σ_{eff} summarizes all information concerning the correlation in the case of DPI in pp scatterings; however, whereas the contribution from different flavours can be disentangled by selecting the final states properly (they add up), the effects of correlations in the transverse coordinates and in the (longitudinal) fractional momenta are unavoidably mixed in the final observables.

2 Proton-Deuteron Collisions

Additional information on multiparton correlations can be obtained by studying DPIs in proton-Deuteron collisions since, as we will show, the longitudinal and transverse correlations have different effects when a single nucleon or both target nucleons participate in the hard process.

In this case the double parton interaction cross section receives three different contributions:

$$\sigma_{double}^{pD} = \sigma_{2,0}^{pD} + \sigma_{1,1;\mathcal{D}}^{pD} + \sigma_{1,1;\mathcal{I}}^{pD}. \quad (7)$$

$\sigma_{2,0}^{pD}$ is the contribution where only a single target nucleon undergoes a double parton collision, while there is no large momentum exchange with the second nucleon. $\sigma_{1,1;\mathcal{D}}^{pD}$ and $\sigma_{1,1;\mathcal{I}}^{pD}$ are respectively the diagonal and the off-diagonal contributions when both target nucleons interact with large momentum.

¹the dependence on the factorization scale is understood everywhere.

2.1 Only a single target nucleon interacting with large momentum exchange

When only a single target nucleon interacts with large momentum exchange, the cross section is

$$\sigma_{2,0}^{pD} = 2 \int \Gamma(x_1, x_2; b) \hat{\sigma}(x_1, x'_1) \hat{\sigma}(x_2, x'_2) \Gamma\left(\frac{x'_1}{Z}, \frac{x'_2}{Z}; b\right) \frac{|\Psi_D(Z, \beta)|^2}{Z(2-Z)} dZ d\beta db \quad (8)$$

where x_1, x_2, x'_1, x'_2, Z are fractional momenta of partons ($x_i^{(i)}$) and nucleons (Z) with respect to the leading light-cone components of the experimentally accessible momenta; b, β are respectively the relative transverse distance between the two interacting partons and the relative transverse distance between the two nucleons. The information on the nuclear structure is carried by Ψ_D , which is given by the non-relativistic Deuteron wave function expressed through light-cone variables. By neglecting the smearing in the longitudinal nuclear fractional momentum Z ,

$$\sigma_{2,0}^{pD} \simeq 2\sigma_{double}^{pp}, \quad (9)$$

thereby this term does not increase our knowledge with respect to the pp collisions. In particular, the transverse scale of the process is the same as in the pp interactions.

2.2 Both target nucleons interacting with large momentum exchange

2.2.1 Diagonal contribution

The diagonal contribution is given by

$$\begin{aligned} \sigma_{1,1;\mathcal{D}}^{pD} &= \int \Gamma(x_1, x_2; b) \hat{\sigma}(x_1, x'_1) \hat{\sigma}(x_2, x'_2) \Gamma\left(\frac{x'_1}{Z}; b_1\right) \Gamma\left(\frac{x'_2}{2-Z}; b_2\right) \\ &\quad \frac{|\Psi_D(Z, \beta)|^2}{Z(2-Z)} \delta(\beta - b_1 + b_2 - b) dZ d\beta db_1 db_2 db. \end{aligned} \quad (10)$$

The leading contribution is obtained by neglecting the hadronic scale with respect to the deuteron radius:

$$\sigma_{1,1;\mathcal{D}}^{pD} \simeq K(x_1, x_2) \sigma_{single}^{pp}(x_1, x'_1) \sigma_{single}^{pp}(x_2, x'_2) |\Psi_D(1, 0)|^2. \quad (11)$$

Therefore this contribution has dimensionality given by the deuteron radius and is independent on the transverse correlations.

2.2.2 Non-diagonal contribution

$$\begin{aligned} \sigma_{1,1;\mathcal{I}}^{pD} &= \int \Gamma(x_1, x_2; b) \hat{\sigma}(x_1, x'_1) \hat{\sigma}(x_2, x'_2) \tilde{H}\left(\frac{x'_1}{Z'}, \frac{x'_2}{Z'}; b_1, b_2 - \beta\right) \\ &\quad \tilde{H}\left(\frac{x'_2}{2-Z'}, \frac{x'_1}{2-Z'}; b_2, b_1 - \beta\right) \frac{\Psi_D(Z, \beta)}{Z} \frac{\Psi_D^*(2-Z', \beta)}{2-Z'} \\ &\quad \delta(\beta + b_2 - b_1 - b) \delta(Z' - Z + x'_1 - x'_2) dZ dZ' d\beta db_1 db_2 db \end{aligned} \quad (12)$$

provides the non-diagonal contribution. Here the nucleons fractional momenta are different in the right and in the left side of the cut (fig. 2,a) but connected by a δ function: $Z - Z' = x'_1 - x'_2$ (with x'_1 and x'_2 measured in the final state). We define an off-diagonal function $\hat{H}(x, y; b) := \int \tilde{H}(x, y; b_1, b_1 - b) db_1$ such that $\hat{H}(x, x; 0) = G(x)$, related to the Generalized Parton Distributions ⁵⁾.

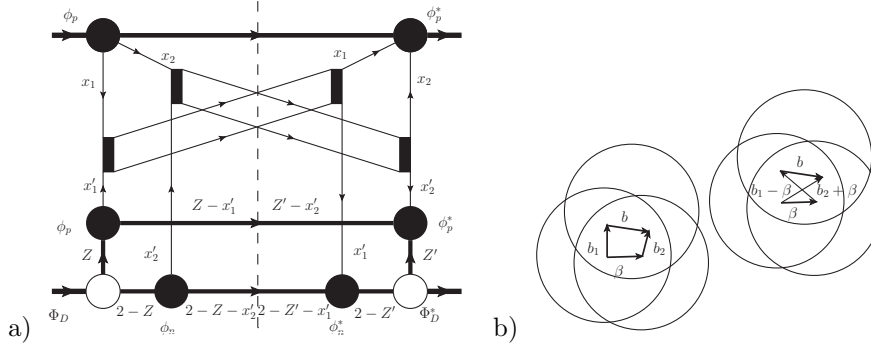


Figure 2: a) Cut diagram relative to the off-diagonal contribution to DPI when both the target nucleons hard interact. b) The two interfering configurations in the transverse space. They give rise to the same initial partonic state.

Again, neglecting the hadronic scale with respect to the deuteron radius leads to the dominant contribution

$$\begin{aligned} \sigma_{1,1;\mathcal{I}}^{pD} &\simeq K(x_1, x_2) G(x_1) G(x_2) \hat{\sigma}(x_1, x'_1) \hat{\sigma}(x_2, x'_2) \int f_{x_1 x_2}(b) \hat{H}\left(\frac{x'_1}{Z'}, \frac{x'_2}{Z'}; b\right) \\ &\quad \hat{H}\left(\frac{x'_2}{2-Z'}, \frac{x'_1}{2-Z'}; b\right) \frac{\Psi_D(Z, 0) \Psi_D^*(2-Z', 0)}{Z(2-Z')} \delta(Z' - Z + x'_1 - x'_2) db dZ dZ'. \end{aligned} \quad (13)$$

Since the Deuteron wave function is evaluated in $\beta = 0$, the cross section is proportional to $1/R_D^2$; so the Deuteron radius still provides the dimensionality of the cross section.

The cross section 13 depends on the correlation in transverse space like 11. However the two contributions can be separated by exploiting the very strong dependence on $x'_1 - x'_2$ of 13, due to the overlap of the Deuteron wave function.

3 Results and conclusions

In first approximation, we consider the leading contributions to the cross section, namely eq. 9, 11 and 13. We find out that

$$\sigma_{double}^{pD} - \sigma_{2,0}^{pD} = \sigma_{1,1;\mathcal{D}}^{pD} + \sigma_{1,1;\mathcal{I}}^{pD} \quad (14)$$

is linear in K . The study of the left side of eq. 14 as a function of $x'_1 - x'_2$ allows to disentangle the contribution of the interference term and obtain reliable indication not only about K , the longitudinal contribution, but also about Λ , the transverse one, through the evaluation of the overlaps

$$\int f_{x_1 x_2}(b) \hat{H}\left(\frac{x'_1}{Z}, \frac{x'_2}{Z'}; b\right) \hat{H}\left(\frac{x'_2}{2-Z}, \frac{x'_1}{2-Z'}; b\right) db$$

$$\int f_{x_1 x_2}(b) f_{x'_1 x'_2}(b) db = \frac{1}{\pi \Lambda^2(x_1, x'_1, x_2, x'_2)}. \quad (15)$$

Therefore, the measurement of double parton interactions in pp and pD collisions could provide an estimation of longitudinal and transverse correlations; moreover for channels where the interference term is largely suppressed (e. g. W +jets), the longitudinal correlation could be directly studied (eq. 11).

References

1. M. Strikman and D. Treleani, Phys. Rev. Lett. **88**, 031801 (2002), [hep-ph/0111468].
2. E. L. Berger, C. B. Jackson and G. Shaughnessy, Phys. Rev. D **81**, 014014 (2010), [arXiv:0911.5348 [hep-ph]].
3. M. Strikman, Acta Phys. Polon. B **42**, 2607 (2011), [arXiv:1112.3834 [hep-ph]].
4. F. Abe *et al.* [CDF Collaboration], Phys. Rev. D **56**, 3811 (1997).
5. M. Diehl, Phys. Rept. **388**, 41 (2003), [hep-ph/0307382].